Pontifícia Universidade Católica
do Rio de Janeiro

Rodrigo Vieira Landim

Tolerance to short crack modeling applied to the structural analysis of Hydrogen Embrittlement under H_2S brine systems and high-pressure gaseous hydrogen.

Tese de Doutorado

Thesis presented to the Programa de Pós-graduação em Engenharia Mecânica from PUC-Rio, in partial fulfillment of the requirements for the degree of Doutor em Engenharia Mecânica.

Advisor: Prof. Marco Antônio Meggiolaro
Co-advisor: Prof. Jaime Tupiassú Pinho de Castro

Rio de Janeiro
May 2024

Pontifícia Universidade Católica
do Rio de Janeiro

Rodrigo Vieira Landim

Tolerance to Short crack modeling applied to the structural analysis of Hydrogen Embrittlement under H_2S brine systems and high-pressure gaseous hydrogen.

Thesis presented to the Programa de Pós-graduação em Engenharia Mecânica from PUC-Rio, in partial fulfillment of the requirements for obtaining the degree of Doutor em Engenharia Mecânica. Approved by the Examination Committee:

Prof. Marco Antônio Meggiolaro
Advisor
Departamento de Engenharia Mecânica – PUC-Rio

Prof. Jaime Tupiassú Pinho de Castro
Co-advisor
Departamento de Engenharia Mecânica – PUC-Rio

Prof. Florian Alain Yannick Pradelle
Departamento de Engenharia Mecânica – PUC-Rio

Prof. Renato Bichara Vieira
Departamento de Engenharia Mecânica – PUC-Rio

Prof. Sérgio Souto Maior Tavares
UFF

Prof. Pedro Soucasaux Pires Garcia
UERJ

Rio de Janeiro, May 6th, 2024

Rodrigo Vieira Landim

Graduated in Mechanical Engineering at CEFET-RJ in 2009 and obtained his M.Sc. Degree in Mechanical Engineering from PUC-Rio in 2012.

Bibliographic data

Landim, Rodrigo Vieira

Tolerance to Short crack modeling applied to the structural analysis of hydrogen embrittlement under H_2S brine systems and high-pressure gaseous hydrogen / Rodrigo Vieira Landim ; advisor: Marco Antônio Meggiolaro ; co-advisor: Jaime Tupiassú Pinho de Castro. – 2024.

128 f. : il. color. ; 30 cm

Tese (doutorado)–Pontifícia Universidade Católica do Rio de Janeiro, Departamento de Engenharia Mecânica, 2024.

Inclui bibliografia

1. Engenharia Mecânica – Teses. 2. Trincas curtas. 3. Trincamento assistido pelo ambiente. 4. Fragilização pelo hidrogênio. 5. Hidrogênio gasoso em alta pressão. 6. Corrosão sob tensão induzida por sulfeto. I. Meggiolaro, Marco Antônio. II. Castro, Jaime Tupiassú Pinho de. III. Pontifícia Universidade Católica do Rio de Janeiro. Departamento de Engenharia Mecânica. IV. Título.

CDD: 621

To my parents, for their support
and encouragement.

Acknowledgements

"This study was financed in part by the Coordenação de Aperfeiçoaento de Pessoal de Nível Superior - Brasil (CAPES) - Finance Code 001”.

Throughout my academic and professional progression, numerous challenges have arisen, which often seem overwhelming when faced alone. I've had the chance to share my life with many individuals who have supported me, provided assistance, and offered opportunities that I have embraced to reach where I am today.

With immense pride in my journey, I extend my heartfelt gratitude to my parents who gave me the chance to study and provided a peaceful, loving, and tranquil childhood home. I owe much to my sister, who has always been there for me, inspiring me to constantly strive for more and never settle. To Thaís, who came into my life with kindness, love, and joy at a time when I was uncertain about continuing my path, she has brought about a significant change in my life. With her by my side, I've completed this phase of life and have embarked on exploring other opportunities I might have missed without her. Each step she has taken makes me proud, with so many victories that we haven't even had time to celebrate all, and she has fueled my desire to give her even more reasons to be proud of me.

I am especially thankful to two professors who often believed in me more than I believed in myself. Professor Jaime Tupiassú sparked my interest in Fracture Mechanics with his light and enjoyable teaching style. And Professor Sérgio, who showed me that even when things didn't go as planned, we could learn valuable lessons and find positives, such as in the failure analysis and case study presented in this work.

There are so many people to thank, including the team at the LAH2S Laboratory at INT who were instrumental in helping me with test execution and daily work with joy and professionalism. I am grateful to Sonia Coelho who, in the early stages of my engineering career, provided me with numerous opportunities for professional growth that have guided me to where I am today.

Abstract

Landim, Rodrigo Vieira; Meggiolaro, Marco Antônio (Advisor). **Tolerance to short crack modeling applied to the structural analysis of Hydrogen Embrittlement under H_2S brine systems and high-pressure gaseous hydrogen.** Rio de Janeiro, 2024. 128p. Tese de Doutorado – Departamento de Engenharia Mecânica, Pontifícia Universidade Católica do Rio de Janeiro.

The development of new technologies with hydrogen as an energy source underscores a longstanding challenge in its transportation and storage, since all structural materials are susceptible to hydrogen embrittlement. The usual approach to solve this problem is to use nobler materials more resistant to hydrogen embrittlement. An alternative approach to mechanical design under hydrogen embrittlement conditions involves the modeling of the behavior of short cracks through linear elastic or elastoplastic fracture mechanics. These models consider two key material parameters: the Environmental Assisted Cracking Resistance Limit and the Crack Propagation Threshold in the environment. In this study, the proposed model is validated by suitable tests under sulfide stress corrosion cracking (High Strength and Low Alloy steel and a supermartensitic stainless steel UNS S41426 exposed to hydrogen sulfide), and in a 17-4PH steel exposed to high-pressure gaseous hydrogen, at 200 bar(g) of H_2. A T-WOL test methodology recommended in ASME BPVC code for measuring the fracture toughness at high pressure of H_2 for materials with high toughness is evaluated, and it yields unsatisfactory results. As an alternative, a modified ASTM E1820 test method is proposed to obtain the J-R curve under high-pressure H_2, obtaining the crack propagation threshold at elastoplastic conditions. During these activities, a load cell used within the test autoclave failed when exposed to 200 bar(g) of H_2. Failure analysis and a new design were conducted according the short crack tolerance model, to allow the use of similar load cells in the following tests.

Keywords

Short cracks; Environmentally Assisted Cracking; Hydrogen Embrittlement; High Pressure Gaseous Hydrogen; Sulfide Stress Cracking.

Resumo

Landim, Rodrigo Vieira; Meggiolaro, Marco Antônio (Advisor). **Modelo de tolerância às trincas curtas aplicado a análise estrutural de Fragilização pelo Hidrogênio em sistemas de salmoura contendo H2S e Hidrogênio gasoso em alta pressão.** Rio de Janeiro, 2024. 128p. Tese de Doutorado – Departamento de Engenharia Mecânica, Pontifícia Universidade Católica do Rio de Janeiro.

O desenvolvimento de novas tecnologias com Hidrogênio como fonte de energia ressalta um antigo desafio nos meios de transporte e armazenamento desse, visto que todos materiais estruturais têm susceptibilidade a fragilização pelo hidrogênio. A forma usual de resolver esse problema é o uso de materiais nobres e mais resistentes a fragilização pelo hidrogênio. Uma alternativa para o dimensionamento mecânico em condições de fragilização pelo hidrogênio vem da modelagem de trincas curtas através da mecânica da fratura linear elástica ou Elasto-Plástica. Esses modelos consideram dois parâmetros do material, o Limite de Resistência ao Trincamento Assistido pelo Ambiente e o Limiar de Propagação de Trincas no meio. Nesse trabalho o modelo proposto é validado experimentalmente em condições de Corrosão sob Tensão Induzida por Sulfetos (aço de alta resistência e baixa liga e o aço inoxidável super martensítico UNS S41426 expostos ao sulfeto de hidrogênio), bem como o aço 17-4PH em 200bar(g) de H_2. O método de teste T-WOL recomendado no código ASME BPVC para a obtenção da tenacidade à fratura sob alta pressão de H_2 é avaliada para materiais com alta tenacidade, a qual não apresentou bons resultados. Como alternativa, uma metodologia modificada a partir da norma ASTM E1820 para obter a curva J-R em H_2 a alta pressão é testada, obtendo o limiar de propagação de trincas em condições Elasto-Plásticas. Durante as atividades, uma célula de carga utilizada no interior da autoclave de teste falhou quando exposta a 200bar(g) de H2. Foi realizada análise de falha e redimensionamento, conforme o modelo de trincas curtas proposto, para que células semelhantes pudessem ser utilizadas nos testes subsequentes.

Palavras-chave

Trincas curtas; Trincamento Assistido pelo Ambiente; Fragilização pelo Hidrogênio; Hidrogênio gasoso em alta pressão; Corrosão sob Tensão Induzida por Sulfeto.

Table of contents

List of Figures

List of Tables

List of Symbols

γ_p	Plastic work per unit of crack area
γ_s	Surface energy
ε	Strain
η	Free surface factor
$\Delta HD(H-H)$	Dissociation Enthalpy
ρ	Density,
σ	Stress
σ_{max}	Maximum stress
σ_n	Nominal stress
τ	Shear stress
Π	Potential energy
Π_0	Internal strain energy
a	Crack size
a_0	Short crack characteristic size
A	Crack surface area
AIDE	Adsorption-induced dislocation emission
AISI	American Iron and Steel Institute
API	American Petroleum Institute
ASME	American Society of Mechanical Engineers
ASTM	American Society for Testing and Materials
BPVC	Boiler and Pressure Vessel
C	Carbon
CH_3COOH	Acetic Acid
CH_3COONa	Sodium Acetate
CO	Carbon Monoxide
CO_2	Carbon Dioxide
CP	Cathodic Protection

Cr	Chromium
CRA	Corrosion-Resistant Alloys
CS_2	Carbon Disulfide
C(T)	Compact Tensile
CTOD	Crack Tip Opening Displacement
DBT	Dibenzyltoluene
DC	Direct Current
DCB	Double Cantilever Beam
DCPD	Direct Current Potential Drop
DC(T)	Disc Compact Tensile
E	Total Energy
E	Elastic Modulus
EAC	Environmentally Assisted Cracking
EAC	Environmentally Assisted Cracking
FAD	Failure Assessment Diagram
Fe	Iron
FEM	Finite Element Method
FeS	Iron Sulfide
FFS	Fitness for Service
$\mathcal{G}$	Energy relief rate
G_C	Fracture toughness
Ga	Gallium
Gr	Grade
H^0	Atomic Hydrogen
H^+	Hydrogen ion
H_2	Hydrogen
H_2O	Water
H_2S	Hydrogen Sulfide
HB	Hardness Brinell
HE	Hydrogen Embrittlement

HEDE	Hydrogen-enhanced decohesion
HELP	Hydrogen-enhanced localized plasticity
HESIPT	Hydrogen-enhanced strain induced phase transformation
HESIVF	Hydrogen-enhanced strain induced vacancy formation
Hg	Mercury
HIC	Hydrogen Induced Cracking
HICC	Hydrogen-induced cold cracking
HP	High-Pressure
HRC	Hardness Rockwell C
HS^-	Bisulfide ion
HSLA	High Strength Low Alloy
HV	Hardness Vickers
J	Joule
J	Potential energy release rate (same as G)
J-R	Resistance Curve
K	Kelvin
K_C	Critical Stress Intensity Factor
kg	Kilogram
K_I	Stress Intensity Factor in mode I
K_{II}	Stress Intensity Factor in mode II
K_{III}	Stress Intensity Factor in mode III
K_{IEAC}	Linear Elastic Cracking Propagation threshold in Mode I for EAC
K_{IH}	Linear Elastic Cracking Propagation threshold in Mode I in Hydrogen medium
K_{JEAC}	Fracture Toughness threshold
K_{gr}	Stress gradient effect
K_t	Stress Concentration Factor
K_{th}	Linear Elastic Cracking Propagation threshold
kPa	kilo Pascal
L	Liter

LHV	Lower Heating Value
LMIE	Liquid Metal Induced Embrittlement
LOHC	Liquid Organic Hydrogen Carriers
m	meter
MCH	Methylcyclohexane
Mn	Manganese
Mo	Molybdenum
MOFs	Metal-organic frameworks
MPa	Mega Pascal
N_2	Nitrogen
Nb	Niobium
Ni	Nickel
P	Phosphorus
P	Load
Pa	Pascal
Pb	Lead
P_c	Condensing Pressure
PDBT	Perthydrodibenzytoluene
PH	Precipitation Hardening
PTFE	Polytetrafluoroethylene
pz	Plastic zone
R-curve	Resistance curve
s	second
S	Sulfur
S^{2-}	Sulfide ion
Sb	Antimony
SCC	Stress Corrosion Cracking
S_{EAC}	Material Strength Limit Against Crack Initiation in EAC conditions
SIF	Stress Intensity Factor
SMIE	Solid Metal Induced Embrittlement

SMYS	Specified Minimum Yield Strength
Sn	Tin
SNG	Synthetic Natural Gas
SO_2	Sulfur Dioxide
SO-HIC	Stress-Oriented Hydrogen Induced Cracking
SSC	Sulfide Stress Cracking
S_y	Yield Strength
T_c	Condensing temperature
TDS	Thermal Desorption Spectroscopy
TEM	Transmission Eletronic Microscope
Ti	Titanium
U1	Strain energy stored in the body
U2	Potential energy relief
UTS	ultimate tensile strength
V	Vanadium
V_{pl}	Plateau Velocity
w	Residual ligament
w_f	Fracture Energy
W_s	Work required to form the two crack surfaces
YS	Yield Strength

1. Introduction

The interaction between hydrogen and metals has challenged researchers and engineers for many decades, due to its implications for material integrity and mechanical design across many industries, such as Nuclear, Aviation, Automotive, Construction, Oil and Gas, and renewable energies (ROBERTSON et al., 2015). Hydrogen's ability to weaken metallic bonds and induce embrittlement poses significant challenges, particularly in high-strength material applications. When hydrogen atoms from various sources adsorbs into the metal surface, they can lead to significant damage, such as micro-cracks through a phenomenon known as Hydrogen Embrittlement (HE) (LYNCH, 2011). In sectors such as Oil and Gas production, the presence of hydrogen sulfide, among other hydrogen sources, accelerates Hydrogen adsorption into the metal through electrochemical corrosion processes (KANE; CAYARD, 1998). Furthermore, with the rising interest in using gaseous and liquid hydrogen as renewable energy carriers, understanding hydrogen interactions with structural materials has become increasingly important.

In mechanical design, engineers are often tasked with optimizing structural geometries to fulfill specific purposes. However, the introduction of notches, while usually unavoidable, leads to local stress concentrations that, in the presence of hydrogen, can cause premature component failures (JONES, 2017). Numerous components in service have been found to host non-propagating cracks in areas with significant stress gradients, a phenomenon that can arise even in the absence of notches.

Conventional engineering approaches to avoid environmentally assisted cracking (EAC) typically involve selecting materials that withstand hydrogen-rich environments based on pass/fail criteria in conditions exceeding those encountered during operation (ASME B31.12, 2019; ASME BOILER AND PRESSURE VESSEL CODE, 2021; NACE MR0175 / ISO 15156, 2020; NACE TM0177, 2016). Despite these precautions, the presence of notches still poses a risk by locally increasing tensile stresses, potentially leading to crack initiation and propagation.

Within the context of Fitness for Service (FFS) assessments, standards like API 579 (2018) offer methodological approaches for evaluating the residual life of damaged components, including those with cracks. However, there is a gap in these

standards, since they do not consider the particular behavior of short cracks, which presents unique challenges due to their apparently odd mechanics and impact on structural integrity in hydrogen environments.

To bridge this knowledge gap by delving into the short crack behavior, a recent model has focused on addressing the influence of short cracks in the design of mechanical components exposed to cyclic loading (CASTRO et al., 2012; CASTRO; MEGGIOLARO, 2016a, 2016b; MEGGIOLARO; MIRANDA; CASTRO, 2007; WU et al., 2010). This model has emerged as a robust tool for accurately estimating fatigue life in such scenarios. After that, another model has been published with the goal of addressing the impact of stress gradient analysis over short cracks in the context of environmentally assisted cracking (EAC) (CASTRO et al., 2015; CASTRO; LANDIM; MEGGIOLARO, 2015; CASTRO; MEGGIOLARO, 2014; LANDIM et al., 2023; SOUSA et al., 2013).

However, this method still has its applicability limited to situations where the material remains in an elastic state even for complex geometries. This condition is not applicable to the majority of real-world scenarios. Recently, the plastic stress concentration effects have been investigated and extended to evaluate the material fatigue strength (LIU et al., 2023).

1.1. Objective

This works aims to evaluate through proper tests the suitability of the model proposed for analysis of structural components used in conditions that might lead to hydrogen embrittlement such as the transport or storage of high-pressure gaseous hydrogen and in brine solution with sulfide hydrogen. It is also an objective to extend the applicability of the EAC model previously presented in (CASTRO et al., 2015; CASTRO; LANDIM; MEGGIOLARO, 2015; CASTRO; MEGGIOLARO, 2014; LANDIM et al., 2023) to an elastoplastic state considering the analysis presented in (LIU et al., 2023). This work also proposes a methodology to obtain elastoplastic parameters in high-pressure (HP) pure gaseous hydrogen.

1.2. Research Outline: Mechanisms, Testing Methods, and Modeling in Hydrogen Environments

The use of hydrogen as an energy source brings several challenges to the industry, some of them due to hydrogen embrittlement mechanism that affects many

of the main materials used to transport or storage traditional fuels. Hydrogen brings as a potential element to replace natural gas or to be mixed to it, which aim to reduce dependence of fossil fuel sources (BLOOMBERG NEF, 2020; EUROPEAN HYDROGEN BACKBONE, 2023). There are several ways to transport and store hydrogen. Each one has their advantages and disadvantages. Chapter 2 will explore how this technology has been developed and how the industry has worked on the way to reach a carbon-free economy, and the importance of hydrogen storage on that.

A large part of the actual net of natural gas distribution are from carbon steel pipelines (ASME B31.12, 2019). They can be susceptible to hydrogen embrittlement, hydrogen induced cracking, blistering, and to those mechanisms associated with fatigue (ASME B31.12, 2019). To find a proper way to test those materials in operational conditions is a necessary step to improve the reliability of preexisting facilities to transport pure gaseous hydrogen or its mixes with natural gas. Moreover, hydrogen has potential to become an alternative solution to work some green energy sources such as solar energy, which is not available at night, and wind power, which is dependent on wind intensity (PATONIA; POUDINEH, 2023). These green energy sources can be used to produce Hydrogen and then storage it for a further application.

Chapter 2 introduces the major mechanisms that affect crack propagation in metals within hydrogen-rich environments, in particular within the two primary hydrogen sources examined in this research: electrochemical hydrogen with H_2S and pure gaseous hydrogen.

For pipeline systems (ASME B31.12, 2019) and storage vessels (ASME BOILER AND PRESSURE VESSEL CODE, 2021), ASME has proposed design methods and ways to evaluate materials properties for use in gaseous hydrogen environments. However, test methods for measuring elastoplastic fracture mechanics parameters are not well-developed for high pressure gaseous hydrogen yet. Therefore, while chapter 3 introduces the fundamentals of fracture mechanics, a new methodology for evaluating notch sensitivity effects in materials susceptible to hydrogen embrittlement is proposed in chapter 3.4.

The use of a short crack tolerance approach to design complex geometries with stress concentration spots is a potentially powerful toll for fitness for service analyses. This approach has been studied and verified for linear elastic conditions

on environmentally assisted cracking (EAC) as presented on chapter 4, for three different EAC mechanisms: Aluminum in liquid Gallium, High Strength Low Alloy steels in H_2S environments, and a Martensitic stainless steel also in H_2S brine solution. All with results that support its efficiency under elastic conditions. An improvement in this model is also proposed.

In chapter 5, this model is extended to account for localized yielding around the notch tip. This chapter also introduces a methodology for determining fracture toughness within high-pressure gaseous hydrogen environments. It analyzes some results from fracture toughness tests conducted according to ASTM E1820 (2023). Furthermore, the chapter proposes a simplified approach for evaluating the full resistance curve (J-R) in a high-pressure gaseous hydrogen environment.

The proposed Elastoplastic model requires just two material properties that must be obtained by proper tests. For hydrogen embrittlement those properties are the material strength limit against crack initiation (S_{EAC}) and the fracture toughness threshold (K_{JEAC}), measured according to ASTM Standards (ASTM E1681, 2023; ASTM E1820-23B, 2023).

Tough materials applied for sour service in the oil and gas industry have good resistance to some hydrogen embrittlement mechanisms (NACE MR0175 / ISO 15156, 2020). However, the damage mechanism those materials have been tested for are due to electrochemical corrosion, such as sulfide stress corrosion cracking, or else due to cathodic polarization. Since those materials can be a low-cost alternative to transport or store gaseous hydrogen at high pressure, Section 5.1.2 describes the tests of an API 5L X65 steel within gaseous hydrogen at 200 bar(g).

During the implementation of ASTM E1820-23B (2023) test procedures applied to high-pressure gaseous hydrogen, the internal load cell of the hydrogen pressure vessel failed on its screw by hydrogen embrittlement. This failure was not expected and the initial failure analysis indicates an error in material selection. The load cell received was made from 17-4PH stainless steel, but to keep the tests with an internal load cell it was decided to apply the same model proposed to qualify and validate the use of this load cell for a new maximum load.

Chapter 6 studies the failure analysis of the 17-4PH load cell during the resistance curve tests under high-pressure gaseous hydrogen. The material has high values of S_{EAC} and extremely low K_{IEAC}. The condition for the load cell has been a

study case to verify the efficiency of the proposed model, generating useful data to prevent similar failures.

1.3. Alternative technologies for Hydrogen storage and transport

Most renewable energy sources are inherently intermittent. Solar energy is available only during the day, hydropower relies on river flow or reservoir level, which depends on rainfall, and wind energy is contingent on wind availability (PATONIA; POUDINEH, 2023). Thus, energy storage is crucial for optimizing the use of intermittent renewable energy sources and balancing energy supply and demand.

Various storage methods offer different capabilities, with electrochemical and electrical solutions suitable for mid-range storage and mechanical solutions, dependent on geographical factors, having the potential for larger-scale storage (PATONIA; POUDINEH, 2023). Chemical energy storage, particularly hydrogen, holds the greatest potential for large-scale energy storage. This can be achieved through the storage of compressed hydrogen gas in large tanks, underground storage, liquid hydrogen, or hydrogen carriers like ammonia and liquid organic hydrogen carriers (MØLLER et al., 2017). Hydrogen can even be stored in the solid state by combining it with light elements, such as magnesium, to form hydrides that can achieve very high gravimetric hydrogen densities (>100kg H_2/l) (MØLLER et al., 2017).

While considerable attention has been directed towards hydrogen production and transportation, storage remains a crucial yet underexplored component in its use. Effective hydrogen storage is imperative for its role as a traded commodity, as it typically needs to be stored after production and prior to delivery to end-users. Historically, hydrogen has been primarily consumed near to its generation point, with its storage and transportation occupying a secondary position in the hydrogen chain (INTERNATIONAL ENERGY AGENCY, 2021; PATONIA; POUDINEH, 2023). Nevertheless, as we advance towards a hydrogen-based economy, the focus must shift to understand and to address the challenges and peculiarities associated with preserving hydrogen in various quantities for different durations.

Hydrogen presents unique storage challenges due to its status as the smallest and lightest molecule in the universe and to its gaseous nature under standard conditions (MØLLER et al., 2017; PATONIA; POUDINEH, 2023). Enhancing

hydrogen storage is essential for practicality and economics, necessitating improved density to rival or surpass commonly used fossil fuels. At normal temperature and pressure, hydrogen has extremely low volumetric density, approximately 0.0812 kg/m³ (MØLLER et al., 2017), but this increases when it is compressed or liquefied. Despite these enhancements, hydrogen falls short as an energy carrier when compared to conventional fossil fuels (Table 1) (STĘPIEŃ, 2021). To address this, converting hydrogen into other substances with higher volumetric density may be necessary. However, the optimal storage choice depends on various factors, including hydrogen density, volume, duration, safety, and intended usage (PATONIA; POUDINEH, 2023).

Table 1.Hydrogen properties compared with common hydrocarbon fuels, adapted from (STĘPIEŃ, 2021).

Property	**Hydrogen**	**Methane**	**Gasoline**
Carbon content (mass%)	0	75	84
Lower (net) heating value (MJ / kg)	119.9	45.8	43.9
Density (at 1 bar & 273 K; kg/m3)	0.089	0.72	730-780
Volumetric energy content (at 1 bar & 273 K; MJ /m3)	10.7	33	33×10^3
Molecular weight	2.016	16.043	≈110
Boiling point (K)	20	111	298-488
Auto-ignition temperature (K)	853	813	≈623
Minimum ignition energy in air (at 1 bar & at stoichiometry; mJ)	0.02	0.29	0.24
Stoichiometry air/ fuel mass ratio	34.4	17.2	14.7
Quenching distance (at 1 bar & 298 K at stoichiometry; mm)	0.64	2.1	≈2
Laminar flame speed in air (at 1 bar & 298 K at stoichiometry; m/s)	1.85	0.38	0.37-0.43
Diffusion coefficient in air (at 1 bar & 273 K; m2 /s)	8.5×10^{-6}	1.9×10^{-6}	-
Flammability limits in air (vol%)	4 - 76	5.3 - 15	1 - 7.6
Adiabatic flame temperature (at 1 bar & 298 K at stoichiometry; K)	2480	2214	2580

As observed in Table 1, when compared to hydrocarbon fuels, hydrogen presents advantages in terms of carbon content, Lower Heating Value (LHV), Stoichiometry air/fuel mass ratio, minimum ignition energy, and other factors (STĘPIEŃ, 2021). However, its lower density and molecular weight make its Volumetric energy content less attractive when compared to Methane or gasoline.

To make hydrogen storage more practical and cost-effective, its density must be improved to match or exceed that of conventional fossil fuels. Compression and liquefaction are two methods to achieve this, with compression requiring high-pressure tanks (Table 2).

Hydrogen can be stored as a gas, liquid, or in porous solids, and there are six primary storage types: pure hydrogen, synthetic hydrocarbons, chemical hydrides, liquid organic hydrogen carriers (LOHC), metal hydrides, and porous materials (Table 2). When hydrogen is compressed and stored, the lowest cost is achieved when it is stored in pressurized containers with small volumes on a daily basis, or in large volumes on a monthly or weekly basis in salt caverns (BLOOMBERG NEF, 2020).

Pure hydrogen can be stored through compression or liquefaction, with compression using high-pressure tanks (350-700 bar). It allows for direct use but consumes energy during compression. Compressed hydrogen is favored for fuel cell vehicles and large-scale storage, although it has energy intensity and safety issues.

While gaseous hydrogen itself is non-toxic, the majority of hydrogen storage forms can present safety concerns due to their potential for being corrosive, toxic, and flammable (Table 2). Therefore, it is crucial to prioritize safety when dealing with these various hydrogen storage methods.

Recent pilot projects have successfully blended up to 20% hydrogen with hydrocarbon fuels. Notable among these is the HyDeploy initiative in the Northeast of England, where a blend of hydrogen is being supplied to 100 homes and 30 campus buildings, resulting in the abatement of 27 tonnes of carbon (HYDEPLOY, 2024). Similar initiatives are gaining momentum globally, including the EHB (EUROPEAN HYDROGEN BACKBONE, 2023), HyBRIDS in Italy, HIGGS in the EU, HyBlend in the USA, and HyP projects in Australia.

Compressing hydrogen to 700 bar results in a significantly lower volumetric energy density (5.6 MJ/l) compared to gasoline (32.0 MJ/l) (PATONIA; POUDINEH, 2023). This issue can be partially addressed by utilizing high-pressure cylinders/tanks and solid-state materials with hydrogen (MØLLER et al., 2017). However, storing highly compressed hydrogen in larger vessels, such as tanks or spheres designed for marine transport, involves safety issues related to hydrogen embrittlement, as some materials are vulnerable to this effect.

Table 2.Hydrogen storage forms characteristics, adapted from (PATONIA; POUDINEH, 2023).

State	Storage forms		Volumetric Hydrogen density	Gravimetric H2 content	Corrosiveness	Toxicity	Flammability	Cost of storage (US$/kg)	Energy use for storage in (kJ/mol per day)
Gas	Compressed Hydrogen		Medium	High	Yes	No	Yes	0.23	< 10
	Synthetic Hydrocarbons	Synthetic Methane/ SNG	Low	Medium	No	No	Yes	- 1.90	> 1.9
		Liquified SNG	High	Medium	No	No	Yes	-	19.1 – 34.7
		Synthetic gasoline	High	Medium	No	Yes	Yes	-	N/A
		Synthetic diesel	High	Medium	No	Yes	Yes	-	
	Liquid Hydrogen		Medium	High	Yes	No	Yes	4.57	> 28.3
Liquid	Chemical Hydrides	Liquid Ammonia	High	Medium	Yes	Yes	Yes	2.83	≈1
		Methanol	High	Medium	Yes	Yes	Yes	-	N/A
		Formic Acid	Medium	Low	Yes	Yes	Yes	-	
		Isopropanol	Low	Low	Yes	Yes	Yes	-	
	Liquid Organic Hydrogen Carriers	Toluene / Methylcyclohexane (MCH)	Low-Medium	Low	No	Yes	Yes	4.50	
		Naphtalene/ decalin	Medium	Low	No	Yes	Yes		
		Benzene/ cyclohexane	Medium	Low	No	Yes	Yes		
		Dibenzyltoluene (DBT)/ perthydro-dibenzytoluene (PDBT)	Medium	Low	No	Yes	Yes		
Solid	Metal Hydrides	Elemental metal hydrides	High	Low-Medium	No	No	No	-	N/A – 0.6
		Inter-metallic Hydrides	High	Low	No	No	No	-	
		Complex - metal hydrides	Medium-High	Low-Medium	No	No	No	-	
	Porous materials	Carbon fibers	Low	Low-Medium	No	No	No	-	4.4 – 12
		Carbon nanotubes	Low	Low-Medium	No	No	No	-	
		Activated carbon	Low	Low	No	No	No	-	
		Graphene	Low	Low	No	No	No	-	
		Carbon aerogel	Low	Low	No	No	No	-	
		Templated carbon	Low	Low	No	No	No	-	
		Metal-organic frameworks (MOFs)	Low	Low-Medium	No	No	No	-	

1.4. ASME code design for pipeline and storage tanks

ASME B31.12 (2019) provides guidelines for the use of structural steels in the transportation of hydrogen. It is important to note that, according to the ASME, all structural steels are susceptible to hydrogen embrittlement (HE), with the severity of this susceptibility varying depending on factors such as temperature and the partial pressure of hydrogen. On the other hand, ASME BPVC Section VIII Division III (2021) presents on article KD-10 special requirements for the design of high-pressure vessels containing hydrogen. Furthermore, the ASME BPVC code mandates K_{IH} tests in accordance with ASTM E1681(2023) to assess material properties, but does not account for the elastoplastic state in crack evaluation.

Preliminary tests using ASTM A516 Gr. B carbon steel at 200 bar H_2 pressure demonstrated that the ASTM E1681 (2023) test method may not be suitable for evaluating K_{IH} for all carbon steels, especially when dealing with specimens known to be susceptible to hydrogen embrittlement. Details are presented on Chapter 5.1.1

Among the guidelines outlined in ASME B31.12 for pipelines, the standards emphasize the importance of limiting hydrogen gas pressure and pipeline dimensions to prevent hydrogen embrittlement. The code ASME B31.12 also indicates some materials to operate in dry hydrogen environments (less than 3ppm of H_2O) and says to avoid others, as indicated in Table 3. Where, these compatible materials have less susceptibility to HE than the not compatible ones.

As mentioned earlier, all structural materials are susceptible to hydrogen embrittlement, and as the hardness and the strength of the materials increase, the susceptibility to HE also increases. It is essential to remember that when use the data presented in Table 3.

Additionally, certain alloys that are classified as 'Not compatible' have shown promising performance within a specific range of hydrogen exposure. For instance, low-strength nickel alloys with low iron content, like Hastelloy C276 and C22, are employed to manufacture the autoclaves used in this study.

Table 3. Material compatibility with gaseous hydrogen according to ASME B31.12 (2019).

Materials compatible with gaseous hydrogen	Materials NOT compatible with gaseous hydrogen
Aluminum and aluminum alloys	Gray, ductile, or cast iron
Austenitic stainless steels with greater than 7% Nickel (e.g., 304, 304L, 308, 316, 321, 347)	Ferritic and Martensitic High alloyed steels (410, 430, 440, 17-4PH, and HP9-4-20)
Low alloy Carbon steels (ASTM A106 Grade B, ASTM A53 Grade B, and API 5L Grades X42 and X52)	Nickel and some nickel alloys (e.g., Inconel and Monel)
Copper and copper alloys (e.g., brass, bronze, and copper–nickel)	Nickel steels (e.g., 2.25%, 3.5%, 5%, and 9% Ni)
Titanium and titanium alloys	-

The following chapter details the hydrogen embrittlement mechanism and its behavior in steels.

2. Hydrogen Embrittlement (HE), an Environmentally Assisted Cracking (EAC) Mechanism.

Hydrogen embrittlement is a failure mechanism caused by the interaction between a susceptible material and hydrogen under applied mechanical loading. Similar to all environmentally assisted cracking (EAC) mechanism, of which HE is one, HE depends of the synergistic effect of three components. The absence of any of these three components, namely a *susceptible material*, a *corrosive environment*, and *applied mechanical loading*, is sufficient to prevent any EAC mechanism. EAC mechanisms are commonly classified into five mechanisms, which include:

- *Stress Corrosion Cracking, SCC*
- *Hydrogen Embrittlement, HE*
- *Liquid Metal Induced Embrittlement, LMIE*
- *Solid Metal Induced Embrittlement, SMIE*
- *Corrosion Fatigue.*

2.1. Environmentally Assisted Cracking in metals

Stress Corrosion Cracking is commonly associated with low crack growth rate mechanisms inside aqueous environments. SCC can follow one of four paths during its nucleation and propagation phases, as illustrated in the flow diagram from Fig 1.

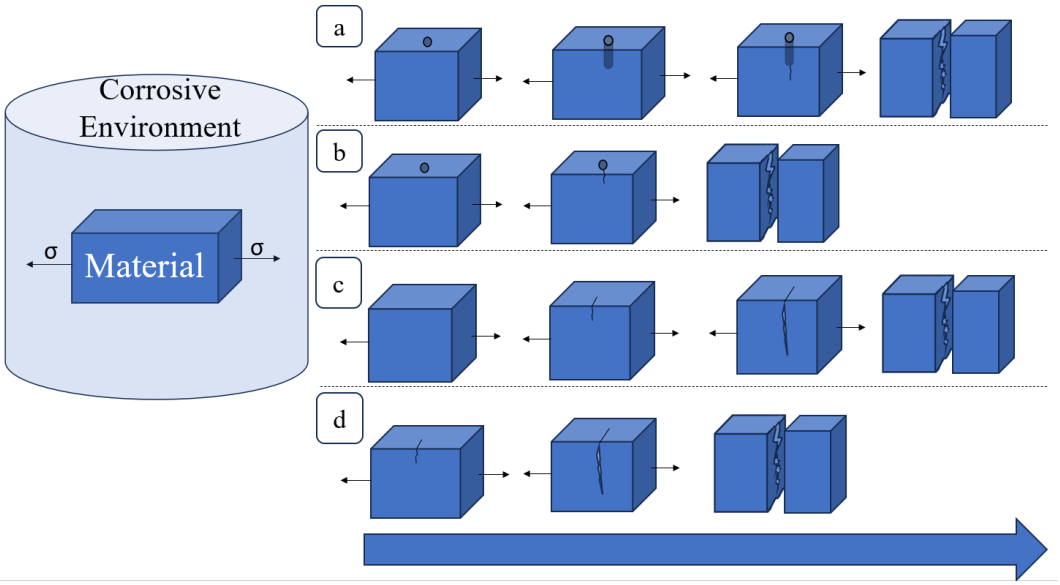

Fig 1. Stress corrosion cracking flow diagrams (Source: Created by the author)

Where, each path in Fig 1 corresponds to:

a) Localized corrosion pit nucleates due to corrosion, grow for a while, and then nucleates a crack that propagates until failure.

b) is Similar to (a), localized corrosion pit nucleates, however it does not continuously grow, and a crack starts and then propagates.

c) A crack starts without any localized corrosion pit beforehand and then begins to propagate.

d) A preexisting flaw has a Stress Intensity Factor (SIF) higher than the SIF threshold, and the crack propagates until failure

Pitting corrosion affects crack initiation in two ways. Firstly, it acts as a notch, increasing local stress at the notch root with an intensity that depends on the pitting depth and root radius. Secondly, it changes the electrochemical conditions since, inside the pit, the localized environment can concentrate chemical ions, creating a more corrosive region on the component surface.

Corrosion Resistant Alloys commonly have their SCC mechanism associated with the nucleation and growth of localized corrosion pits, as shown in Fig 1 (a) and (b). This localized corrosion breaks the passive film, exposing the bulk metal to the corrosive environment, which in turn creates the condition for crack initiation and propagation (JONES, 2017).

When Corrosion-Resistant Alloys (CRA) are immersed in a corrosive fluid at the temperature and electrochemical potential where pitting begins, it results in a non-passivated surface. The bulk material exposed to the solution within the pit experiences localized galvanic corrosion, and the potential can reach a condition where crack initiation occurs (JONES, 2017).

SCC in High Strength Low Alloy (HSLA) steels can start in a manner similar to that in CRAs. It can also occur without the presence of localized corrosion, such as in cases where hydrogen serves as the embrittlement agent (BROWN, 1972). Furthermore, as it will be detailed later in this work, cracks can nucleate and propagate just for a while and then becomes non-propagating due to the stress gradient ahead of the notch tips (CASTRO; LANDIM; MEGGIOLARO, 2015; CASTRO; MEGGIOLARO, 2014).

Stress corrosion cracks can propagate through either an anodic dissolution path or a cathodic mechanism (JONES, 2017), where significant dissolution may

not be evident. Even as the crack propagates, it is influenced by corrosion reactions that brings brittle agents to the crack tip.

The crack propagation behavior of the Environmentally Assisted Cracking mechanisms is illustrated in Fig 2.

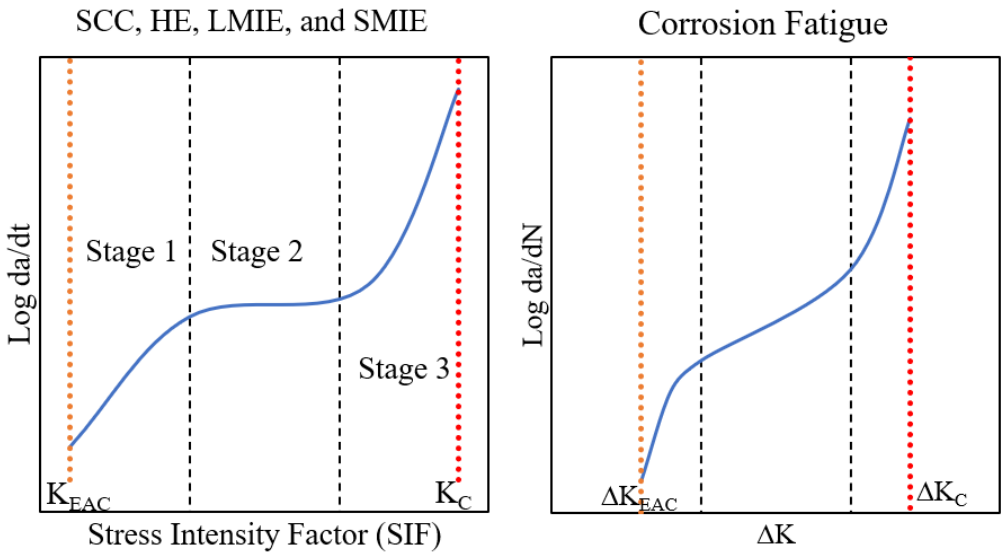

Fig 2. Crack propagation behavior under the EAC mechanisms, on the left SCC, HE, LMIE, and SMIE, and on the right Corrosion Fatigue (Source: Created by the author).

For crack propagation to occur, the Stress Intensity Factor (SIF) needs to become larger than the crack propagation threshold (K_{th}). Immediately after this, subcritical crack propagation begins, which can be divided into three stages:

- *Stage 1: Dependent on both chemical reactions and mechanical forces, it is associated with low growth rates, which change fast with the increasing in the SIF.*
- *Stage 2: Also known as the plateau region, it exhibits an almost constant growth rate and is considered in cases where it is possible to monitor and tolerate the presence of the crack. This region is predominantly influenced by chemical and electrochemical reactions. The SIF has low influence on the crack propagation rate.*
- *Stage 3: The crack propagation rate is high and almost independent of the environment. It ends at the critical Stress Intensity Factor (K_C), where the material undergoes rapid and catastrophic fracture.*

Corrosion fatigue must be presented in a different way, since the propagation occurs due to the synergistic effect of the environment and fatigue. Therefore, cyclic parameters characterized by the Greek letter Δ must be used in its analyses.

Differing from SCC, which is primarily a chemical or electrochemical mechanism, LMIE and SMIE are fundamentally physical mechanisms. Both mechanisms occur in solids with low or no solubility with other metals when in a solid state. SMIE typically occurs at temperatures slightly above the melting point of the metal, leading to crack formation. In contrast, LMIE is associated with the interaction of solids with metals below their melting points (INA; KOIZUMI, 2004).

Sub-critical cracks under LMIE can initiate at Stress Intensity Factors (K_I) as low as 0.1 MPa.m$^{-1/2}$, and the plateau velocity (V_{pl}) can reach speeds as high as 0.1 m/s (GLICKMAN, 2011). For example, aluminum alloys are susceptible to LMIE in the presence of liquid Ga, Pb, or Hg, leading to a significant loss of ductility when subjected to tensile stress (GLICKMAN, 2011; INA; KOIZUMI, 2004; VASUDEVAN, 2013).

Among all EAC mechanisms, hydrogen embrittlement stands out as one of the most versatile. This phenomenon can be associated with various mechanisms, whether chemical, electrochemical, or physical. It may occur as a result of corrosive processes, cathodic protection, quenching, or the hydrostatic pressure of pure gaseous hydrogen (LYNCH, 2012). When associated with an electrochemical corrosive process, it is commonly called a Stress Corrosion Cracking (SCC) mechanism. An example of this electrochemical corrosion mechanism occurs with high strength steels in presence of hydrogen sulfide (H_2S) (KANE; CAYARD, 1998). In acidic conditions, H_2S is chemically stable and can be easily dissolved in aqueous solutions to form corrosive environments. Steel corrosion reaction under anaerobic environments commonly occurs according to the following process (KANE; CAYARD, 1998):

Anode reaction:

$$Fe \rightarrow Fe^{2+}2e^{-} \quad (1)$$

Cathode reaction:

$$H_2S + H_2O \rightarrow H^+ + HS^- + H_2O \quad (2)$$

$$HS^- + H_2O \rightarrow H^+ + S^{2-} + H_2O \quad (3)$$

Global reaction:

$$Fe + H_2S + H_2O \rightarrow FeS + 2H^0 \quad (4)$$

The production of atomic hydrogen (H^0) at metal cathodic sites is one typical byproduct of corrosion. The majority of this H^0 recombines on the metal surface to form a harmless hydrogen gas (H_2) that leave as bubbles without affecting the metal, but the presence of H_2S or other sulfur species as HS^- and S^{-2} dissolved can significantly delay that process and increase the atomic hydrogen absorption by the material. This recombination behavior is similar to what happens with other species such as Sn, Pb, Sb, and P.. This phenomenon significantly delays or hinders the hydrogen recombination kinetics, and it is commonly called hydrogen recombination "poison" (KANE; CAYARD, 1998).

In this corrosion process, atomic hydrogen (H^0) production at local cathodic sites can be seen where it is adsorbed onto the metal surface and forms iron–sulfur compounds with various phases as corrosion products. Different stoichiometric ratios of iron and sulfur produce many solids including cubic iron sulfide, mackinawite, and troilite (all FeS), pyrite (cubic FeS_2), marcasite (FeS_2), greigite (Fe_3S_4), pyrrhotite ($Fe_{1-x}S$ or Fe_7S_8), and smythite (Fe_9S_{11}) (BAI et al., 2014).

The presence of H_2S, and of the sulfur species formed from it, also enhances the hydrogen charging associated with the absorption of H^0 by the metal. The Sulfide Stress Corrosion Cracking mechanism is associated with the hydrogen embrittlement cracking effect associated with H_2S (KANE; CAYARD, 1998).

Low alloy steels also are susceptible to blistering, hydrogen induced cracking (HIC) and stress-oriented hydrogen induced cracking (SO-HIC). In these materials, the absorbed hydrogen recombines to form in a gas phase H_2 enhancing the local stresses inside the metal. These mechanisms do not need an external loading to achieve the cracking, since the internal forces are significantly high (KANE; CAYARD, 1998).

As mentioned earlier, hydrogen is a byproduct of corrosion linked to cathodic reactions. During either cathodic protection (CP) or cathodic polarization, hydrogen is generated at the metal surface. High-strength low-alloy (HSLA) steels and some corrosion-resistant alloys (CRAs) may be susceptible to hydrogen embrittlement when overprotected. The quantity of hydrogen produced is directly proportional to

the applied cathodic current, and the risk of the embrittlement mechanism intensifies as more hydrogen is generated and adsorbed onto the metal surface.

In addition to the electrochemical mechanisms of hydrogen embrittlement, metals can also crack in the absence of an electrolyte due to hydrogen. This phenomenon occurs when subjected to high hydrostatic pressure of H_2 or when the metal is heated in the presence of H_2, and the cooling rate is faster than the rate necessary to allow the hydrogen to exit the microstructure (SHVACHKO, 2000).

Hydrogen-induced cold cracking (HICC) in structural steels welds occurs due to the higher solubility of H_2 in molten metal than in its solid state. During welding, hydrogen diffuses into the metal, and upon cooling, it lacks sufficient time to exit the microstructure. Consequently, the high residual stress in welding, coupled with the hydrogen embrittlement mechanism and susceptible microstructure (martensite with %C $\geq$ 0.10%), can lead to cracks emerging minutes, hours, or days after welding. Pre-heating and certain post-weld heat treatment procedures can prevent this issue, as higher temperatures facilitate faster hydrogen release from the microstructure, preventing entrapment (YURIOKA; SUZUKI, 1990).

Among the various types of hydrogen embrittlement (HE) discussed earlier, embrittlement under high hydrostatic pressure of hydrogen is perhaps the most straightforward to comprehend. Due to hydrogen being the smallest element in the universe, it can readily be adsorbed into the metal surface and diffuse into the metal lattice. The diffusion of hydrogen in the solid state is contingent upon the partial pressure of hydrogen surrounding the embrittled metal (LYNCH, 2012).

Hydrogen embrittlement is commonly recognized as a low-temperature mechanism, typically occurring below 95ºC. All structural materials experience a loss of ductility and/or of toughness due to hydrogen embrittlement. However, certain materials, such as some titanium alloys, high-chromium nickel alloys, and many annealed austenitic stainless steels, are considered 'immune' to hydrogen embrittlement in various environments (ASME B31.12, 2019).

Some nonferrous alloys such as Aluminum alloys are resistant to hydrogen embrittlement in dry hydrogen gas but can be susceptible in the presence of water vapor. Copper alloys with oxygen can also be embrittled in hydrogen gas due to the reaction between dissolved hydrogen and oxygen. Therefore, oxygen-free grades of copper can be used for dry hydrogen gas applications (ASME B31.12, 2019).

2.2. Hydrogen Embrittlement in steels

The susceptibility of steels to hydrogen embrittlement is inherently linked to their strength. As the ultimate tensile strength (UTS) and the yield strength (YS) increase, hydrogen embrittlement becomes more pronounced. At near-ambient temperature, steels with YS above 800 MPa tends to be susceptible to HE. These high-strength steels have their application limited in presence of gaseous hydrogen or electrochemical environments that can liberate high concentrations of hydrogen by corrosion reactions of the metal, like in presence of H_2S. K_{IEAC} below 20 MPa.$m^{-1/2}$ is common for materials with YS higher than 1,250 MPa (MCLNTYRE, 1985). As the material strength looks to be a key factor in the embrittlement behavior of steels in presence of hydrogen, increasing the amount of hydrogen in the steel or the pressure of gaseous hydrogen increase their tendency to suffer HE.

2.2.1. Influence of the environment in the hydrogen embrittlement in steels, gaseous hydrogen and sulfide hydrogen

The embrittlement mechanism due to hydrogen reaches its maximum effect on steels just below ambient temperature, with low effect below −100°C or above 100°C (MCLNTYRE, 1985). The main environmental variables associated to SSC in HSLA steels are temperature, pH, and partial pressure of H_2S. Low pH normally is more severe than high pH, probably because low pH indicates more hydrogen into the solution. Tests at room temperature are more susceptible to SSC than tests at relatively high temperature like 200ºC, since high partial pressures of H_2S increase the susceptibility to SSC (KANE; CAYARD, 1998).

Similar behavior can be observed in tensile tests carried out on high-strength steels under gaseous hydrogen and in H_2S aqueous solutions. Loss of ductility or the extension of cracks originating from the surface enhance with the content of H_2S in the solution or with the pressure of hydrogen. High strength steels have a tolerance limit to both hydrogen and H_2S. NACE MR0175 / ISO 15156 (2020) gives the threshold of 0.3 kPa for the occurrence of Sulfide Stress Cracking (SSC), while Bowker and Hardie (1975) found a threshold just below 1 kPa for a high strength steel 5CrMoV under gaseous Hydrogen.

Strain rate tensile test methods have been widely used to evaluate HE susceptibility of materials, which characteristic is to induce a reduction in the tensile

ductility or the occurrence of cracks originating and propagating from the surface, depending on the applied strain rate. Strain rates as low as $3x10^{-2}$ s^{-1} do not produce any effect in the materials properties. Time is necessary to activate HE (BOWKER; HARDIE, 1975).

NACE TM0198 (2020) recommends strain rates as low as $1x10^{-6}$ (m/m)/sec for stainless steels, but indicates that $4x10^{-6}$ (m/m)/s rates can guarantee satisfactory results. Indeed, the relationship between the strain rate and the loss of ductility is an exponential function, and lower values yield results close to the limits. However, those recommendations are for corrosion-resistant alloys, which have a hydrogen permeation rate significantly lower than carbon steels, which commonly show satisfactory results at rates slightly higher than those recommended for corrosion-resistant alloys (NACE TM0198, 2020).

When comparing the performance of high strength steels in gaseous hydrogen and in H_2S aqueous environments, a similar behavior can be observed also for the hardness influence on the material susceptibility to HE. According to NACE MR0175 / ISO 15156 (2020), Low Strength and Low Alloy steels with Hardness below 22HRC (248 HV) are commonly not susceptible to SSC and can be used for "*sour"* service operations, which means in the presence of H_2S (NACE MR0175 / ISO 15156, 2020). Additionally, NACE MR0175 / ISO 15156 (2020) gives the H_2S partial pressure limit for many alloys, which shall be followed linked to the hardness control to avoid SSC.

As presented in Fig 3, Almond et al. (ALMOND et al., 1983; MCLNTYRE, 1985) tested a gas cylinder material (1CrMoV steel) with hardnesses varying from 260HB to 340HB (275HV to 360HV) through different heat treatments at 6.9 MPa of gaseous hydrogen, and their results also indicated a threshold in hardness.

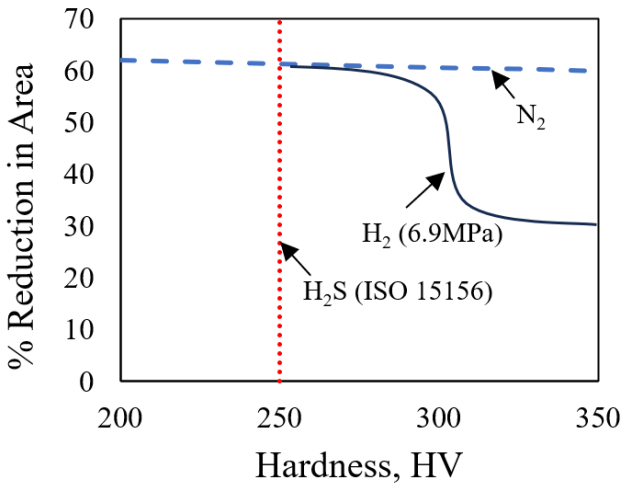

Fig 3. Hardness effect in the area reduction of carbon steels under hydrogen environments. Curves for N_2 and 6.9MPa H_2 obtained for a 1CrMoV steel, adapted from (ALMOND et al., 1983; MCLNTYRE, 1985).

The values from Almond et al. (ALMOND et al., 1983; MCLNTYRE, 1985) have been converted to Vickers hardness based on ASTM E140-12B (2019) to be compared with recommended hardness limits in H_2S environments.

Zhao et al. (2015) performed a study using nano-indentation hardness and Thermal Desorption Spectroscopy (TDS) to identify the influence of the hydrogen charging process in the hardening or softening effect. They found out that when electrochemical hydrogen charging produce hardening in low alloy steels, it is due to their typical higher content of hydrogen and non-uniform distribution. On the other hand, environments with gaseous hydrogen, which have a more uniform hydrogen distribution at lower levels, induce softening in the steel.

As previously mentioned, high yield strength steels tend to be more susceptible to hydrogen embrittlement. Hence, low K_{IEAC} values and high crack propagation rates are expected for these materials. As indicated in Fig 4, Mclntyre and Priest (1985) measured crack propagation rates for a high yield strength steel (above 1,380 MPa) and found lower crack propagation thresholds for H_2S environments at the same pressure as gaseous hydrogen (MCLNTYRE, 1985).

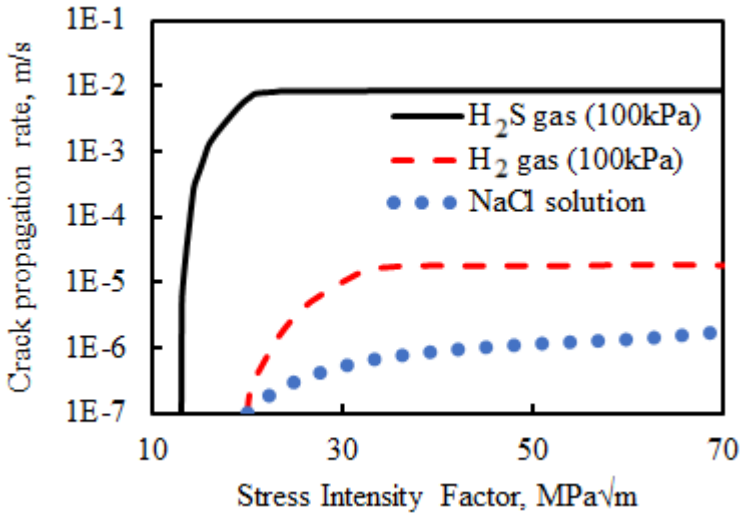

Fig 4. Crack propagation behavior for 4NiCrMo steel in hydrogen environments and in brine solutions. Adapted from (MCLNTYRE, 1985).

Partial pressures of H_2S above 1 kPa indicate low influence in the K_{IEAC} threshold for high strength steels (HSS) with high susceptibility to SSC, see Fig 5. According to ISO 15156-2 (NACE MR0175 / ISO 15156, 2020), the limits to start an SSC is around 0,3 kPa. Therefore, cracks can still propagate in partial pressures below that for high susceptible materials.

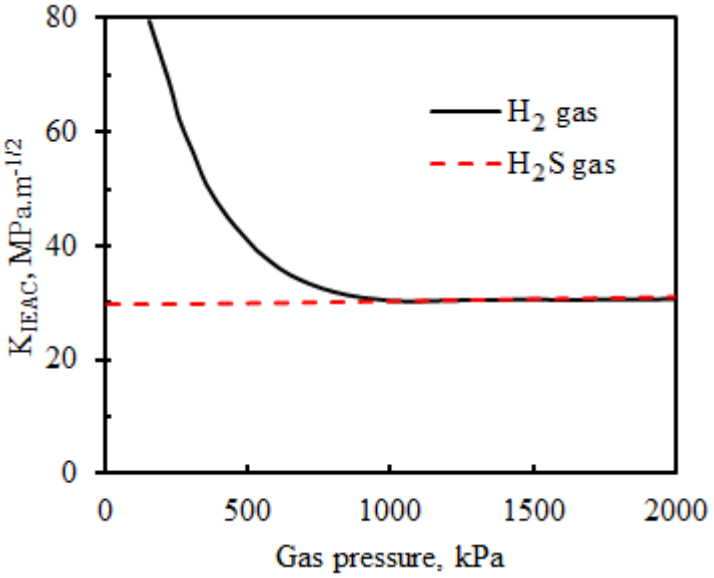

Fig 5. Influence of gas pressure on stress intensity factor threshold (K_{IEAC}) for AISI 4340 steel in hydrogen environments. Adapted from (MCLNTYRE, 1985).

The K_{IEAC} of high strength steels with YS higher than 1,380 MPa is not much affected by the hydrogen environment. Increasing the H_2 gas pressure in the environment or the total pressure of H_2S tend to induce similar K_{IEAC} values, which indicate a limit in the amount of hydrogen adsorbed and absorbed in the steels to

embrittle them (MCLNTYRE, 1985), as seen in Fig 5. Therefore, the crack growth rates in the hydrogen sulfide gas environment are about three to four orders of magnitude faster than those in hydrogen gas.

Small amounts of oxygen tend to arrest cracking in pre-cracked specimens. ASME BPVC VIII-3 (ASME BOILER AND PRESSURE VESSEL CODE, 2021) indicates a limit for impurities that can affect the K_{IEAC} measurements, which are O_2 < 1 ppm, CO_2 < 1 ppm, CO < 1 ppm and H_2O < 3 ppm. As the steel has a preferential surface reaction with O_2 than with H_2, small amounts of O_2 can adsorb in the crack tip and delay the gaseous H_2 interaction with steel arresting the crack. In H_2S environments, the almost instantaneous chemical reaction between H_2S and O_2 in aqueous solutions also reduce the total amount of free sulfide dissolved elements, and consequently their poisoning effects.

0,7% of O_2 in gaseous hydrogen environments are enough to arrest hydrogen assisted cracking at ambient pressure (MCLNTYRE, 1985). Cyclic loading conditions behave in a different way, since a disturbance in loading can break the oxide film and expose the metal cracked surface or remove the oxygen from the crack tip. In gaseous hydrogen environments, CO, CS_2, and SO_2 are hydrogen assisted cracking inhibitors. These catalytic poisons adsorb in steel surface and poison the chemical active sites preventing hydrogen molecules dissociation into atoms (MCLNTYRE, 1985).

2.2.2. Effect of microstructure and alloy elements in HE of steels

The microstructures and chemical compositions of high strength steels (with YS higher than 1,250 MPa) have a low effect in their hydrogen assisted cracking behavior. However, for mild steels this effect increases as their strength level decreases (MCLNTYRE, 1985).

Alloying elements such as Mo, V, Ti, and Nb can reduce the susceptibility to SSC and increase the stress intensity threshold in H_2S aqueous environments, due the formation of fine carbides of these elements. In ferritic steels, impurities as sulfur and phosphorus, and alloying elements such as carbon, manganese, and chromium can increase their susceptibility to hydrogen embrittlement (LI et al., 2020).

The microstructure of high alloy steels plays a significant role in determining their vulnerability to hydrogen embrittlement. Austenitic stainless steels are usually considered resistant to HE. However, the presence of ferrite, martensite, and chemical composition can affect their susceptibility. AISI 304 and AISI 316 can undergo martensitic transformation due to high plastic deformation during cold forming, which turns the material more susceptible to hydrogen assisted cracking.

For applications involving hydrogen gas, a higher nickel content is advisable. Except for certain austenitic stainless steels, most highly alloyed steels are generally susceptible to hydrogen embrittlement. Specific steels like AISI 410, 430, 440, and 17-4PH are not recommended for use with hydrogen gas (ASME B31.12, 2019).

Table 4 summarizes the influence of the main alloy elements and impurities in hydrogen assisted cracking.

Table 4. Influence of chemical elements in hydrogen assisted cracking (ASME B31.12, 2019)

Enhances the resistance against hydrogen embrittlement	Reduces the resistance against hydrogen embrittlement
Ni, Mn(1), Mo, V, Ti, and Nb	S, P, C, Mn(2), and Cr

Note 1: For ferritic steels Mn reduces the resistance against HE.
Note 2: Mn for austenitic steels stabilizes the austenite and enhances resistance to HE.

Among them, manganese is an element that plays dual roles, depending on the microstructure of the steel. In ferritic steels, low levels of manganese can decrease the resistance to hydrogen embrittlement. On the other hand, when added in higher amounts to stabilize austenite, manganese can enhance the steel's resistance to HE.

2.3. Main Hydrogen Embrittlement mechanisms proposed models for steels.

Many mechanisms have been proposed to explain the HE from a nano structural point of view, among them: hydrogen-enhanced decohesion (HEDE) (DJUKIC et al., 2019; GERBERICH et al., 1991; ORIANI; JOSEPHIC, 1974; TROIANO, 2016); hydrogen-enhanced localized plasticity (DJUKIC et al., 2019;

MARTIN et al., 2019; ROBERTSON et al., 2015), and adsorption-induced dislocation emission (LYNCH, 2012), which can occur simultaneously. However, they cannot explain the cracking behavior for all cases. Hence, additional or refined mechanisms are proposed, such as hydrogen-enhanced strain-induced vacancy formation (HESIVF) (NAGUMO, 2004) and hydrogen-enhanced strain-induced phase transformations (HESIPT) (NARITA; BIRNBAUM, 1980).

The understanding of hydrogen embrittlement mechanisms continues to evolve. Advanced characterization techniques like electron microscopy, atom probe tomography, and computational modeling contribute to a deeper understanding of how hydrogen interacts with materials on an atomic and microstructural level. The anisotropy and the random distribution of lattice and defects associated with the study at a nanoscopic level is a challenge to introduce those related mechanisms in mechanical design (WASIM; DJUKIC; NGO, 2021).

Indeed, most of the previous cited models are based on damage mechanisms related to localized plasticity (HELP, AIDE, HESIVF, and HESIPT), only HEDE proposes a model that is not associated with that. Various of these mechanisms can be active simultaneously depending of hydrogen concentration, lattice defects, material conditions, loading rate, chemical potential, crack size, diffusion enthalpy, temperature, and cleavage stress intensity (DJUKIC et al., 2019; GERBERICH et al., 1991; WASIM; DJUKIC; NGO, 2021). To understand which particular mechanism will occur when a steel is loaded inside any given hydrogen environment is a challenging task, which depends on:

- Source of hydrogen (gaseous H_2, H_2S, cathodic polarization, liquid hydrogen, etc.); presence of hydrogen trappings in the microstructure, hydrogen permeation and diffusion, and hydrogen charging.
- Microstructure: Impurities, defects, crystalline structure (austenite, ferrite, etc.);
- Concentration of hydrogen and its distribution in the steel;
- Mechanical loading: Static, dynamic, or cyclic loads causing tensile, bending, or shear stresses.

2.3.1. Hydrogen-enhanced decohesion (HEDE)

Hydrogen-enhanced decohesion (HEDE) is one of the primary mechanisms proposed to explain how hydrogen can lead to the cracking of steels, specifically its tendency to promote brittle fracture. The central idea behind HEDE is that hydrogen atoms, when present at high enough concentrations within a metal, can reduce the cohesive strength between the metal atoms. This weakening occurs primarily near the crack tip or at stress concentration areas, since hydrogen atoms absorbed into a metal's crystal lattice tend to migrate to there. As hydrogen atoms accumulate, they reduce the cohesive force between metal atoms, making it easier for cracks to initiate and propagate (GERBERICH et al., 1991).

High-strength steels rely on strong metallic bonds to provide their strength and toughness. However, when exposed to hydrogen, its atoms can diffuse into the metal. Once inside, they migrate to areas of high stress, such as grain boundaries or dislocations, where the hydrogen reduces the metal resistance to crack propagation (TROIANO, 2016).

This reduction in bond strength between metal atoms occurs due to the alteration of the local electronic structure of the metal by the hydrogen atoms. Hydrogen atoms interact with the electron density at the crack tip, effectively reducing the local electron density and thus the bond strength between metal atoms. This interaction results in a local reduction in the work required to separate atoms, effectively lowering the metal's fracture toughness. Consequently, even under normal service conditions, the metal can fail in a brittle manner, fracturing along the paths of least resistance where hydrogen atoms have congregated (DJUKIC et al., 2019).

Experimental evidence for the HEDE mechanism includes observations of intergranular or quasi-cleavage fracture surfaces after failure, which are indicative of a decohesion process. Additionally, advanced analytical techniques such as electron microscopy and spectroscopy have been employed to visualize the distribution of hydrogen within the metal and at the crack tip, supporting the concept that localized hydrogen concentrations correspond to the sites of fracture (GERBERICH et al., 1991; ORIANI; JOSEPHIC, 1974; WASIM; DJUKIC; NGO, 2021).

2.3.2. Hydrogen-enhanced localized plasticity (HELP)

HEDE and HELP were the primary mechanisms proposed to explain HE in an atomic scale. HELP assumes hydrogen atoms diffuses through the metal lattice and interact with dislocations, reducing the energy barrier for their movements and thus increasing localized plasticity (DJUKIC et al., 2019). Those dislocation movements can be observed through advanced electronic microscope techniques such as transmission electron microscopy (TEM), which allows for the direct observation of dislocations and their interactions with hydrogen atoms. Additionally, the fracture surface of steels exposed to HE exhibits an increase in localized plasticity, as observed through tensile tests performed at a slow strain rates (DJUKIC et al., 2019).

Hydrogen atoms can be attracted to the stress fields around dislocations. As dislocations move through the lattice during plastic deformation, they can drag hydrogen atoms with them. This hydrogen zone around a dislocation can enhance the dislocation mobility, since the hydrogen atoms can locally modify the electronic structure of the metallic lattice and reduce the cohesive strength between atoms, resulting in a decrease in the critical resolved shear stress required for dislocation movements. Consequently, the presence of hydrogen can lead to an increase in the rate of plastic deformation in certain areas, which is the essence of HELP (WASIM; DJUKIC; NGO, 2021).

While this might initially seem beneficial, since plasticity typically opposes brittle failures, it can lead to premature failures in hydrogen environments because the localized nature of the hydrogen-enhanced plasticity can intensify the strains in specific regions. This facilitates the nucleation and growth of micro-voids and ultimately leads to material failure through a ductile fracture process (DJUKIC et al., 2019).

2.3.3. Adsorption-induced dislocation emission (AIDE)

Transmission electronic microscope analyses of the fracture surface of steels exposed to hydrogen sources indicate nucleation of dislocations within the material crystal structure on the cracked surfaces. Adsorption-induced dislocation emission mechanism appear as an alternative to explain this phenomenon (LYNCH, 2012).

When hydrogen atoms come in contact with a metal surface, they can be absorbed into the metal or remain adsorbed on the surface. The adsorbed hydrogen atoms can affect the metal's surface energy and alter the local stress state. Hydrogen weakens the atomic bonds and modifies the electronic structure at the surface, effectively reducing the work of adhesion between the atoms. As a result, hydrogen embrittles the surface, making it easier for dislocation nucleation (LYNCH, 2012).

Dislocation nucleation commonly requires significant energy due to the need to break bonds and form a dislocation core. However, in the AIDE mechanism, the energy barrier for dislocation nucleation is lowered because the adsorbed hydrogen decreases the energy needed to form dislocation in the surface. This lowered energy barrier is especially significant under applied tensile stresses.

Once nucleated, these dislocations can be emitted from the surface into the bulk of the metal. This emission of dislocations is a critical step in the AIDE mechanism because it provides a pathway for plastic deformation to initiate and propagate from the surface into the material's interior. The emitted dislocations can multiply and interact with other dislocations, increasing the local plasticity near the surface. However, if the metal is under an applied load, this localized increase in plasticity can contribute to the formation and growth of micro-cracks that coalesce and lead to brittle fracture (LYNCH, 2012).

3. Introduction to Fracture Mechanics

Defect tolerance approaches for the design of structural components under hydrogen embrittlement conditions are based on fracture mechanics concepts, briefly reviewed following.

3.1. Fundamental Concepts

Fracture mechanics concepts can explain how cracks initiate and propagate in solid materials. To better understand how flaws, notches, and other geometric discontinuities affect the stress state within a material, it is essential to examine the stress concentration factor. This factor plays a critical role in this understanding.

3.1.1. Stress Concentration Factor (K_t)

Most structural elements need to have abrupt variations in their geometry, generically called notches, for operational and/or assembly reasons. Saint-Vénant principle dictates that nominal stress formulas do not apply near such notches, since they can cause significant localized stress-concentration effects, which must be quantified properly, both for structural analysis and for design purposes (CASTRO; MEGGIOLARO, 2016b). Stress concentration factors (K_t) can be used in such cases, in particular when dealing with brittle failures, fatigue, and EAC problems. K_t is defined as the ratio between the maximum stress at the notch tip, σ_{max}, and the nominal stress that would act there, σ_n, if the notch did not affect the stress field around it (CASTRO; MEGGIOLARO, 2016b):

$$K_t = \frac{\sigma_{max}}{\sigma_n} \tag{5}$$

Inglis analyzed stress concentration effects around elliptical holes in flat plates (INGLIS, 1913). He considered a plate large enough so that the stress around the elliptical hole with axes $2a$ and $2b$ was not affected by the plate boundaries. In the simplest case where the applied stress is perpendicular to the axis $2a$, see Fig 6, the stress concentration factor at the point A is given by:

$$\sigma_A = \sigma\left(1 + \frac{2a}{b}\right) = \sigma\left(1 + 2\sqrt{\frac{a}{\rho}}\right), \text{ since } \rho = b^2/a \tag{6}$$

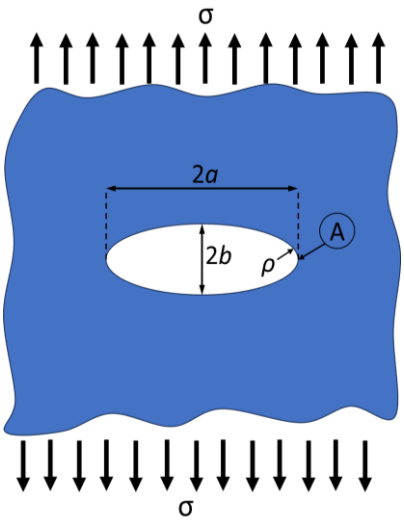

Fig 6. Elliptical hole in a flat plate considered by Inglis to quantify the SCF, K_t. (Source: Created by the author).

Notice that Inglis equation reproduces the Kirsch K_t for a circular hole when $a = b$, for which $K_t = 3$. For elongated notches with $a >> b$, the hole looks like a blunt crack. Inglis model gives good quantitative estimates for the SCF of sharp corners, but it does not apply when the flaws become extremely sharp and $\rho \to 0$, since in such cases $\sigma \to \infty$. Since no material can withstand infinite stresses, the Inglis model would indicate that any material should fail in presence of a sharp crack, even under extremely low applied stresses.

3.1.2. Griffith's Theory of Brittle Fracture

Griffith solved the sharp crack paradox using an energy-based model based on the first law of thermodynamics, the energy conservation principle (GRIFFITH, 1921). Hence, to grow a crack in brittle materials, the cracked component must be able to supply the surface energy required to form the new crack faces (ANDERSON, 2005):

$$\frac{dE}{dA} = \frac{d\Pi}{dA} + \frac{dW_s}{dA} = 0 \Rightarrow -\frac{d\Pi}{dA} = \frac{dW_s}{dA} \tag{7}$$

where:

E = total energy, J

Π = potential energy, J

W_s = work required to form the two crack surfaces, N.m

A = crack surface area, m^2

The potential energy Π stored in the cracked component depends on the internal strain energy and on the forces externally applied on it. Considering the Inglis stress analysis presented in Fig 7 for a plate with thickness B, Griffith express the potential energy for an uncracked plate and the work W_s (ANDERSON, 2005)as follows:

$$\Pi = \Pi_0 - \frac{\pi\sigma^2 a^2 B}{E} \tag{8}$$

and

$$W_s = 4aB\gamma_s \tag{9}$$

Where γ_s represents the surface energy of the material.

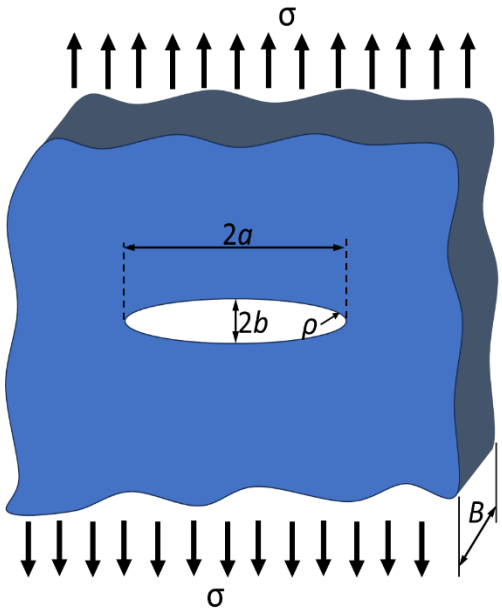

Fig 7. Flat plate considered by Griffith to his model. (Source: Created by the author).

Thus, considering the total crack surface area A = 2 ($a \cdot B$) and solving for the fracture stress (ANDERSON, 2005),

$$-\frac{d\Pi}{dA} = \frac{\pi\sigma^2 a}{E} \tag{10}$$

$$\frac{dW_s}{dA} = 2\gamma_s \tag{11}$$

$$\sigma_f = \sqrt{\frac{2E\gamma_s}{\pi a}} \tag{12}$$

The expressions above as proposed by Griffith are valid only for brittle materials. To extend Griffith's solution for metals and ductile materials, Irwin and Orowan (ANDERSON, 2005) proposed a modified and reviewed version which includes the term γ_p in the equation, giving:

$$\sigma_f = \sqrt{\frac{2E(\gamma_s + \gamma_p)}{\pi a}} \tag{13}$$

where γ_p is the plastic work per unit of crack area A associated with ductile materials. Or in a generalized way representing w_f as the fracture energy associated to any material:

$$\sigma_f = \sqrt{\frac{2Ew_f}{\pi a}} \tag{14}$$

3.2. Energy Approaches in Fracture Mechanics

The energy approach proposed by Griffith plays a very important role in Fracture Mechanics. This section introduces the *energy release rate*, a critical measure of the energy changes associated with crack extension, followed by a discussion of the J-Integral, a path-independent quantity that characterizes the intensity of the stress and strain field near a crack tip.

3.2.1. Energy release rate

Irwin proposed the energy release rate approach in 1956. It is based on the Griffith energy-balance model, therefore, the Irwin's approach introduces the term (potential or strain) *energy relief rate* $\mathcal{G}$, considered as a much more appropriate form to solve engineering challenges (ANDERSON, 2005). $\mathcal{G}$ is also called the *crack driving force*.

$$\mathcal{G} = -\frac{d\Pi}{dA} \tag{15}$$

Which, for the Griffith's plate presented in Fig 7 corresponds to:

$$\mathcal{G} = -\frac{\pi\sigma^2 a}{E} \tag{16}$$

When $\mathcal{G}$ attends to its critical value $\mathcal{G}_c$, which is a material property known as the fracture toughness, the crack extension occurs.

$$\mathcal{G}_c = 2w_f \tag{17}$$

3.2.1. The J contour Integral

In Elastoplastic (EP) cases, the Potential Energy Release Rate **-dΠ/dA** is called **J** instead of $\mathcal{G}$. The J-Integral is used to quantify crack effects under small EP monotonic strains, considered as Non-Linear Elastic. The J-Integral concept was originally proposed by Cherepanov in 1967 (CHEREPANOV, 1967) and Rice in 1968 (RICE, 1968).

Ductile materials exhibit gradual and stable crack growth accompanied by significant plastic deformation. The resistance to crack propagation is attributed to the energy release through plastic deformation around the crack tip, where the plastic zone increases before reaching a consistent growth pattern. This process requires increased external forces to sustain stable crack growth.

The J-R curve quantifies these phenomena, plotting the relationship between stable crack propagation (Δa) and the J-integral. The resistance to ductile crack propagation in materials, such as steel, is characterized by the slope dJ/da. Crack growth is accompanied by elastic unloading, leading to non-proportional plastic deformation in the vicinity of the crack tip. This implies the strict application of the J integral in the analysis of stationary cracks. Nevertheless, if nearly proportional loadings occur anywhere except in the immediate vicinity of the crack tip, J can be used to analyze crack growth. However, additional conditions must be provided for J-controlled crack growth to be satisfied. The J-Integral can be interpreted as the rate of potential energy relief related to the variation in crack length as illustrated in Fig 8. Since the Potential Energy is given by:

$$\Pi = U1 - P\Delta = -U2 \tag{18}$$

where, Π is the potential energy, $U1$ is the strain energy stored in the body, U2 is the potential energy relief, P and Δ are respectively the load and displacement associated with a cracked plate with a non-linear behavior.

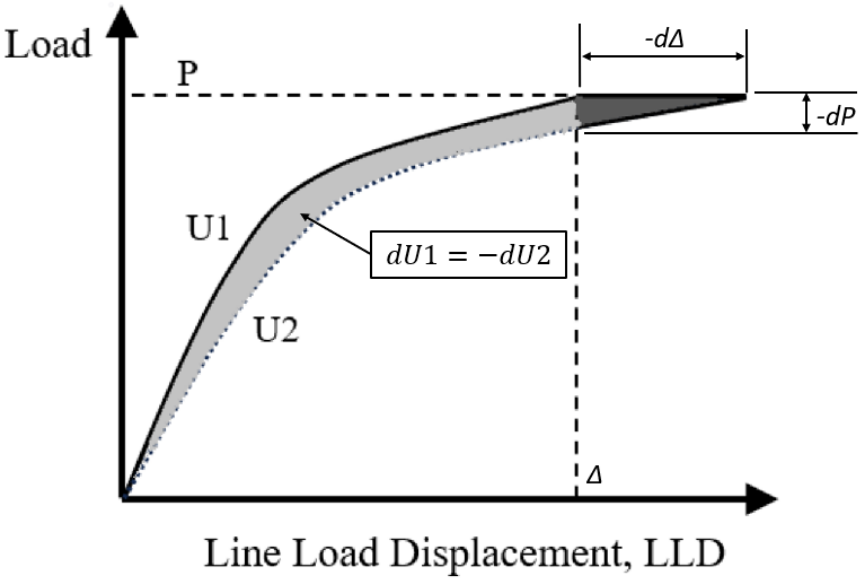

Fig 8. Non-linear Energy release rate. Adapted from (ANDERSON, 2005)

For a two-dimensional elastic concept, it is given by (ANDERSON, 2005):

$$J = \int_{\Gamma} \left(w dy - \underline{T_i} \frac{\partial \underline{u_i}}{\partial x} ds \right) \tag{19}$$

where, $\underline{T_i}$ are the components of the traction vector, $\underline{u_i}$ are the displacement vector components, w is the strain energy density, and $d\boldsymbol{s}$ is the length increment along the contour Γ.

$$w = \int_0^{\varepsilon_{ij}} \sigma_{ij} d\varepsilon_{ij} \tag{20}$$

3.3. Fracture Toughness

Fracture toughness quantifies the material's resistance to crack growth. There are many standard methods to quantify fracture toughness, either in normal ambient conditions or inside corrosive environments (ASTM E399, 2022; ASTM E1681, 2023; ASTM E1820-23B, 2023). This property is fundamental in the design and assessment of structural components.

This section begins presenting the three modes of fracture followed by a discussion of the Stress Intensity Factor (SIF), which describes stress fields around crack tips and serves as a critical parameter in fracture toughness analysis. Then it presents the Resistance Curve, or R-curve, which provides insight into the changes in material toughness as the crack grows.

3.3.1. Modes of Fracture

Cracks can grow under three basic loading modes, which affect the stress field around their tips and the fracture process differently. It is necessary to understand these different loading modes to analyze and to predict the crack behavior under various loading conditions. These three modes are, see Fig. 9:

- Mode I – The normal or opening Mode, with tensile loads applied perpendicular to the crack surface,
- Mode II – The sliding mode, with shear loads applied parallel to the crack surface, and
- Mode III – The tearing Mode, with torsion or shear loads parallel to the crack surface and to its front.

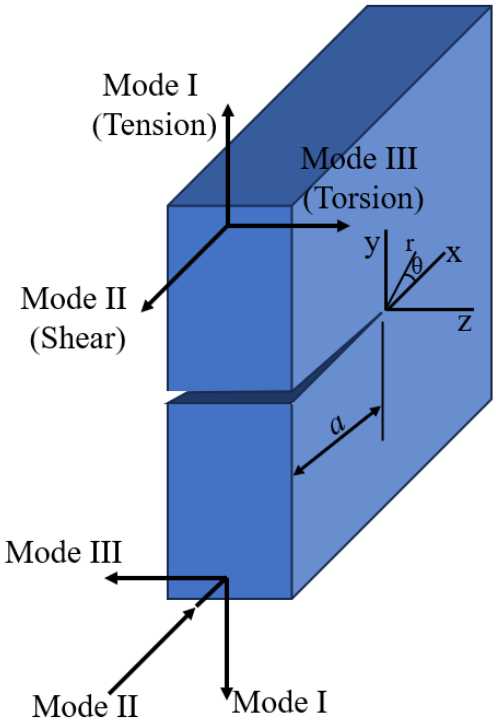

Fig 9. Three basic modes of load any cracked structure. (Source: Created by the author).

3.3.2. Stress Intensity Factors

Irwin extended Griffith's energy approach by introducing the Stress Intensity factor (SIF) to describe stress fields near the tip of a crack in linear elastic materials. This approach also includes ductile materials, when the plastic zone around the

crack tip is small and most of the stress field remains linear elastic (CASTRO; MEGGIOLARO, 2016a).

Any cracked structural components in isotropic, homogeneous, and linear-elastic conditions have their stress fields around the crack tip controlled by the stress intensity factor. 2D stress fields in modes I, II, and III are given by equations (21), (22), and (23) respectively (CASTRO; MEGGIOLARO, 2016a).

$$\begin{aligned}\left(\sigma_x\ \sigma_y\ \tau_{xy}\right) = \frac{K_I}{\sqrt{2\pi r}} \\ cos\ cos\left(\frac{\theta}{2}\right)\left\{1 - sin\ sin\left(\frac{\theta}{2}\right)\ sin\ sin\left(\frac{3\theta}{2}\right)\ 1 + \right. \\ sin\ sin\left(\frac{\theta}{2}\right)\ sin\ sin\left(\frac{3\theta}{2}\right)\ sin\ sin\left(\frac{\theta}{2}\right) \\ \left. cos\ cos\left(\frac{3\theta}{2}\right)\right\}\end{aligned} \tag{21}$$

$$\begin{aligned}\left(\sigma_x\ \sigma_y\ \tau_{xy}\right) = \frac{K_{II}}{\sqrt{2\pi r}} \\ cos\ cos\left(\frac{\theta}{2}\right)\left\{1 - sin\ sin\left(\frac{\theta}{2}\right)\ sin\ sin\left(\frac{3\theta}{2}\right)\ 1 + \right. \\ sin\ sin\left(\frac{\theta}{2}\right)\ sin\ sin\left(\frac{3\theta}{2}\right)\ sin\ sin\left(\frac{\theta}{2}\right) \\ \left. cos\ cos\left(\frac{3\theta}{2}\right)\right\}\end{aligned} \tag{22}$$

$$\left(\tau_{xz}\ \tau_{xy}\right) = \frac{K_{III}}{\sqrt{2\pi r}}\left\{- sin\ sin\left(\frac{\theta}{2}\right)\ cos\ cos\left(\frac{\theta}{2}\right)\right\} \tag{23}$$

The xy cartesian and polar rθ coordinates shall be centered in the crack tip. In mode I, the general form for it is given by (CASTRO; MEGGIOLARO, 2016a):

$$K_I = \eta\ \sigma\ \sqrt{\pi a}\ f(a/w) \tag{24}$$

Where, σ is the nominal stress applied, *a* is the crack length, η quantifies free surface and notch effects, and *f(a/w)* is a non-dimensional function describing the crack geometry and loading conditions.

Fig 10 describes each K_I equation term, the image on the left of the figure depicts the Stress Intensity Factor (SIF) for an infinite plate under Mode I. Following this, the effect of a free surface is included, and on the far right, the SIF for a body with a surface crack is shown.

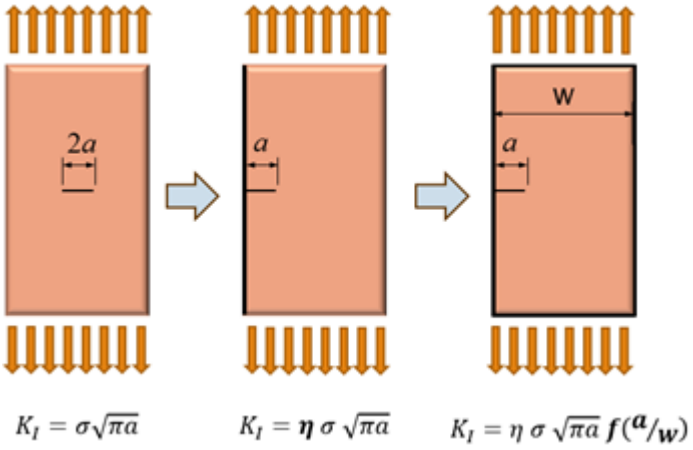

Fig 10. General equation for the stress intensity factor in mode I. (Source: Created by the author).

Structural materials are not linear-elastic at high stresses. However, if the plastic zones that always form around loaded crack tips are small compared to the cracked component dimensions, the stress intensity factor can still be used to quantify crack effects. Equation (25) estimates the plastic zone size in Mode I.

$$\sigma_y(r = pz, \theta = 0) = S_y \rightarrow pz \cong \frac{{K_I}^2}{2\pi\left({S_y}^2\right)} \qquad (25)$$

Fracture of tough components, associated with large plastic zones, cannot be described by LEFM. In many cases tough fractures can be modeled by elastoplastic fracture mechanics (EPFM) concepts, such as the Crack Tip Opening Displacement (δ), the J-Integral value, the J-R curve, or a Failure Assessment Diagram (FAD).

Under LEFM conditions, the material property fracture toughness can be associated with a critical value stress intensity factor. In mode I, K_{IC} represents the threshold value of the stress intensity factor above which a material with a pre-existing flaw will fail due to unstable crack propagation.

To understand how the material resistance to crack growth varies along the crack path, the resistance can be plotted against the crack length increment Δa. This graphical approach is known as the R-curve or the Resistance curve.

3.3.3. Resistance curves or R-curves

The resistance curve is a way to represent how the material resistance to crack propagation varies with the crack size. Since equation (17) must be satisfied to allow crack growth, the material resistance to crack growth R is equal $2w_f$ and the

R-curve corresponds to the plot of R versus crack extension Δa (ANDERSON, 2005).

Cracked materials present two fracture behaviors, as shown in Fig 11.

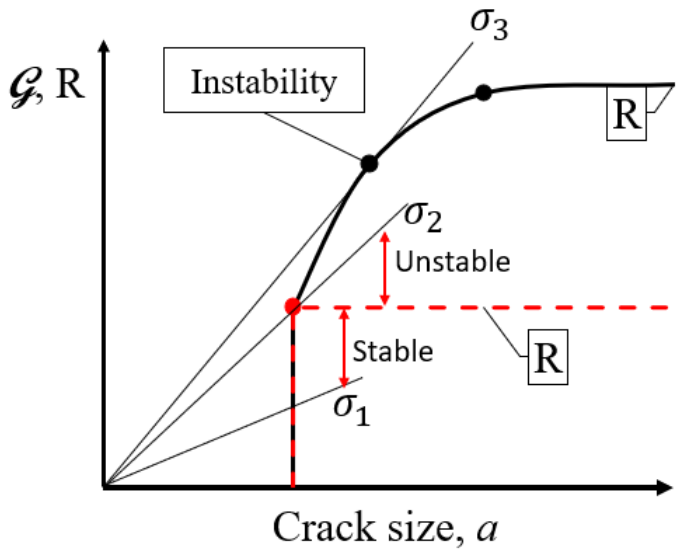

Fig 11. Driving force versus R curve, flat R curve as red dash line and a rising R curve as a continuous black line. (Source: Created by the author).

The first, when the fracture resistance is independent of the crack increment Δa and the crack propagate unstably when $\mathcal{G}$ reaches $\mathcal{G}_c$. The second, when the fracture resistance is dependent on the crack increment Δa and presents an increasing R curve while the crack grows stably until reaching a critical value $\mathcal{G}_c$, when the crack propagates unstably (ANDERSON, 2005).

3.4. Estimation of stress concentration factors from linear elastic fracture mechanics (LEFM) concepts, the Creager and Paris approach.

From well stablished solutions for the stress intensity factor (SIF), Creager and Paris proposed a method in 1967 (CREAGER, 1967) to estimate the stress concentration factor (K_t) for crack-like notches. In such cases, they demonstrated that by considering the tip radius (ρ) displaced by ρ/2 towards the interior of the notch and the origin of the r and θ axes, it becomes feasible to estimate the stress field around the tip of the notches. Hence, as proposed by them, the stress concentration factor is given by:

$$K_t \cong \frac{2K_I}{\sigma_n\sqrt{\pi\rho}} \tag{26}$$

3.4.1. The Notch sensitivity effect (*q*)

Originally, the concept of notch sensitivity focused in explaining the of structures under cyclic loads, when the material does not fracture by fatigue even above the fatigue limit in the presence of a notch-induced stress concentration field (CASTRO; MEGGIOLARO, 2016b). Aiming to quantify the real impact of notches on fatigue limits, the q factor given by the relation between K_f and K_t, where K_f is the actual stress concentration factor associated to the fatigue limit, which was empirically obtained (CASTRO; MEGGIOLARO, 2016b).

$$K_f = 1 + q(K_t - 1) = \frac{\Delta\sigma_0}{\Delta\sigma_f} \tag{27}$$

where $\Delta\sigma_0$ is the fatigue limit obtained in a smooth specimen and $\Delta\sigma_f$ is the fatigue limit of a notched specimen.

The difference between K_f and K_t is associated to the presence of small non-propagating fatigue cracks found at notch tips when $\frac{\Delta\sigma_0}{K_t} < \Delta\sigma_n < \frac{\Delta\sigma_0}{K_f}$ (MEGGIOLARO; MIRANDA; CASTRO, 2007). To quantify the effect of very small fatigue crack sizes, El Haddad, Topper and Smith proposed a *characteristic small crack size* a_0 (EL HADDAD; TOPPER; SMITH, 1979) to modify the SIF range ΔK_I of a cracked infinite plate loaded in mode I (Irwin's plate) reproducing the Kitagawa-Takahashi diagram behavior.

$$\Delta K_I = \Delta\sigma\sqrt{\pi(a+a_0)}, \qquad where\ a_0 = \frac{1}{\pi}\left(\frac{\Delta K_{th0}}{\Delta S_{L0}}\right) \tag{28}$$

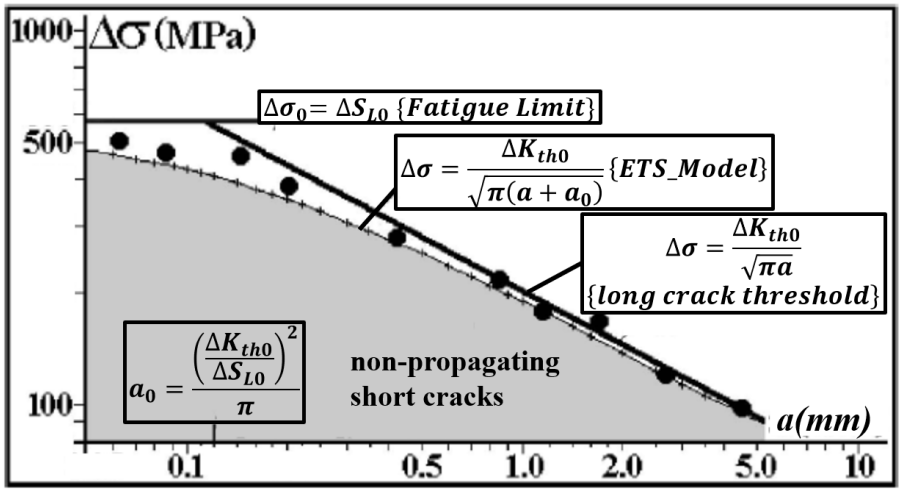

Fig 12. Kitagawa Takahashi diagram, modified from (CASTRO; MEGGIOLARO, 2016a)

As illustrated in Fig 12, small fatigue cracks can initiate but they will not propagate while they remain below the ETS model as described in equation (28). The ETS model unifies the different behavior of short and long fatigue cracks. The crack size-dependent fatigue crack growth threshold $\Delta K_{th}(a)$ can be generalized by including Bazant's coefficient (MEGGIOLARO; MIRANDA; CASTRO, 2007):

$$\frac{\Delta K_{th}(a)}{\Delta K_0} = \left[1 + \left(\frac{a_0}{a}\right)^{\frac{n}{2}}\right]^{-\frac{1}{n}} \tag{29}$$

3.4.2. Notch sensitivity effects in corrosion (q_c)

Similar to the fatigue approach, notch sensitivity factors for environmentally assisted cracking (q_c) can be calculated departing from two material properties obtained in the corrosive environment, S_{EAC} and K_{IEAC}, which can be measured through proper standardized tests. As proposed by Castro et al. (CASTRO; LANDIM; MEGGIOLARO, 2015; CASTRO; MEGGIOLARO, 2014) for EAC, a characteristic crack size for a non-propagating small crack is given by:

$$a_0 = \frac{1}{\pi}\left(\frac{K_{IEAC}}{\eta\, S_{EAC}}\right)^2 \tag{30}$$

where, a_0 is the characteristic short crack size under EAC, K_{IEAC} is the stress intensity factor threshold measured in a corrosive environment, S_{EAC} is the ultimate tensile Strength (UTS) measured in a corrosive environment, $\eta = 1.1215$ is a correction factor for a free surface.

Small cracks do not propagate while the applied loading remains below the limit curves seen in Fig 13.

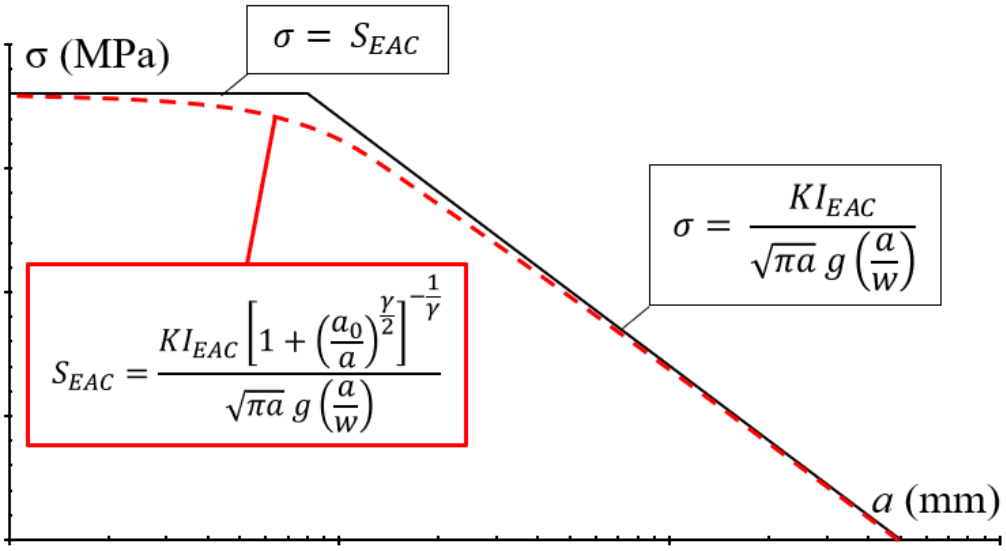

Fig 13. Short and long crack behavior for EAC conditions. Adapted from (CASTRO; LANDIM; MEGGIOLARO, 2015).

From the Creager and Paris model (EL HADDAD; TOPPER; SMITH, 1979), an *f(a)* and *g(a)* function can be estimated as follows.

$$f(a) = \frac{K_I(a_0)}{\sigma_n \sqrt{\pi(2a+\rho)}}\left(1 + \frac{\rho}{2a+\rho}\right) \tag{31}$$

$$K_{Ith} = \eta\, g\left(\frac{a}{\rho}, K_{tc}\right)\sigma\sqrt{\pi(a)} \tag{32}$$

where $g\left(\frac{a}{\rho}, K_{tc}\right)$ is the crack growth limit on the stress field ahead the notch root.

$$g(a, K_{tc}) = \frac{\frac{K_{IEAC}}{\sigma\sqrt{\rho}} K_{tc}}{\left[\left(\eta\sqrt{\frac{\pi a}{\rho}}\right)^{\gamma} + \left(\frac{K_{IEAC}}{\sigma\sqrt{\rho}}\right)^{\gamma}\right]^{\frac{1}{\gamma}}} \tag{33}$$

Then, solving the equation system 34 to obtain x_{max} and K_{tc}.

$$\begin{cases} f(x_{max}) = g(x_{max}, K_{tc}, \gamma) \\ \frac{d}{dx} f(x_{max}) = \frac{d}{dx} g(x_{max}, K_{tc}, \gamma) \end{cases} \tag{34}$$

q_c can be obtained from:

$$q_c = \frac{K_{tc} - 1}{K_t - 1} \tag{35}$$

4. Tolerance to short cracks under EAC conditions

Failures of notched structural components either by fatigue or by EAC depend on the stress gradient ahead of the notch tip, and on the material resistances to crack initiation and growth, which control their tolerance to short cracks (CASTRO et al., 2015). The apparently odd behavior of cracks that start at notch roots and stop after growing for a while is easy to explain. It is due to the competition between the decreasing stress and the increasing crack size ahead of the notch tip on the crack SIFs. When the crack driving force (its SIF) becomes smaller than $\Delta K_{th}(a)$, the crack stops.

Non-propagating short cracks can also be found in smooth surfaces subjected to suitable stress gradients, induced e.g. by bending or torsion, by point loads, by thermal stresses, by residual stresses, by corrosion pits, or by any other cause (MEGGIOLARO; MIRANDA; CASTRO, 2007). In the same way high-enough stresses can start cracks at critical points, high-enough stress gradients can turn them in tolerable non-propagating cracks (MEGGIOLARO; MIRANDA; CASTRO, 2007).

To quantify such effects clearly, Castro, Liu, and Miranda (LIU et al., 2023) proposed to split SIFs into four parts, including a K_{gr} term to consider stress gradient effects on it explicitly, see equation (36) for the fatigue case. This model can be extended to EAC as in equation (37). Notice that $K_{gr}(a \rightarrow 0) \rightarrow K_t$.

$$\Delta K = \eta.\Delta K_{gr}(a/w).\Delta\sigma\sqrt{\pi(a+a_0)}, \qquad a_0 = (1/\pi).\left[\Delta K_{th_0}/\eta.S_{L_0}\right]^2 \tag{36}$$

$$K = \eta.K_{gr}(a/w).\sigma\sqrt{\pi(a+a_0)}, \qquad a_0 = (1/\pi).\left[K_{EAC_0}/\eta.S_{EAC_0}\right]^2 \tag{37}$$

where $\sigma\sqrt{(\pi a)}$ and $\Delta\sigma\sqrt{(\pi a)}$ are the reference SIF and SIF range (for static and cyclic loads), $\eta = 1.12$ quantifies the free surface effect, $K_{gr}(a/w)$ the stress gradient effect, f(a/w) the geometry (of the crack and of the cracked piece) effect, and a_0 is the short crack characteristic size.

This study aims to understand the mechanical behavior of mechanically short cracks, thus the methodology proposed here does not apply for very cracks in scale of the grain size. As studied in section 3.4.2, LEFM can model the mechanical

behavior of short cracks under EAC conditions, using their stress field, and the material resistances to crack initiation (S_{EAC}) and to crack propagation (K_{EAC} (a)). It is also important to emphasize the LEFM limits: stress field predominantly linear elastic, isotropic and homogeneous materials. Short cracks under EAC conditions can behave in three ways (LIU et al., 2023), see Fig 14:

a) Continuous crack propagation, when its SIF K_I (in mode I) is always above the crack dependent SIF threshold for EAC ($K_{IEAC}(a)$).

b) Non-propagating short cracks, which start with $K_I(a) > K_{IEAC}(a)$ but due to high enough stress gradients $K_I(a)$ decreases as the crack grows until reaching $K_I(a) < K_{IEAC}(a)$, when the crack stops to propagate.

c) Unstable point, when $K_I(a) = K_{IEAC}(a)$ but small disturbances in the stress field can be enough to make the crack continue to propagate. This unstable point determines the maximum non-propagating crack size (a_{max}) tolerable by the cracked piece for any load level.

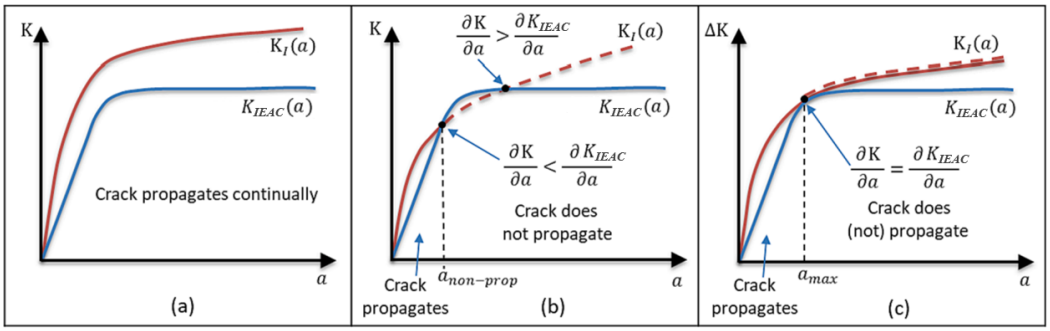

Fig 14. Mechanical behavior of short cracks: (a) crack propagates up to fracture, (b) crack nucleate and stop to propagate when crossing the material resistance curve, (c) crack can propagate up to its unstable non-propagating crack size a_{max}. Modified from (LIU et al., 2023)

On the next sections, the proposed short crack tolerance model is tested under different EAC mechanisms, which follow a similar mechanical behavior. This study includes a low alloy steel and a supermartensitic stainless steel exposed to H_2S, and an aluminum alloy embrittled by liquid gallium. All tests have been performed in the Laboratory of Stress Corrosion Cracking, H_2S, and CO_2 from National Institute of Technology in Rio de Janeiro, Brazil.

4.1. Tolerance to short crack under Liquid Metal Embrittlement

To test short crack tolerance predicted by the model previously presented, tests were made first in an Al 2024 – liquid gallium pair at 35ºC (Ga is liquid above 30ºC), whose main advantage is its very quick liquid metal embrittlement reactions,

in the order of minutes. In comparison, EAC-sensitive Al alloys may take weeks to crack in NaCl-water solutions. Moreover, contrary to other liquid metals that may cause LMIE like mercury, Ga is a safe, non-toxic material. LMIE may occur in solid metal–liquid metal couples that form simple eutectic phase diagrams without any intermetallic phase. LMIE leads to low levels of crack nucleation and propagation thresholds, with reported values of K_{IEAC} as low as 0.1MPa√m and propagation velocity as fast as 0.1m/s. Whereas EAC in aqueous environment involves metal oxidation at anodic sites and an electrical current flow between anodic and cathodic sites that causes loss of metal and local dissolution at the crack tip, LMIE does not involve oxidation reactions because the very high electrical conductivity of liquid metals does not allow for separation between locally anodic and cathodic sites.

4.1.1. Materials and Methods

A 12.7mm thick plate of a 2024 aluminum alloy obtained in a T351 heat treatment, with analyzed chemical composition as described in Table 5.

Table 5. Chemical composition of Al 2024 T351

Element	Al	Si	Fe	Cu	Mn	Mg	Cr	Zn	Zr	Other
Content (%w/w)	Bal.	0,12	0,16	4,44	0,54	1,35	0,02	0,18	0,01	<0,05

However, it had first to be annealed to remove its residual stresses, since in the original as-received plate condition the Ga environment would induce the test specimens to break during manipulation, spoiling all attempts to properly measure the EAC properties of this pair. All test specimens were cut on the TL direction of the plate, identified by standard metallographic procedures as seen in Fig 15.

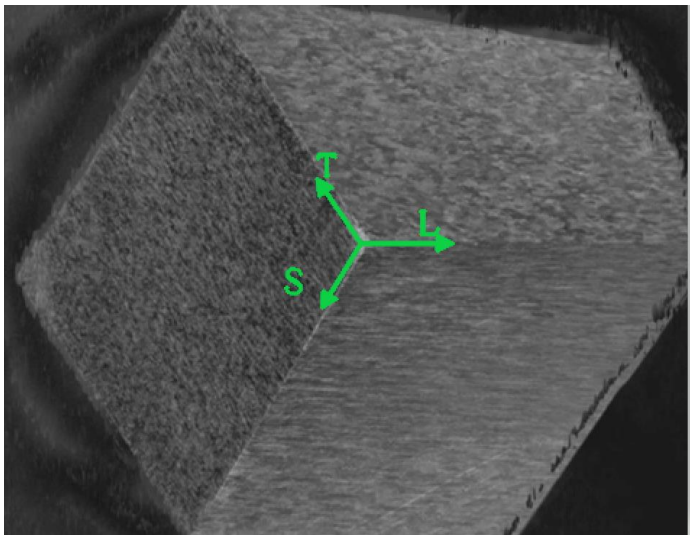

Fig 15. Transversal (T), Longitudinal (L), and Short (S) orientation from the Al plate as received, etched according to ASTM E340(ASTM E340, 2015).

EAC sensibility and reaction rates of the Al-Ga pair were qualitatively evaluated also at 35ºC in very slow $d\varepsilon/dt = 4.5 \cdot 10^{-8}/s$ strain rate tension tests made in a servo-controlled electromechanical testing machine, following ASTM G129 (2021) and NACE recommendations. The liquefied Ga was applied on the test specimen surfaces with a brush, and light bulbs were used to maintain the warm 35ºC temperature during the tests. To guarantee that the exposure time was long enough to ensure the full LME reactions, the time necessary to propagate a crack in the annealed Al 2024 - liquid Ga pair was double-checked by testing pre-cracked C(T) specimens like those used to measure K_{IEAC}. To do so, two pre-cracked specimens were tested under $12MPa\sqrt{m}$ and failed in less than 3 hours. Then two other similar specimens were tested under $7.5MPa\sqrt{m}$ and did not fail after 2 days.

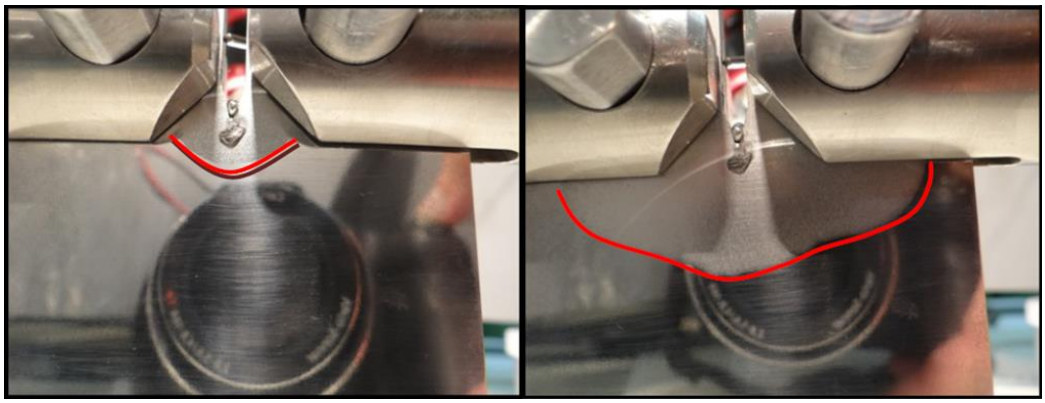
Fig 16. Galium at 35ºC applied at the cracked specimen, after 1 hour on the left and after 3 hours on the right

Following standard procedures and assuming that the incubation time should be a value close to 3 hours, a preload of $7.5\ MPa\sqrt{m}$ was applied for 1 day on the test specimens used to measure K_{IEAC}. Similarly, a pre-load of $30\ MPa$ was applied

for 1 day on the test specimens used to measure S_{EAC}. Then the basic EAC resistances were measured using small incremental load steps induced by calibrated load rings following ASTM E1681 (2023), ASTM F1624(2018), and ISO 7539 (ISO 7539-4, 1989; ISO 7539-9, 2021) standard procedures: S_{EAC} tests started at *30 MPa* and *2.5 MPa* steps, while K_{IEAC} tests initiated at *7.5 MPa* $\sqrt{m}$ and *0.25 MPa* $\sqrt{m}$ steps. The time between successive load steps was at least one hour.

Finally, using these standard EAC properties, four pairs of C(T)-like notched test specimens were ***designed*** to support a maximum local stress at their notch tip $\sigma \cong 90MPa > 2S_{EAC}$. The dimensions chosen for such notches were *{b, ρ, b/w} = {20mm, 0.5mm, 0.33}, {12mm, 0.5mm, 0.2}, {20mm, 0.2mm, 0.33}, {40mm, 4.5mm, 0.67},* respectively for specimens called TS1-TS2, TS3-TS4, TS5-TS6, and TS7-TS8, where *b* and ρ are the notch depth and tip radius, and *w* is the specimen width, with both *b* and *w* measured from the load line.

The idea was, of course, to study the effect of different combinations of their stress concentration factor K_t and stress gradient ahead of the notch tip to assure tolerance to the short cracks that should start at the tips of their notches, since they all were loaded well above S_{EAC}. The (different) loads applied on each one of such notched test specimens were maintained for at least 48 hours, a time much longer than the time required to measure the material resistances to EAC, see (CASTRO et al., 2015) for further details.

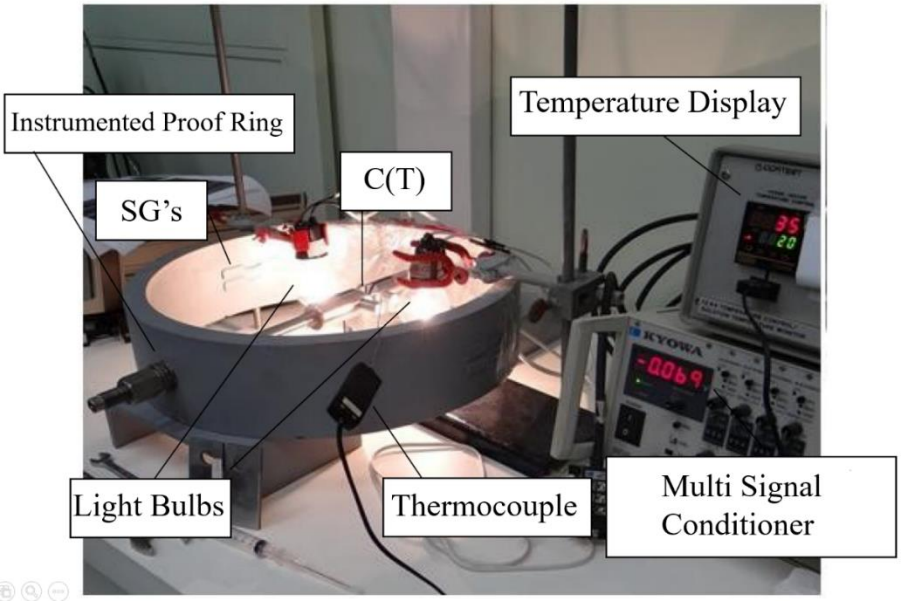

Fig 17. Instrumented Proof ring test system.

4.1.2. Results and discussion

The basic mechanical properties of the annealed Al 2024 alloy were measured by ASTM E8M procedures at 35ºC, resulting in $E = 70\ GPa$, $YS = 113\ MPa$, $UTS = 240\ MPa$, and ultimate strain $\varepsilon_U = 16\%$ as described in Table 6.

Table 6. Mechanical properties of Al 2024 T351

Sample	E, MPa	YS, MPa	UTS, MPa	εu, mm/mm
Al_Tensile Specimen 2	70,300	112.2	242.5	0.174
Al_Tensile Specimen 4	69,519	111.6	238.5	0.160
Al_Tensile Specimen 5	70,457	115.9	238.1	0.143
C(3 ; 95%)	70,092 ± 1,248	113.3 ± 2.3	239.7 ± 2.4	0.159 ± 0.016

The EAC resistances measured by such standard procedures were $S_{EAC} = 43.6 \pm 4.2\ MPa$ (average of *9* samples, with *95%* reliability) and $K_{IEAC} = 8.8 \pm 0.3\ MPa\sqrt{m}$ (*8* samples, *95%* reliability).

Despite being submitted to a much longer exposure than that required to measure S_{EAC} and K_{IEAC} according to standard procedures, none of the designed notched C(T)-like specimens failed during the tests, exactly as predicted (beforehand, during their design stage). Fig 18 shows some of the unbroken notched test specimens after being loaded for a period 50 times longer than the one required for the standard S_{EAC} measurements by a maximum local stress at the notch tip higher than ***twice*** the material resistance to crack initiation under EAC conditions.

After 48 hours immersion period, a time much longer than the time required to measure the material resistances to EAC, the test samples depicted in Fig 18 were examined. These samples all had a width $w = 60mm$ and, from top to bottom, with $\{b, \rho, b/w\} = \{20mm, 0.5mm, 0.33\}$, $\{12mm, 0.5mm, 0.2\}$, $\{20mm, 0.2mm, 0.33\}$, and $\{40mm, 4.5mm, 0.67\}$. They were tested under a peak stress $\sigma_{max} \cong 90MPa > 2 \cdot S_{EAC}$ at the notch tip, or ***twice*** the stress that would lead un-notched specimens to fail by EAC.

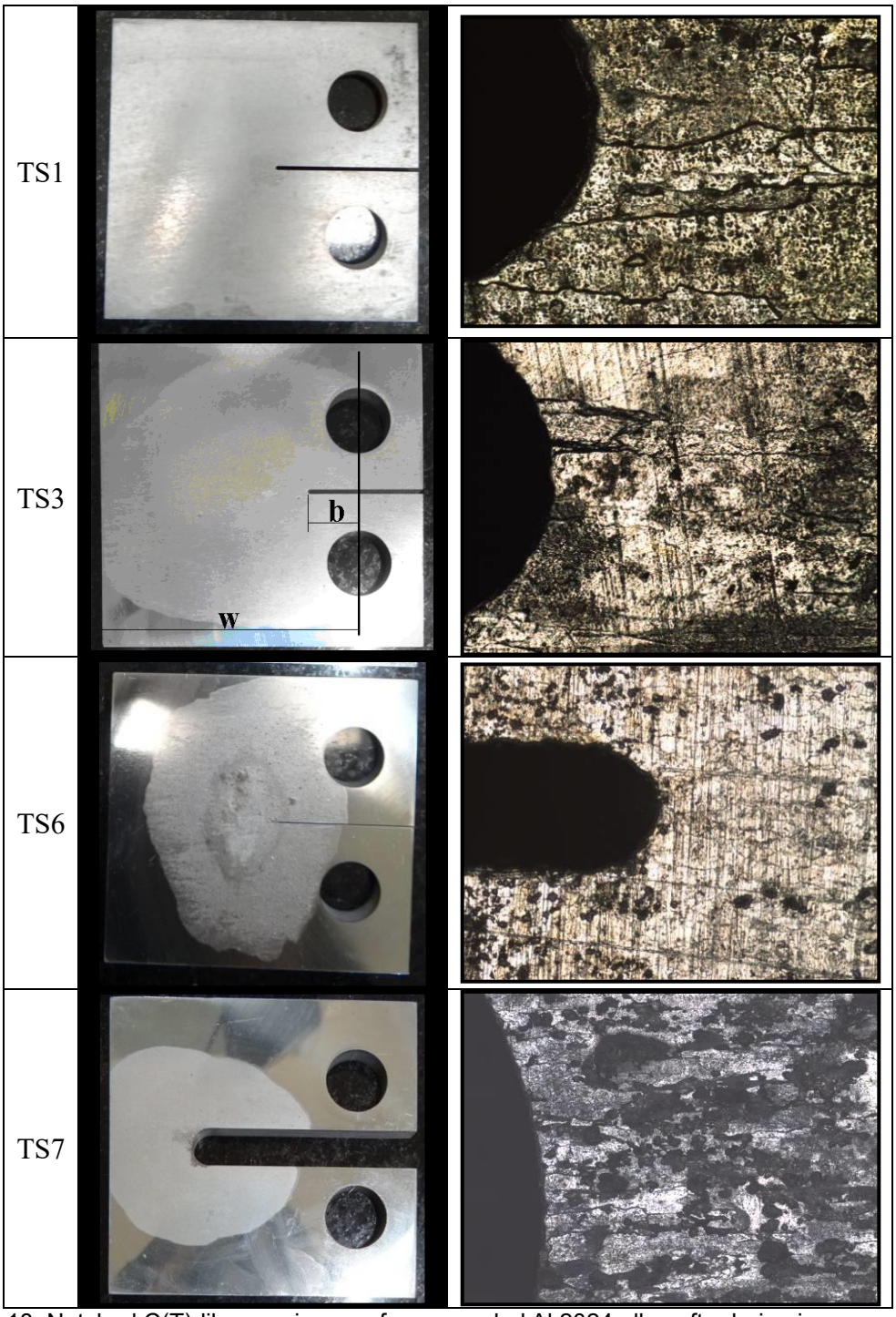

Fig 18. Notched C(T)-like specimens of an annealed Al 2024 alloy after being immersed in liquid Ga for 48 hours.

Specimens TS1 and TS3 clearly indicate the presence of some cracks around the notch. However, for specimen TS6 the evidence is not as clear, and for TS7, significant corrosion makes it difficult to analyse the surface under an optical microscope (Fig 18).

Needless to say, since the chance of 8 specimens tolerating stresses twice higher than the stress needed to start and propagate cracks in un-notched specimens

is very low, this can be seen as strong experimental evidence that the method presented here can indeed be useful to evaluate the tolerance to short cracks that depart from notch tips under EAC conditions. The idea that the mechanical behavior of the short cracks shall be similar for any EAC mechanism, it is now evaluated under hydrogen embrittlement conditions.

4.2. Tolerance to short cracks under Sulfide Stress Corrosion Cracking

The short crack tolerance under hydrogen embrittlement conditions is the core of this work. The use of H_2S as the hydrogen source was chosen due to its faster crack growth rates than in pure hydrogen environments. Sulfide stress corrosion cracking (SSCC) is usually accepted to be a form of hydrogen embrittlement (HE), where the cracking process can be induced by tensile stresses in a susceptible material immersed in an aggressive media containing sufficient amounts of free atomic hydrogen (LANDIM et al., 2023). In the oil and gas industry, in marine applications, and in other organically enriched sediments where the reduction of sulfate ions caused by sulfate-reducing bacteria can produce sufficient H_2S, this gas is commonly associated with HE in high strength low alloy (HSLA) steels. Known as an acidic gas, the H_2S at low pH is stable and can form some acidic solutions after dissolved in aqueous environments (KANE; CAYARD, 1998).

4.2.1. AISI 4140 steel under SSCC

Standard laboratory tests performed with a material previously known to be SSCC susceptible, the AISI 4140 steel, to verify whether its crack initiation threshold under SSCC conditions was low enough as in the LMIE tests made before, say $S_{EAC} < YS/2$. The idea was to validate the model predictions by applying a local tensile stress at notch tips about twice as high as S_{EAC} like in the Al-Ga pair tested before, but maintaining LEFM conditions without failure.

4.2.1.1. Materials and Methods

The aggressive environment was an aqueous solution containing 5 wt% sodium chloride, 2.5 wt% of glacial acetic acid (CH_3COOH), and 0.41 wt% sodium

acetate (CH_3COONa), referenced as solution B in the NACE TM0177(2016) standard, with pH range 3.4-3.6 at 1 bar total pressure, and with partial pressure of H_2S and CO_2 equal to 125 mbar and 875mbar, respectively, at room temperature. The AISI 4140 steel was received as a round bar, with nominal chemical composition as per Table 7

Table 7. Chemical composition of AISI 4140

Element	Fe	Cr	Mn	C
Content (%w/w)	Bal	0.8-1.1	0.75-1.0	0.38-0.43
Element	Si	Mo	S	P
Content (%w/w)	0.15-0.35	0.15-0.25	≤0.04	≤0.03

The basic material tensile properties, measured following ASTM E8M (2022) standard procedures at 25ºC ± 1°, were *YS = 670 MPa* and *UTS = 976 MPa*.

First the crack initiation threshold S_{EAC} (which quantifies the basic resistance of this material-environment pair to SSC or HE conditions) was prospected by using small incremental load steps, following ASTM F1624 (2018) standard procedures. The test was performed in a servo electromechanical machine following a 10/10/2,4 load profile, with 10 initial load steps of 2 hours holding time, followed by 10 load steps of 4 hours holding time.

To ensure that the test condition reproduces the same anodic and cathodic reactions for all tests, the dissolved oxygen was removed by purging the solution and the test vessel for 2 hours per liter with 99,999% pure nitrogen gas before the specimen was immerse into the aggressive solution.

As the test vessels must be inert to the test environment, they were made in glass and PTFE, see Fig 19. After the purge the anaerobic solution was transferred to the test vessel, and the saturation with the test gas was performed for 2 hours. After this, a film developed at the specimen surface, and the cathodic reaction could be visualized by the H_2 bubbles it produces on the specimen surface, see Fig 20.

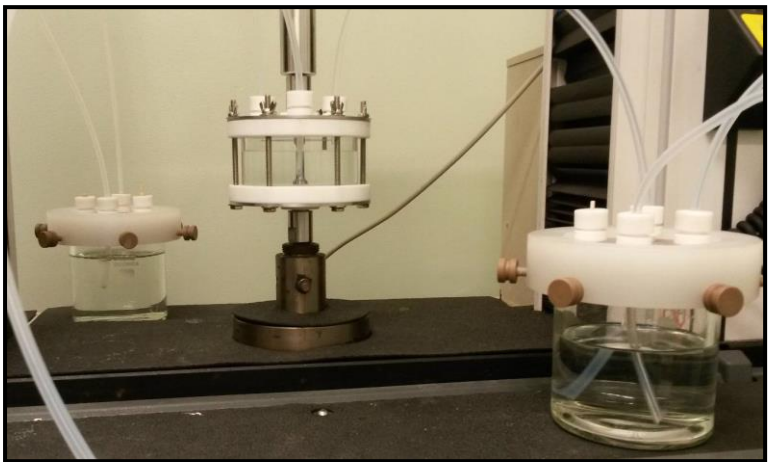

Fig 19. Servo electro-mechanic machine used for the incremental 10/10/2,4 tensile tests; used to measure the basic resistance to crack initiation under EAC, S_{EAC}.

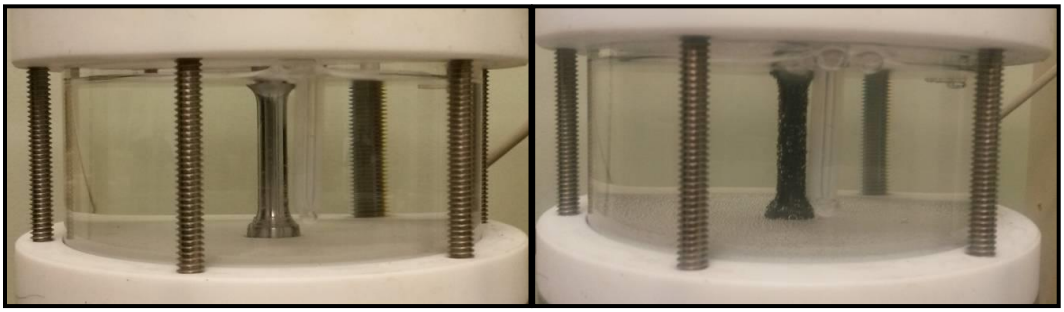

Fig 20. 4140 steel specimens immersed into the anaerobic solution after the purge (left); and the same specimen after saturation, showing the cathodic reaction generating H_2 bubbles on the specimen surface (right).

The crack propagation threshold for this SSC conditions was measured using standard NACE TM0177(2016) method D procedure, by testing four side-grooved Double Cantilever Beam specimens machined by wire electrical discharge to avoid residual stress, see Fig 21.

These specimens were immersed in the hydrogenated anaerobic test solution for 14 days and loaded by double tapered wedges in order to provide a crack mouth displacement $\delta = 0.63$mm, using all precautions adopted in the step loading tests to avoid oxygen contamination. After the test, the specimens were loaded in a servo electro-mechanical machine to obtain the equilibrium wedge-load (P). Finally, the specimens were broken in liquid nitrogen to measure the crack, see Fig 22.

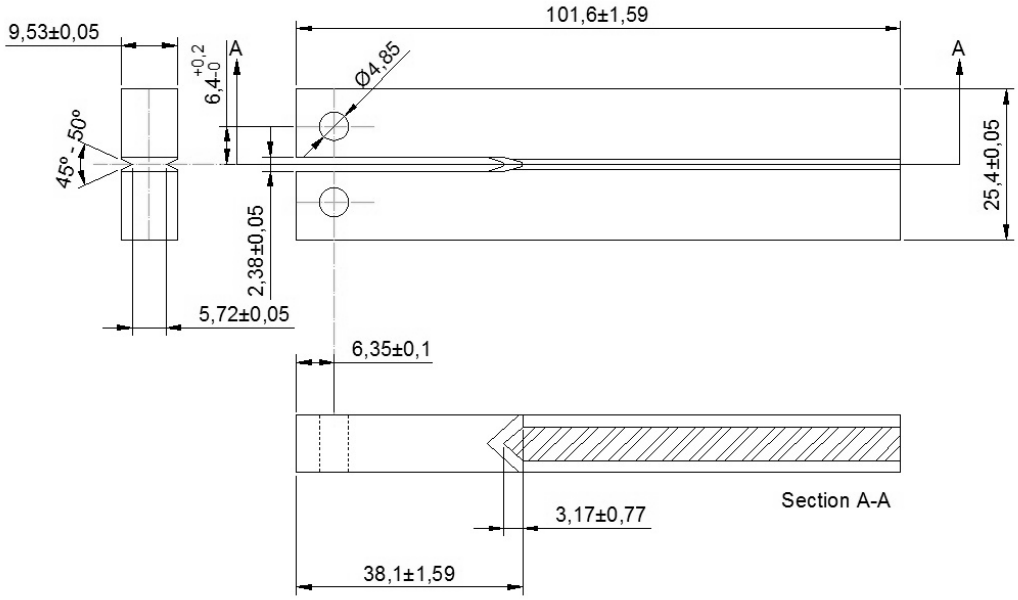

Fig 21. DCB specimens used to measure the basic 4140 resistance to crack propagation under EAC conditions inside the aggressive solution, K_{IEAC} (dimensions in mm).

Fig 22. DCB specimen loaded by an imposed displacement in a servo electromechanical testing machine at equilibrium wedge-load (left) before it was immersed in the aggressive solution; and its fracture surface after it was broken in liquid Nitrogen (right).

4.2.1.2. Results and discussion

Following the test methodology proposed, the material's resistance to initiate a crack in the AISI 4140 steel in H_2S brine solution was $S_{EAC} = 332 \pm 11.3$ MPa. The fractographic analyses of the EAC-induced failures in those smooth tensile specimens in a scanning electron microscope showed a characteristic transgranular cracking behavior, as illustrated in Fig 23. This characteristic fracture surface is commonly linked to the Hydrogen Enhanced Decohesion (HEDE) mechanism (LYNCH, 2012), however, a more accurate technique as a Transmission Electronic Microscope (TEM) is required to confirm it, identify another mechanism, or the synergistic between two or more mechanisms. The long crack propagation threshold was determined, resulting in $K_{IEAC} = 34.2$ MPa.m$^{1/2}$.

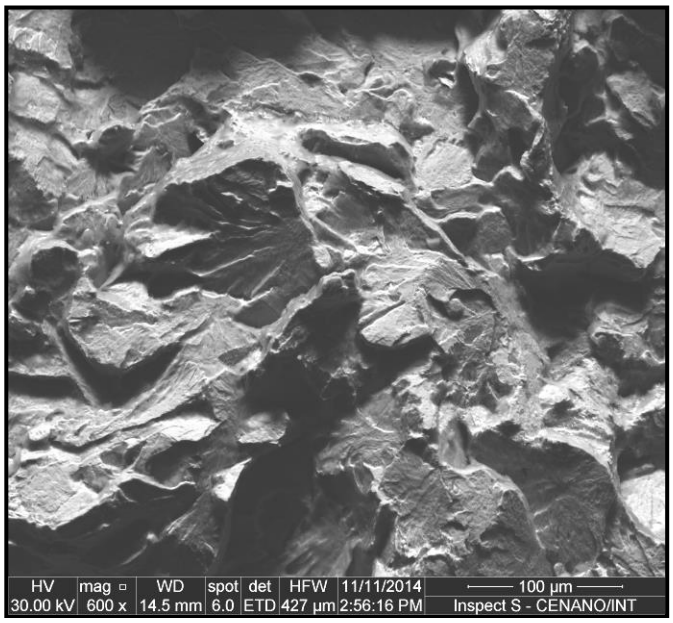

Fig 23. SEM cross section fractography of the 4140 steel tensile specimen used to measure its S_{EAC} resistance after it was loaded by the 10/10/2,4 profile.

4.2.1.3. Validating the tolerance to short crack approach for AISI 4140 steel with H_2S as a Hydrogen source.

Using the measured S_{EAC} and K_{IEAC} properties, and the tolerance to short crack approach, two notched DC(T)-like specimens were designed and machined with two different notch sizes, to reach at the notch tip a maximum stress near twice the crack initiation threshold S_{EAC}, without exceeding the material yielding strength YS to maintain LE conditions all over the tested specimens.

These notched specimen dimensions were width $w = 60\ mm$, initial notch size $b/w = 0.3$ and two different notch tip radii, one $\rho = 0.5\ mm$ and the other $\rho = 1.5\ mm$, see Fig 24. Such notched specimens were loaded in proof rings to obtain a maximum stress $\sigma_{max} = 610MPa = 1.84 \cdot S_{EAC} = 0.91 \cdot YS$ at the notch tip.

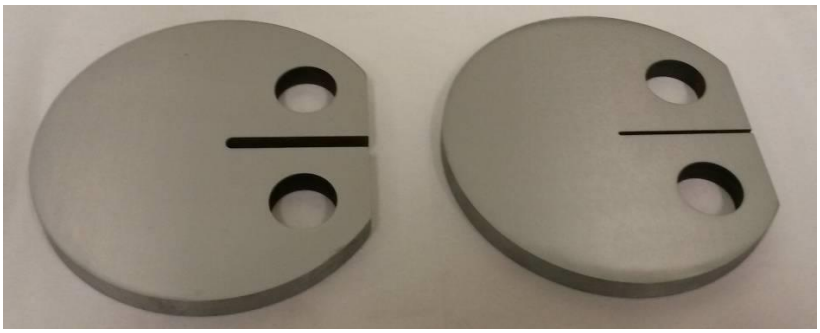

Fig 24. Notched DC(T)-like specimens of 4140 steel before their EAC tests. Note the two different tip radius.

The loads applied by the proof rings were monitored in real time using strain gages, see Fig 25.

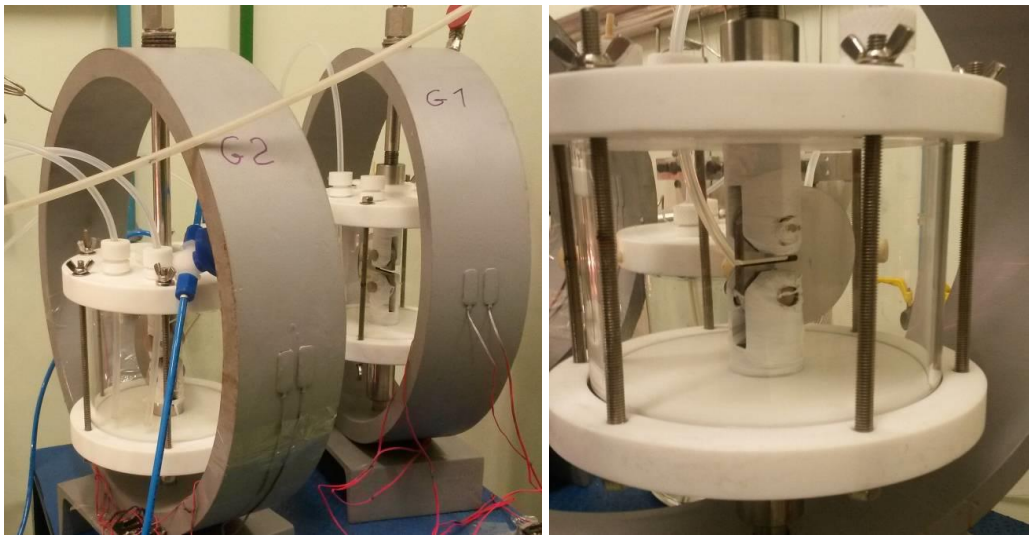

Fig 25. EAC tests of the notched 4140 steel DC(T)-like specimens used to verify the tolerance to short cracks under HE conditions predicted by the model proposed here (right), immersed in the aggressive solution and assembled in proof rings (left), and a front view of one of them.

As shown in Fig 26, exactly as predicted beforehand, these specimens did not break under such high loads after 30 days of immersion, more than twice the time needed to measure K_{IEAC}.

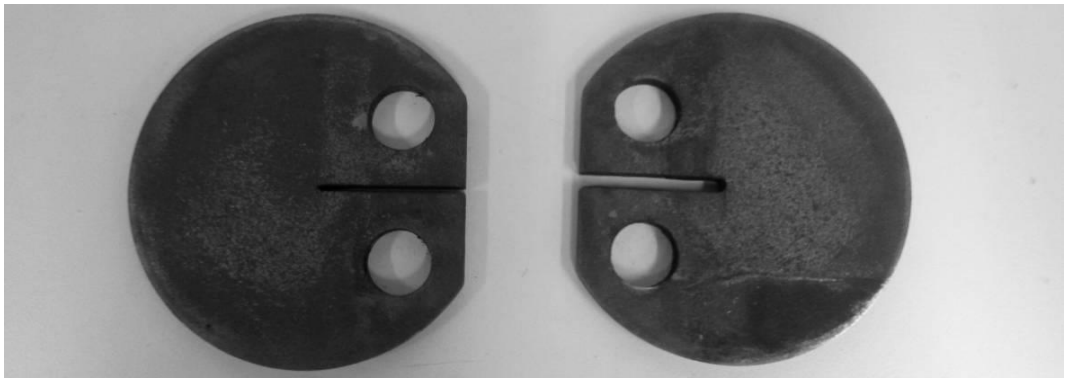

Fig 26. Notched 4140 steel DC(T)-like specimens after their SSC exposition.

Fig 27 shows the two notched DC(T)-like specimens after being exposed during 30 days to the aggressive environment that cause HE in its material.

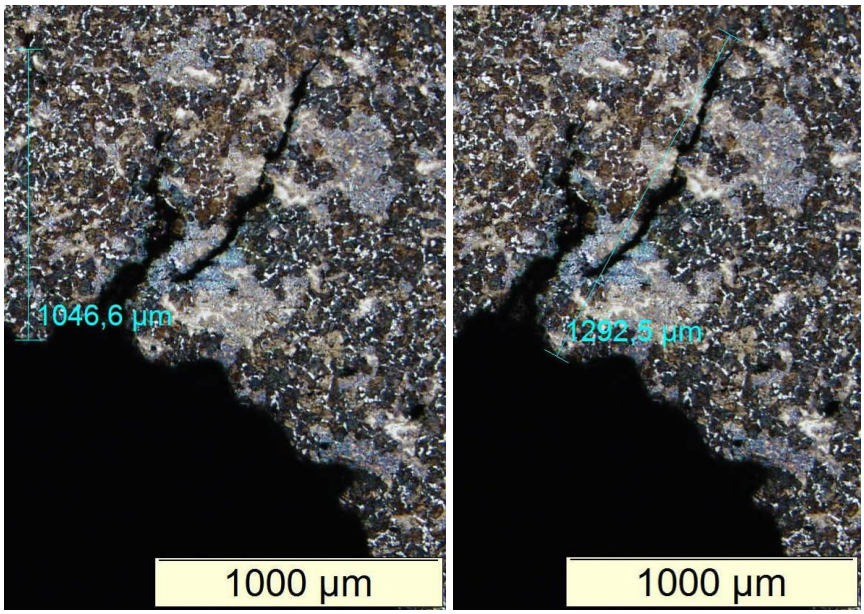

Fig 27. Tip of one of the notched DC(T)-like specimen after the corrosive exposition.

Note once again that although such 4140 steel specimens were loaded to induce a maximum stress at their notch tips $\sigma_{max} = 1.84 \cdot S_{EAC}$, a value much higher than that material resistance to start and propagate a crack by EAC in un-notched specimens, they did not break after 30 days immersed in that aggressive environment. Nevertheless, this high stress level did start non-propagating short cracks at the notch, exactly as predicted by the model proposed here, see Fig 27.

This experimental result confirms once again that this mechanical model has the potential to be useful to consider stress analysis issues when analyzing and designing structural components for EAC applications.

4.2.2. UNS 41426 Super 13Cr stainless steel under SSCC

Martensitic stainless steel is also known to be susceptible to SSCC. Although the chromium oxide layer gives a corrosion resistance characteristic for many corrosive environments, hydrogen embrittlement is a challenge for this material, and advances in material science are constantly improving the alloys and processing to withstand higher hydrogen content (LANDIM et al., 2023).

UNS S41426 S13Cr weldable supermartensitic stainless steel with good corrosion and mechanical resistances, including low-temperature toughness, are popular choices to solve some tough H_2S and/or CO_2 problems in oil and gas industry. They are now used as tubulars and casings od wheels bellow the

Christima's tree, the so-called oil country tubular goods (OCTG) application. Supermartenstic were also applied as pipelines for oil and gas transportation (above the Christima's tree).

After hot rolling, the seamless tubes are heat treated by quenching and tempering. The tempering temperature is a key parameter to their final mechanical and corrosion resistances. They can contain micro-additions of N, Ti, V, and/or Nb, to increase their mechanical strengths through carbide and carbo-nitride precipitation during heat treatments (ESCOBAR et al., 2018; LIAN et al., 2015; UDOD et al., 2016). Typically, their microstructure consists of tempered martensite with small amounts of interlath and intergranular residual austenite, as well as coarse TiN and fine Ti(C,N) and/or V(C,N) precipitates (ESCOBAR et al., 2018).

S13Cr steels are purchased in 650 or 760 MPa (95 or 110 ksi) classes, based on their specified minimum yield strength SMYS. However, they may suffer SSCC in aqueous solutions with small amounts of H_2S gas at low pH, namely H_2S partial pressure greater than 10kPa (1.5 psi) and pH < 4.5 (NACE MR0175 / ISO 15156, 2020; TAVARES et al., 2017). Other compounds in aqueous solutions may accelerate the SSC damage, such as organic acids, and chloride. In addition, pressure and temperature can affect it too.

ASTM, EFC, ISO, and NACE standards and guidelines are widely used to evaluate and qualify corrosion resistant alloys (CRA) exposed to sulfide-containing environments, among them the UNS S41426 steel (NACE MR0175 / ISO 15156, 2020). Most of them use pass/fail criteria, based on suitable specimens developing or not cracks after exposed to the aggressive environment under a specified tensile stress during a long enough testing time. Here, those standards support the way to find the S_{EAC}.

Furthermore, many design parameters for sour service are purely empirical. For example, ASME even recommends a maximum design stress of 0.67·SMYS for pipes (ASME BOILER AND PRESSURE VESSEL CODE, 2021), and (NACE MR0175 / ISO 15156, 2020) recommends SSC tests under 0.9·SMYS, using proof rings (NACE TM0177, 2016) or four-point bending tests (NACE TM0316, 2016). However, no standard or guideline nowadays considers fracture mechanics parameters to allow proper stress analyses in the design or evaluation of structural components for use in sulfide environments capable of causing SSCC.

To apply the concepts discussed in the previous sections, it is assumed here that all physicochemical effects involving SSC issues can be properly described by two material properties: the resistance to crack nucleation and growth inside the aggressive environment, S_{EAC} and K_{IEAC}, respectively. These properties must be measured after a time long enough to become time-independent, i.e. they must be compatible with the complex interaction of mechanical (tensile) stress, metallurgical characteristics of the steel, and physicochemical processes. The experimental procedures used to do that, are described next.

4.2.2.1. Materials and Methods

The basic mechanical properties of the tested UNS S41426 steel were measured by ASTM E8M procedures, resulting in E *= 209 GPa*, *YS = 826 MPa*, *UTS = 861 MPa*, and hardness *HRC 26*. This steel nominal chemical composition in weight percent, provided by its manufacturer, see in Table 8.

Table 8. Chemical composition of UNS 41426 steel.

Element	Fe	Cr	Ni	Mn	C	Si	Mo
Content (%w/w)	Bal	11.5-13.5	5.5-6.5	0.3-0.7	< 0.03	0.1-0.5	1.5-2.5
Element	Ti	V	S	P			
Content (%w/w)	0.01-0.5	< 0.5	<0.005	< 0.02			

SSC was induced in suitable specimens at 23 ± 2°C using the NACE TM177 solution C (NACE TM0177, 2016). This solution is composed of distilled water with 100g/L of NaCl, that was adjusted with hydrochloric acid HCl to obtain pH 4.0. The pressure during the tests was set to 100 kPa, with 25 kPa partial pressure of H_2S and 75kPa of CO_2. This environment is even more aggressive environment than the one used by Marchebois et al. (2007), who induced SSC failures in S13Cr steel specimens under $\sigma = 0.9 \cdot YS$ and 10 kPa (1.5 ksi) partial pressure of H_2S, as shown in Fig 28.

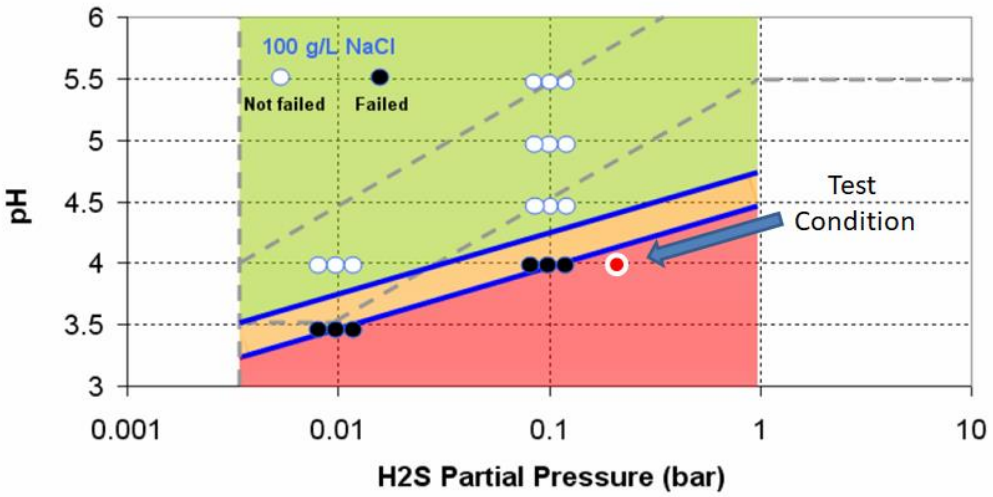

Fig 28: SSC susceptibility diagram of an S13Cr stainless steel with $YS = 854MPa$ (124 ksi) immersed in a 100g/L NaCl solution for specimens loaded under $\sigma = 0.9 \cdot YS$ (adapted from (MARCHEBOIS; LEYER; BERTINE ORLANS-JOLIET, 2007), highlighting the test condition used in this work).

Smooth tension, DCB, and modified C(T) specimens used in the following measurements were machined from an as received UNS S41426 tube with diameter 224.5mm and 13.8mm wall thickness. The aggressive solution was chosen to induce SSC, but not pitting in the test specimens.

First, acetic acid was used to adjust the solution pH, but it induced several undesirable corrosion pits in the S13Cr steel specimens in addition to the desired SSC cracks. Hence, the aggressive solution pH was adjusted with HCl instead.

A previous immersion test made following ASTM G31 and G46 procedures indicated it could avoid undesirable pitting. Indeed, all UNS 41426 specimens tested after this acid change presented a different corrosion behavior, with negligible corrosion rates and without pits, see Fig 29.

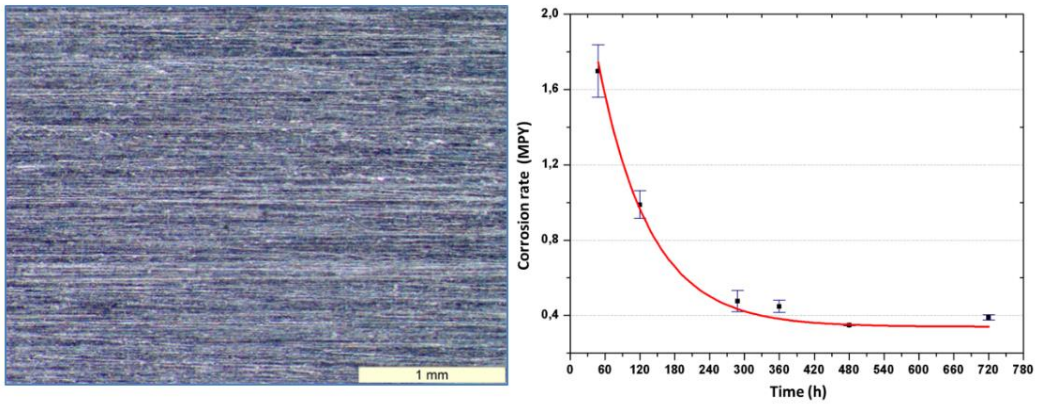

Fig 29. UNS 41426 S13Cr surface with no pits after 30 days of gravimetric test under 25.4kPa (3.7psi) ppH_2S, 75.8kPa (11.0psi) ppCO_2, pH 4.0, 25ºC, 1bar, and 100g/L NaCl (left); and its corrosion rate over time (right).

Notice that pitting is undesirable because it induces random and time-dependent stress concentration factors, which are difficult to quantify except for in a statistical way. Since the objective is to verify whether the proposed model can predict short crack tolerance from stable notches under SSC conditions, any concurrent damage mechanism should be avoided because it could mask the desired verification.

After eliminating the pitting corrosion problem from the aggressive solution, standard tests were performed to measure S_{EAC} and K_{IEAC}, the material resistances to crack initiation and growth under SSCC. These measurements provide essential chemical data for the short crack tolerance model. The crack initiation threshold S_{EAC} was determined using NACE TM0177-2016 (2016), in step-loading tests, as per ASTM F1624 (2018), see Fig 30.

The crack growth threshold K_{IEAC} was measured testing three side-grooved Double Cantilever Beam (DCB) specimens, Fig 30, following standard NACE TM0177-16(2016) method D procedures. These specimens were immersed in the anaerobic aggressive solution for 30 days, loaded by double tapered wedges that induced an initial applied $K_I = 45\ MPa\sqrt{m}$.

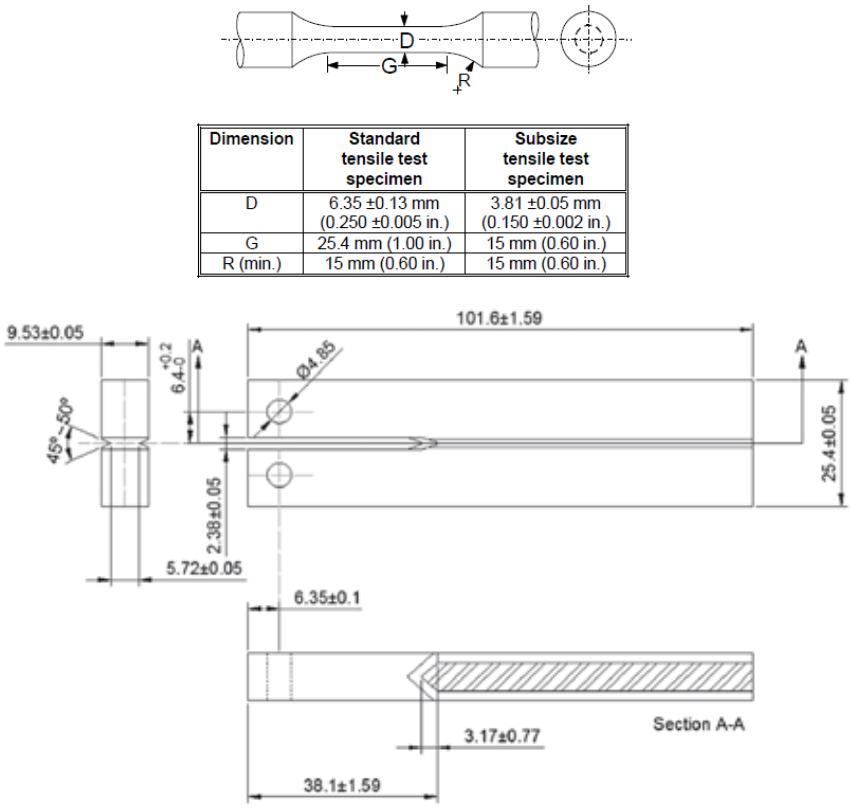

Dimension	Standard tensile test specimen	Subsize tensile test specimen
D	6.35 ±0.13 mm (0.250 ±0.005 in.)	3.81 ±0.05 mm (0.150 ±0.002 in.)
G	25.4 mm (1.00 in.)	15 mm (0.60 in.)
R (min.)	15 mm (0.60 in.)	15 mm (0.60 in.)

Fig 30. Dimensions of tensile and DCB specimens, used respectively in S_{EAC} and K_{IEAC} tests(NACE TM0177, 2016).

The tests were performed using a proof ring previously calibrated by a reference load cell, see Fig 31A and Fig 31B, and also in a servo-mechanical testing machine, see Fig 31C. The tests adopted small 10MPa load steps, initially with 12h holding time at each step, followed by 24h holding time at each step.

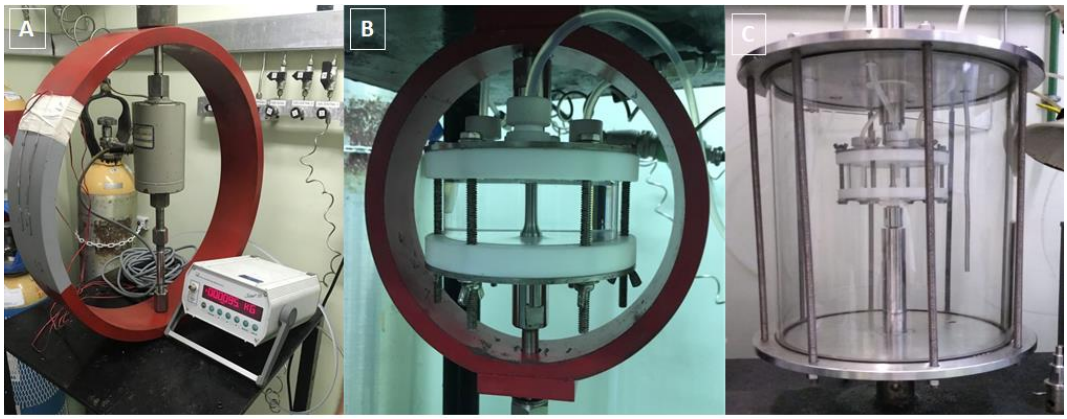

Fig 31. Step loading tests: A) Loading system used to calibrate the proof ring; B) Proof ring experimental assembly; C) Test cell assembly used for tests in a servo-mechanical machine.

The dissolved oxygen was removed by purging the solution and the test vessel for 2h per liter with 99.999% pure nitrogen gas before the specimen was immersed into the chloride aqueous solution. As the test vessel must be immune to the aggressive environment, it was manufactured using glass and PTFE. After the purge, the anaerobic solution was transferred to the test vessel, and the saturation with the test gases was performed for at least 2h. A double wall cell with constant nitrogen flow was used to ensure that the oxygen amounts remained lower than 5ppb, and the system was checked by dissolved oxygen sensors.

The K_{IEAC} measurements used the same procedures adopted in S_{EAC} experiments to avoid oxygen contamination of the solution along the tests. After 30 days, the specimens were taken from the corrosive environment and the load associated with the specimen deflection induced by the wedges was measured in a servo-mechanical machine, loading the specimens until releasing the load applied by the wedge. Finally, the specimens were broken in liquid Nitrogen to measure the SSC crack length, using a stereo microscope.

4.2.2.2. Results and Discussion

Both the material's resistance properties to initiate and to propagate cracks in the UNS 41426 in the H_2S environments were properly measured and the results were:

- $S_{EAC} = 461 \pm 23$ MPa.
- $K_{IEAC} = 36.9 \pm 0.6\ MPa\sqrt{m}$.

Fig 32 shows the K_{IEAC} specimens, while Fig 33 indicates the fracture surface of one smooth tensile specimen used in the S_{EAC} tests, with two different regions clearly identified: one (named A in the figure) corresponding to crack initiation and propagation inside the aggressive environment, and the other (named B) to the final rupture.

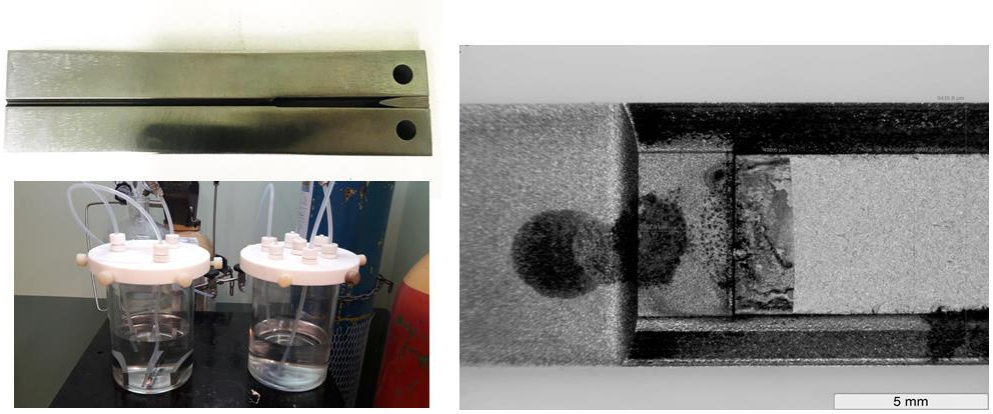

Fig 32: DCB specimen loaded by double tapered wedges during the K_{IEAC} tests, and macroscopic fracture of the DCB specimen used to measure K_{IEAC} in the aggressive environment (aqueous solution containing 25kPa ppH_2S, 75kPa ppCO_2, pH 4.0, 25ºC, 1 bar, and 100g/L NaCl).

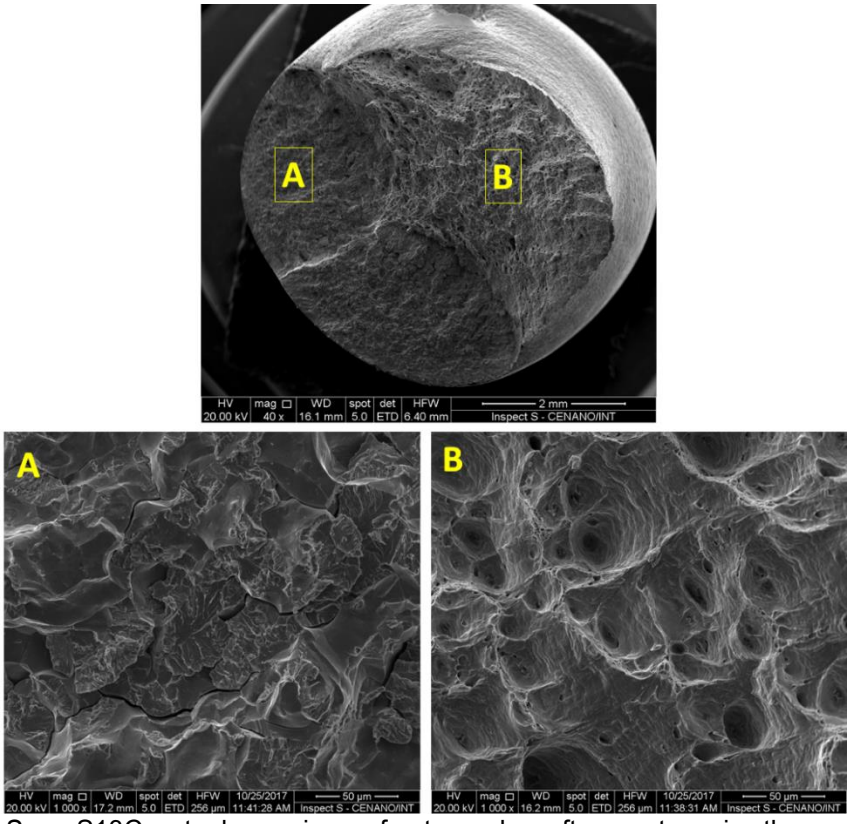

Fig 33. S_{EAC} S13Cr steel specimen fractography after rupture in the aggressive environment (aqueous solution containing 25kPa ppH_2S, 75kPa ppCO_2, pH 4.0, 25ºC, 1 bar, and 100g/L NaCl).

Fracture surfaces (A) and (B) indicate brittle fracture and plastic collapse mechanisms, respectively. At 1000x magnification, (A) presents mixed-mode, intergranular and transgranular cleavage, whereas (B) shows microvoid coalescence and dimples.

4.2.2.3. Validating the tolerance to short crack approach for UNS 41426 stainless steel with H_2S as a Hydrogen source.

To validate the current analysis, four different C(T)-like notched specimens were tested in the same environment used for the S_{EAC} and K_{IEAC} tests. The maximum stress induced at the notch tip was $\sigma_{max} = 1.70 \cdot S_{EAC} = 0.95 \cdot YS = 785\ MPa$, to keep LE conditions. These specimens' width was $w = 25\ mm$, and they had two initial notch sizes $a0/w = 0.25\ and\ 0.33$, each one with two different notch tip radii, $\rho = 0.2$ and $\rho = 0.5\ mm$, see Fig 34.

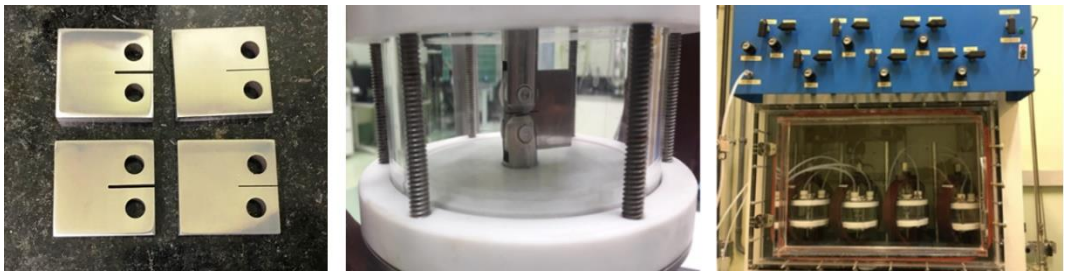

Fig 34: Notched UNS S41426 C(T)-like specimens, with four different combinations of tip radii and notch size (left). To verify the short crack tolerance under SSC predicted by the model proposed here, the specimens were first mounted inside the solution chamber (center), and then immersed into the aggressive solution loaded by proof rings, with the whole set assembled into an inert chamber, to avoid contamination during the month-long test (right).

The specimens were loaded by properly calibrated proof rings, after being assembled within an inert chamber, to avoid contamination of the environment with Oxygen. Moreover, these specimens were electrically insulated from the grips, to avoid galvanic corrosion.

The test period was defined considering the kinetics of the incubation time observed during the S_{EAC} tests, where all specimens lasted no longer than 15 days under tensile stresses higher than S_{EAC}. Therefore, to characterize non-propagating cracks clearly, the notched specimens were tested during 30 days inside the aggressive solution, following standard NACE TM0177(2016) method D procedures for stainless steels. The estimate for the SIF of short cracks that depart

from notch tips previously presented in Section 4.1 and 4.2.1 were improved for this condition, an important task in practical applications, for two reasons. First, short crack behavior is very much affected by the stress gradient ahead of the notch tip, hence imprecise estimates for its interaction with the growing (small) crack can much affect the resulting SIF value. Second, precise numerical simulations for the short crack behavior are not trivial, although recent proposals for facilitating them may be helpful (MIRANDA et al., 2019).

4.2.2.3.1. Improvement of short crack tolerance model by Finite Element Method (FEM)

Besides the Inglis-based estimate for SIFs of short cracks that depart from notch tips, the Creager and Paris (CREAGER, 1967) (C&P) estimate for stress concentration factors, based on SIFs of (long) cracks geometrically similar to the notch in question, can be used as an alternative to approximate the short crack SIFs. The idea is to use its displaced crack tip stress field as an estimate for the stress field ahead of the notch tip. Another probably better short crack SIF estimate can be obtained by using the actual stress field ahead of the notch tip, which can be easily calculated by traditional finite element methods (FEM), instead of the Inglis or C&P approximations for it.

Notice, however, that although all such methods are quite reasonable, they cannot yield precise SIF values because they do not consider stress redistribution issues ahead of the notch tip induced by the growing (short) crack. The only way to model them is by incrementally recalculating the SIF as the crack grows. This requires non-trivial FEM techniques, such as FEM with highly variable sizes (which shape needs to be adjusted properly to avoid numerical instability), sequential remeshings of the entire notch region at every calculation step, and special quarter-point rosette FEMs to simulate the crack tip singularity. All these problems are beyond the scope of this work, but they are properly studied in (MIRANDA et al., 2012).

Anyway, instead of using reasonable, but nevertheless approximate engineering estimates, FE calculations using the especially developed QUEBRA software (MIRANDA et al., 2012) were used to obtain precise values for the SIFs of the short cracks that started at the tips of the four notched specimens used in this work. Comparisons between short-crack tolerance predictions based on such

precise FEM calculations, on simpler FEM and C&P estimates for those SIFs are presented in Fig 35.

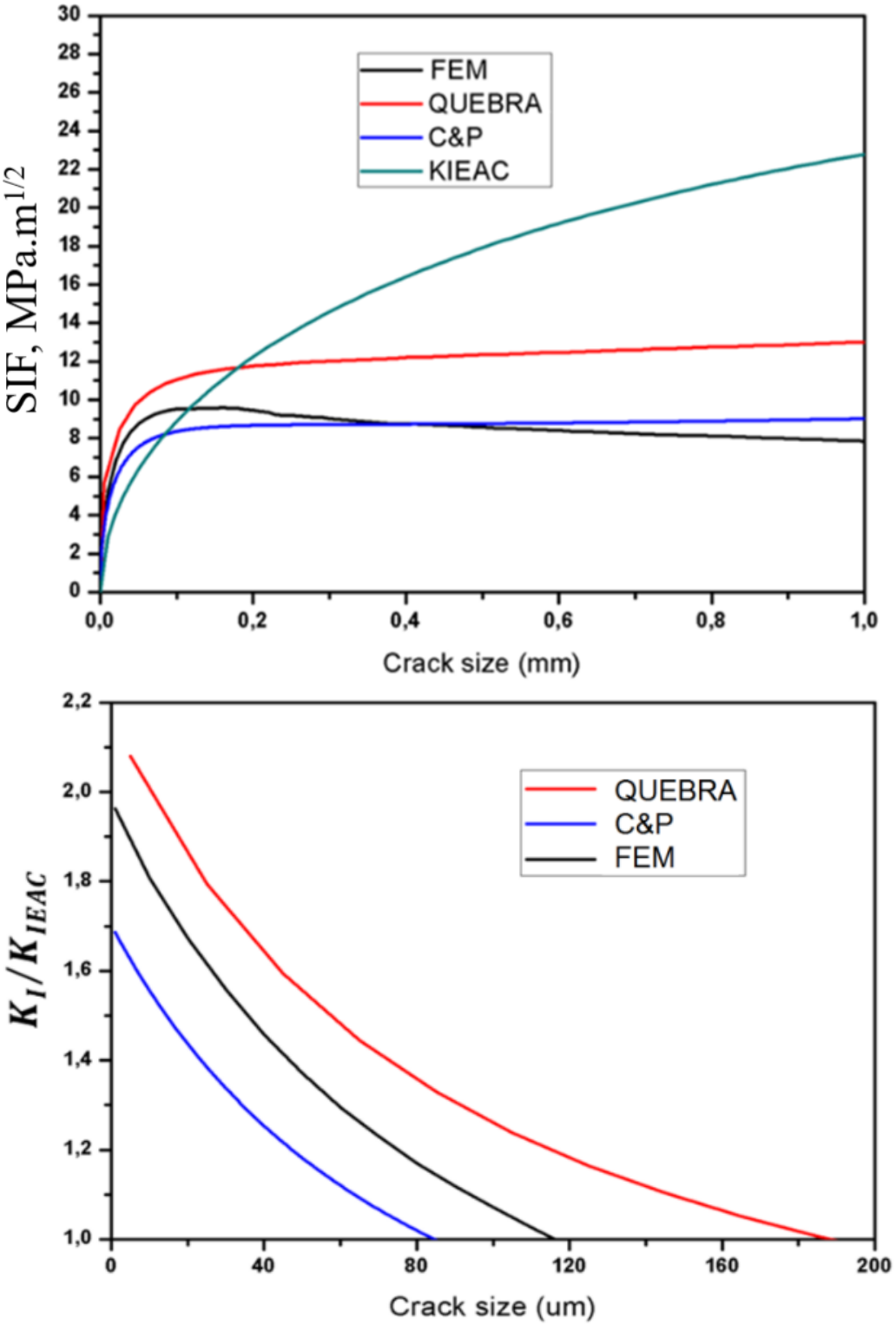

Fig 35. K_I and K_{IEAC} curves vs crack size comparing C&P, FEM stress field and QUEBRA predictions (top), and similar K_I/K_{IEAC} curves for a 0.2mm notch radius and 0.25 *a/w* relation (bottom).

This analysis indicates that, at least in the studied case (but probably in similar problems as well), the proposed estimates can provide quite reasonable ball-park figures for the short crack SIFs, if precise FEM calculations are not available for them. This way, they probably can be a useful engineering tool to evaluate if the predicted notch sensitivity by short crack tolerance can be a viable option to traditional pass/fail criteria, especially in practical SSCC and similar EAC structural integrity analyses.

Fig 35 indicates that, under its loading conditions, the crack dependent SIF curve $K_I(a)$ of the short crack that starts at the notch tip begins with a larger value than the crack size-dependent crack growth threshold-under-SSC curve $K_{IEAC}(a)$. The point at which the $K_I(a)$ curve crosses the $K_{IEAC}(a)$ threshold curve indicates where the initially propagating short crack should arrest, and the size of the resulting non-propagating crack.

The curves in Fig 35 are of course load and geometry dependent since the $K_I(a)$ curves depend on both. For higher loads than the one used in Fig 35, the $K_I(a)$ curves would move upward and eventually would not cross the $K_{IEAC}(a)$ threshold curve, indicating that the cracks initiated under SSCC in that notch tip would not become non-propagating. In such cases, these cracks would not be tolerable (LANDIM et al., 2023).

On the other hand, cracks initiated at lower loads than the one used in Fig 35 would stop at smaller lengths than the ones depicted in that figure. Notice that the crack driving force $K_I(a)$ initially grows fast because the notch-concentrated stresses near the crack tip are high, but its fast increase eventually slows down due to the notch-induced stress gradient effect at the crack tip location.

Since the sharper the notch is, the higher are its stress concentration effect and its gradient as well, sharp notches are more prone to induce non-propagating cracks, whereas such cracks should not initiate from smooth surfaces in uniform stress fields. That is why cracks initiated in S_{EAC} tests performed in smooth specimens never become non-propagating. Indeed, eventual non-propagating cracks initiated at smooth surfaces under uniform (e.g. purely tensile) applied stresses should thus indicate a significant and variable residual stress field near their starting points (LANDIM et al., 2023).

Even though the precise calculation of short-crack $K_I(a)$ SIF-values requires some numerical expertise and can be laborious, this mechanical reasoning is clear

and straightforward, thus it should not be neglected in practical applications. However, it is fair to point out that the SIF calculation for short cracks that depart from notch tips in complex geometries in general need three-dimensional modeling techniques, but this topic is outside the scope of this work.

It is important to point out as well that the mechanics used in this work assumes isotropic and homogeneous materials. Thus, strictly speaking, its predictions should only apply for cracks larger than the grain size in metallic alloys. Those details are important, but they do not invalidate the main conclusions drawn here. Indeed, like in previous EAC conditions, the simple mechanics used here (section 3.4.2 and chapter 4) was able to predict the generation of non-propagating cracks from notch tips loaded under local stresses $\sigma >> S_{EAC}$, induced by still another hydrogen embrittlement mechanism (SSCC in stainless steel) inside an aggressive environment.

4.2.2.3.1. Validation test results

As predicted, all C(T) specimens cracked at the notch tip under local stresses $\sigma > S_{EAC}$, but none of them broke under such high loads after the 30-day immersion period. It is important to emphasize that this tolerance to short cracks was predicted *before* the tests, by using the principles outlined in previous sections while properly calculating (instead of estimating) the SIFs of the short cracks expected at the notch tips, using mechanical tools described in the following.

Moreover, notice that since no non-propagating cracks were induced during the S_{EAC} tests, it is appropriate to claim that the probability of inducing such cracks by chance alone in four different notch tips with various stress concentration factors is negligible. Therefore, it can be claimed as well that these tests confirm the existence of a notch sensitivity effect in SSC, which can be quantified by proper stress analysis techniques.

Fig 36 confirms this claim. It was taken from two C(T)-like notched specimens with $\rho = 0.2mm$ tip radii after a 30-day immersion, one with $a/w = 0.25$ and the other with $a/w = 0.33$ crack-to-width ratios.

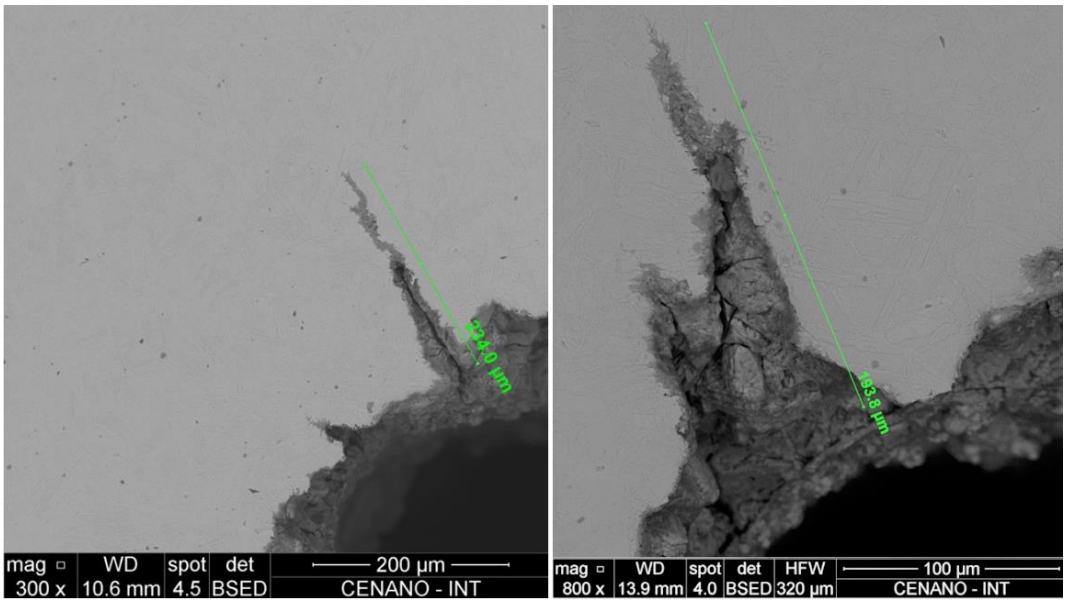

Fig 36. UNS S41426 steel specimen with $a_0/w = 0.25$ and 0.33, $\rho = 0.2mm$, after 30 days immersed in medium containing 250mbar ppH_2S, 750mbar ppCO_2, pH4.0, 25ºC, 1 bar, 100g/L NaCl.

It is important to emphasize that, even under a maximum local stress at the notch tips much higher than S_{EAC}, namely $\sigma_{max} = 1.70 \cdot S_{EAC} = 0.95 \cdot YS$, the specimens did not break after immersed for 30 days in the aggressive solution.

Moreover, notice that, due to the highly localized stress level, several small non-propagating cracks start from the notch tip, and that the largest non-propagating crack sizes are similar to those predicted in Fig 35. Since the model used to predict them has no data-fitting parameters, these experimental results clearly indicate that this mechanical model indeed is a potentially useful tool to design and analyze structural components used in SSC conditions, especially for the oil and gas industries.

Fig 37 shows the SEM analysis around the crack from the C(T)-like notched specimens with $\rho = 0.2mm$ tip radius, with $a/w = 0.25$, after 30 days of immersion.

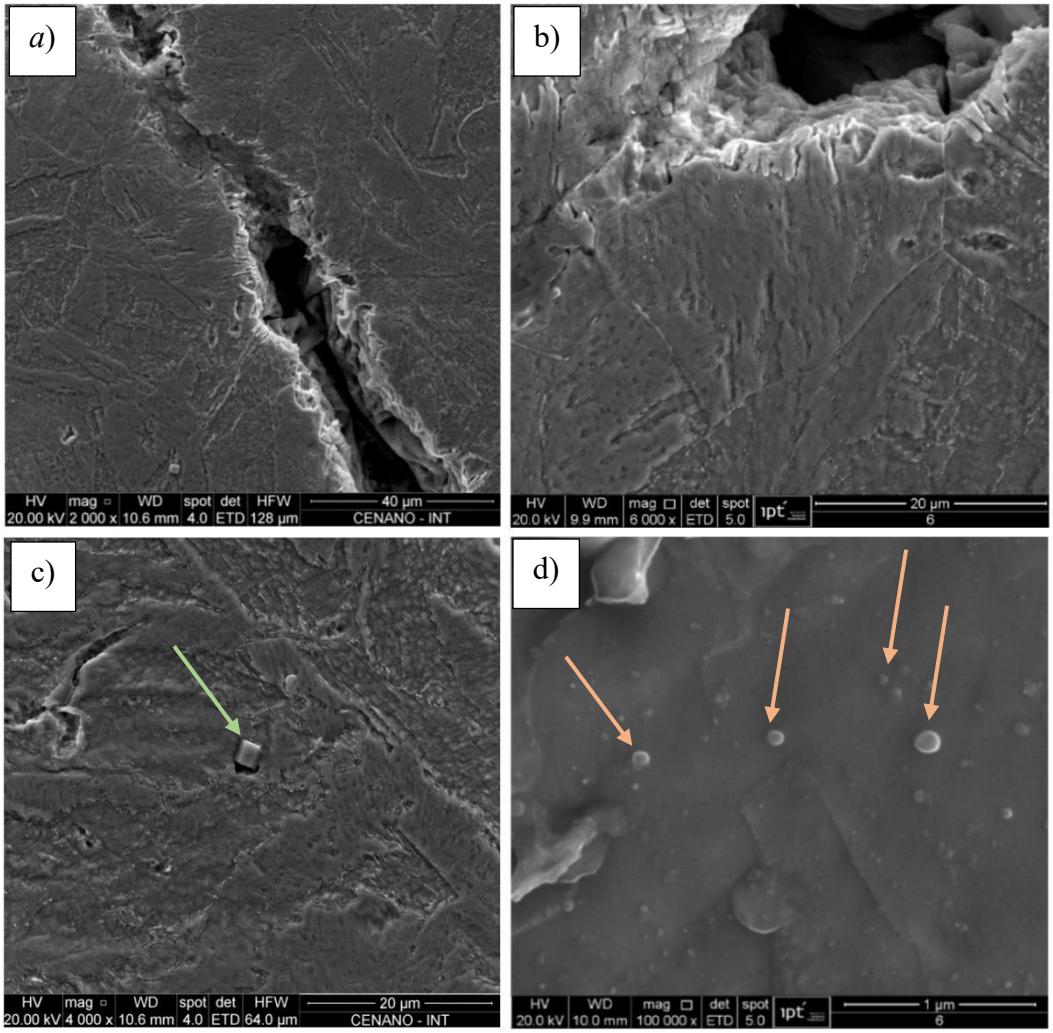

Fig 37. Region around the largest crack found on a UNS S41426 steel specimen with $a_i/w = 0.25$ and $\rho = 0.2mm$, after 30 days immersed in medium containing 250mbar ppH_2S, 750mbar ppCO_2, pH4.0, 25ºC, 1 bar, 100g/L NaCl.

The SEM analysis confirm the cracking mechanism with transgranular cracking, as Fig 33 previously indicated from S_{EAC} tests. The steel microstructure indicates the presence of some cubic precipitates of Titanium Nitride (TiN) (depicted on image Fig 33c) and other smaller and spherical precipitates of Titanium Carbides (TiC) (depicted on image Fig 33d).

4.2.2.4. Partial Conclusion

A Super martensitic stainless steel UNS 41426 was tested under HE conditions with H_2S as the hydrogen source, an aggressive sulfide environment (pH 4, 100g/L of Cl^- in water solution, 1 atm total pressure, and 25.8 kPa (3.75 psi) of H_2S with CO_2 in balance). Its resistances to crack initiation S_{EAC} and growth K_{IEAC} were measured by standard procedures.

Then, four different C(T)-like notched specimens were designed to simulate a peak stress of $0.95 \cdot YS >> S_{EAC}$ at the notch tip, to ensure that short SSC cracks would start there under nominally linear elastic conditions, but would stop after growing for a while, becoming non-propagating cracks. The experimental results confirmed the notch sensitivity under SSC predictions, just as shown before for other EAC mechanisms. These results support the claim that sound stress analysis principles should be considered as an option to over-conservative pass/fail criteria when selecting materials for EAC service.

All tests presented in this chapter demonstrate how the stress gradient ahead of notches affects the mechanical behavior of Environmentally Assisted Cracking (EAC) in short cracks, using concepts from Linear Elastic Fracture Mechanics. Indeed, the majority of real structures may experience yielding strains surrounding notch roots; hence, an elastic-plastic approach would be more appropriate to address this.

The next chapter extends recent developments on the short crack growth tolerance approach for elastic-plastic fatigue cracks to EAC, followed by proposed test methods for obtaining the main parameters needed to apply the model.

5. Elastoplastic Methodology developments to short crack tolerance approach in Hydrogen environments

Stress concentration issues under local plastic stress/strain fields around a newly initiated crack at a notch tip still are a challenging structural design problem. LEFM ideas do not apply if the plastic zone sizes are comparable to the size of the crack itself, since in such cases stress intensity factors cannot quantify the stress field surrounding the crack tip (CASTRO; MEGGIOLARO, 2016a).

Using a strain-based intensity factor (SBIF) based on linear elastic strain fields with their characteristic short crack size a_0, El Haddad et al. (1979) accounted for small scale yielding around notch tips by replacing the stress term in SIFs by a strain term. Using similar ideas, Ince and Glinka (2022) proposed an elastoplastic fatigue crack growth model that considers plasticity-induced stress redistribution around the crack tip. Other EP fatigue crack models use the J-integral as their driving forces(EL HADDAD et al., 1980). Liu et al. (2023) used the SBIF from Ince and Glinka in their fatigue short crack tolerance model to account for local plasticity around notch tips. This Chapter extends the Liu et al. model to EAC. Since the linear elastic stress intensity factor stays valid for long cracks under small scale yielding around notch tips, Liu et al (2023) considered two important issues in their model:

- Include a strain-based gradient factor ($K_{gr\varepsilon}$) in Neuber stress-strain concentration rule (NEUBER, 1961).
- Use the Ramberg-Osgood strain-hardening model to account for plasticity at notch roots.

Equation (38) replaces the stress term in equation (37) by a strain term to change the stress gradient effect factor (K_{gr}) to an elastoplastic stress gradient factor ($K_{gr\varepsilon}$) (LIU et al., 2023), assuming the stress component on the reference stress intensity factor follows Hooke's law:

$$K_I = \eta \cdot K_{gr\varepsilon}(a/w) \cdot E \cdot \varepsilon \sqrt{\pi a} \cdot f(a/w) \tag{38}$$

According to Neuber's stress-strain concentration rule, the product of $K_{t\sigma}$ and $K_{t\varepsilon}$ remains constant and equal to K_t^2, where $K_{t\sigma} = \sigma_{max}/\sigma_n$ and $K_{t\varepsilon} = \varepsilon_{max}/\varepsilon_n$. Using $\sigma_{max} = \sigma$ and $\varepsilon_{max} = \varepsilon$ to simplify the notation, then

$$K_t^{\,2} = \frac{\sigma . \varepsilon}{\sigma_n . \varepsilon_n} \tag{39}$$

Applying equation (39) to estimate K_{gr}, then:

$$K_{gr}{}^2 = \frac{K_{I\sigma}.K_{I\varepsilon}}{K_{I\sigma ref}.K_{I\varepsilon ref}} = \frac{\sigma\sqrt{\pi a}\, f(a/w).E.\varepsilon\sqrt{\pi a}\, f(a/w)}{\sigma_n\sqrt{\pi a}\, f_{ref}(a/w).E.\varepsilon_n\sqrt{\pi a}\, f_{ref}(a/w)} \quad (40)$$

Since $f(a/w)$ and $f_{ref}(a/w)$ tend to 1 when the crack size is very small, the previous equation can be rewritten in a simplified way.

$$K_{gr}{}^2 = \frac{\sigma.\varepsilon}{\sigma_n.\varepsilon_n} \quad (41)$$

Using Ramberg-Osgood relation to model EP stress/strain curves (equation (42)), local elastoplastic stress/strain around the notch root can be obtained.

$$\varepsilon_i = \frac{\sigma_i}{E} + \left(\frac{\sigma_i}{H}\right)^{\frac{1}{h}} \quad (42)$$

where ε_i is the strain for each point of the stress-strain curve, σ_i is stress related to ε_i, E is the linear elastic modulus, H and h are the monotonic strain hardening coefficients and exponents obtained on the stress-strain curves of the material.

Thus, solving the nonlinear relation on equation (43) to obtain K_{gr} from merging Neuber's rule and Ramberg-Osgood model, the local elastoplastic stress-stains is determined (LIU et al., 2023).

$$\left[K_{gr}(a/w)\right]^2\left(\frac{\sigma_n{}^2 + 2E\sigma_n{}^{(h+1)/h}}{(2H)^{1/h}}\right) = \frac{[\sigma(a/w]^2 + 2E[\sigma(a/w)]^{(h+1)/h}}{(2H)^{1/h}} \quad (43)$$

Thus, the tolerance to short crack can be extended to account for small scale yielding at notch roots, including the EP behavior into the stress or strain gradient factor. However, to extend the short crack tolerance concept to small scale yielding, the crack propagation threshold in elastoplastic conditions also need to be measured under suitable test methods (LIU et al., 2023).

5.1. Development of a new elastoplastic testing methodology under high-pressure hydrogen.

To include an EP term in the short crack tolerance model for hydrogen embrittlement conditions, the required material properties should be measured through proper tests. However, some standard tests to measure material toughness in corrosive environments do not work properly in EP conditions.

Two standard test methods have been evaluated to get the material toughness of low alloy steels at high pressure gaseous hydrogen: The static test specified in clause KD-1046 of (ASME BOILER AND PRESSURE VESSEL CODE, 2021) and in (ASTM E1681, 2023), and the J-R curve specified in (ASTM E1820-23B, 2023). The material tested by the constant displacement test method KD-1046 from (ASME BOILER AND PRESSURE VESSEL CODE, 2021) was a carbon steel plate of ASTM A516 grade B used for storage tanks. For the J-R curve, an API 5L X65 piping material have been tested under the same conditions.

5.1.1. Constant displacement test method according to KD-1046 of ASME BPVC and ASTM E1681 (T-WOL specimens)

KD-1046 of ASME BPVC test method requires an arrangement suitable for constant-displacement testing of bolt-load compact specimens. The displacement is applied to the specimen containing a machined notch and a fatigue pre-crack. The displacement is applied with a bolt tightened against a flattened pin and measured with a crack-mouth opening-displacement (CMOD) gage (see Test Method E399 (2022). Reference marks on the face of the specimen on both sides of the notch may be used to verify the CMOD measurement of the applied displacement.

5.1.1.1. Materials and Methods

According to KD-1046 from (ASME BOILER AND PRESSURE VESSEL CODE, 2021), the specimen loading must be performed inside a glovebox with an inert gas to avoid oxygen, moisture, CO_2, CO, and any other contaminant. After the loading, all specimens must be exposed to the gaseous hydrogen environment for at least 1000 hours. To apply this test method, four bolt-loaded compact test specimens were machined from a 25mm thickness plate, see specimens' dimensions

in Fig 38 with accordance with the requirements specified in ASTM E1681 (2023), considering $W = 35$ mm.

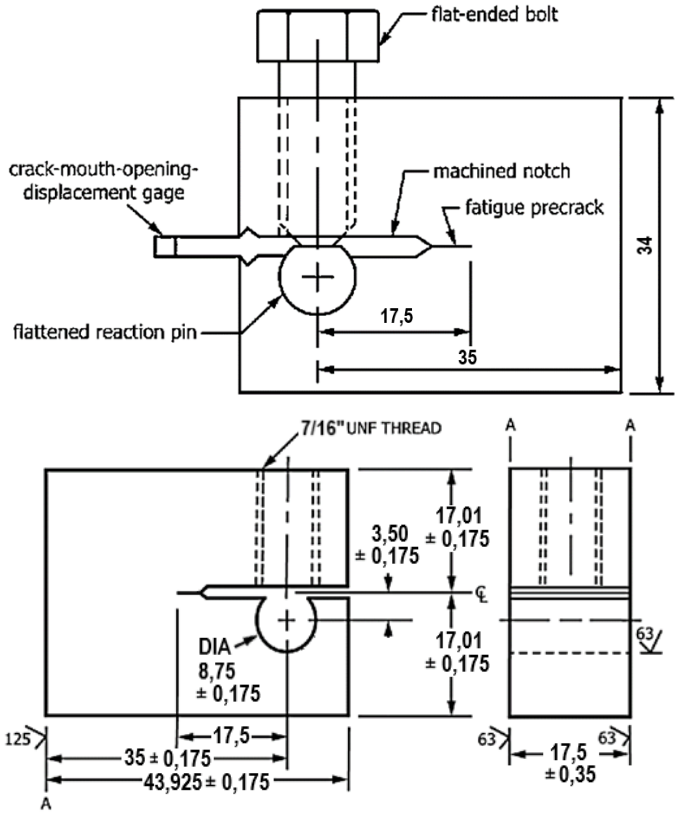

Fig 38. Schematic drawing of test assembly for constant-displacement testing of bolt-load compact specimens and its dimensions. Adapted from ASTM E1681 (2023).

Prior to the hydrogen tests, all notched specimens must have an initial sharp crack. To introduce them, fatigue tests were performed in a servo hydraulic testing machine in ambient air with an applied initial maximum $K_I = 25$ MPa$\sqrt{\text{m}}$, $R = 0.1$, and frequency 35 Hz to obtain a final fatigue crack extension $a/w = 0.5$. Fig 39 shows the testing device used in this work.

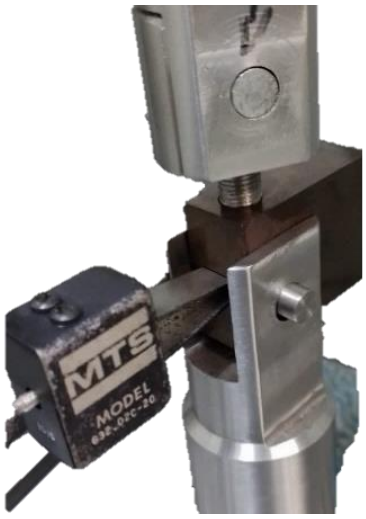

Fig 39. Test device used to pre-crack T-WOL specimens.

The final maximum SIF (K_{Imax}) was 20 MPa√m. The control mode for fatigue pre-cracking was the line load displacement measured through the clip-on gage as in Fig 39. Equation (44) defines the K_I values given by ASTM E1681 (2023).

$$K_I = \left[\frac{V_m E}{W^{0.5}}\right] f\left(\frac{a}{W}\right) \tag{44}$$

$$f\left(\frac{a}{W}\right) = \left[1 - \frac{a}{W}\right]^{0.5} \left[0.654 - 1.88\left(\frac{a}{W}\right) + 2.66\left(\frac{a}{W}\right)^2 - 1.233\left(\frac{a}{W}\right)^3\right] \tag{45}$$

where V_m is the crack-mouth opening displacement on the specimen face [m]; E is Young modulus [MPa]; a is the original or final crack size; B is the specimen thickness; and W is the specimen width [m].

The autoclave chosen for these hydrogen embrittlement test consists in a 2,2 Liter vessel made in Hastelloy C-276 with fittings, tubbing, and valves in the same material and able to work up to 35 MPa total pressure. Prior to install the glovebox around the autoclave, a leaking test was performed in the autoclave with pure Nitrogen (99,999%) up to 300bar(g) per 1 hour. After this leak test, only the autoclave lid bolts were unfastened. With all specimens, tools, clip-gage, and the autoclave inside the glove box, cycles of vacuum (20 min each one) followed by high flow (1 l/min) of pure Nitrogen (1 hour) were used to remove O_2, CO, CO_2, and moisture from the environment before loading the specimens. The complete procedure took 2 days.

An optical oxygen detector from Mettler Toledo were installed at the gas out port of the system and the specimens were loaded after the oxygen meter measured less than 1ppm of O_2. See the autoclave inside the glove box in Fig 40.

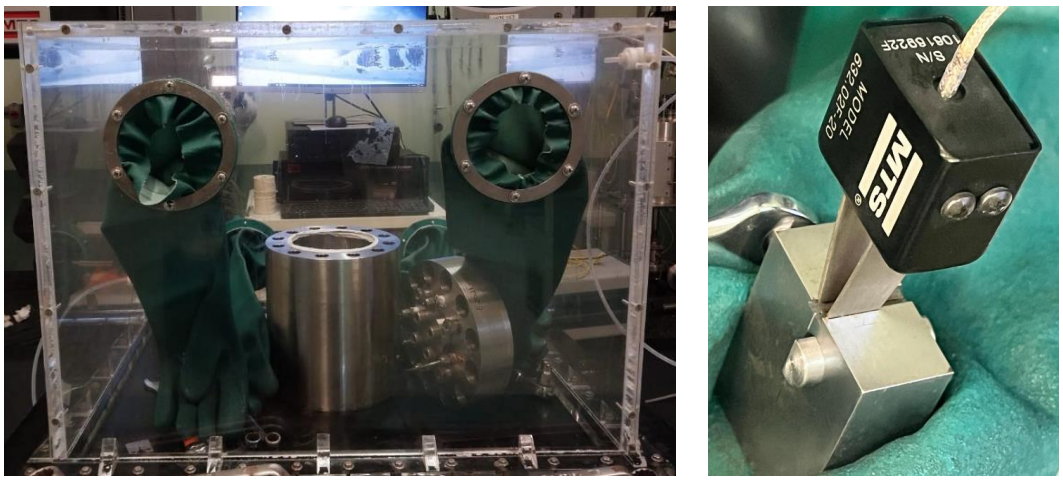

a) b)

Fig 40. a) Autoclave inside the glove box and b) test specimen been loaded.

Specimens loading was carried out with the displacement gauges to verify the applied initial CMOD values (ASTM E1681, 2023). These values were calculated using equation (44). Specimens T-WOL_1 and T-WOL_2 were loaded under K_I = 100 MPa.m^{0,5}, while specimens T-WOL_3 and T-WOL_4 were loaded under K_I = 110 MPa.m^{0,5}.

To build the glovebox, acrylic plates were glued and attached by stainless steel bolts and Nitrile rubber. Four loaded specimens were put inside the autoclave, the autoclave lid attached to the vessel within a continuous flow of Nitrogen at 2 bar(g) and 100 ml/min. At this point, the acrylic glovebox was removed and the bolts tightened up. This procedure followed by a leak test with 300 bar(g) of N_2 (99,999%) per 1 hour.

After the leak test with nitrogen, the autoclave was filled with pure hydrogen (99,9999%) at 200 bar(g) and the pressure were relief up to 1 bar(g) to remove the nitrogen from the test system. Five cycles were used to ensure that the nitrogen was purged properly. Then, the autoclave was filled with 200 bar of pure gaseous hydrogen (99,9999%) and monitored per 1000 hours.

After a 42 days long test, a gas chromatographer connected to the autoclave, measured the content of O_2, CO, CO_2, N_2, H_2O, and H_2. Prior to open the autoclave, nitrogen flushing cycles of 50 bar(g) to 1bar(g) removed the hydrogen gas from the vessel to avoid any flammable atmosphere. To obtain the CMOD values after testing, the same clip-gauge used for loading measurements was connected to the specimens during unloading. All obtained values stay in at least 90% of the loading CMOD value, a requirement to validate the test (ASTM E1681, 2023).

Heating the specimens and their fracture surfaces before broking them after they were cooled in liquid nitrogen facilitates the measurement of crack lengths and the verification of any sign of crack propagation. However, before scanning electron microscopy (SEM) analysis, the test specimens needed to be cleaned with Clark's reagent (ASTM G1-03, 2017).

5.1.1.2. Results and discussion

After ending the tests, no crack growth was observed. Hence, the methodology recommended by ASME's Boiler and Pressure Vessel Code to

measure fracture toughness in corrosive environments was not applicable for the ASTM A516 grade B tested in 200barg of gaseous hydrogen and probably will not be efficient for even more tough materials.

The mechanical behavior of cracks under hydrogen embrittlement indicates some differences for different hydrogen sources, sulfide hydrogen and gaseous hydrogen. A faster crack initiation and growth is expected for H_2S environments, which impacts significantly the total test schedule. The strain rate may play a significant role in hydrogen embrittlement as well, changing the HE mechanism in atomic scale, see Section 2.3. However, as this work aims to study the behavior of mechanically short cracks, the static tests recommended by ASME and by ASTM standards did not present the expected results when plastic strains are needed for crack growth. A modified J-integral with a rising displacement test methodology is presented on next section to obtain the elastoplastic crack propagation threshold.

5.1.2. Rising displacement test method and J-R curve, ASTM E1820.

ASTM E1820 (2023) standard procedures were used to measure J-R resistance curves and K_{IJEAC} under high-pressure gaseous hydrogen.

5.1.2.1. Materials and Methods

To find a suitable material that can withstand hydrogen embrittlement (HE) under LEFM conditions while still exhibiting susceptibility to HE under EP strains, a material meeting the requirements for operating in “sour service” conditions according to API 5L, ISO 3183, and DNV-ST-F101 may be a good choice. Indeed, these materials are certified to operate in LE conditions with electrochemical hydrogen sources, which tend to promote faster and more severe embrittlement compared to gaseous hydrogen. Despite the fact that every structural material is vulnerable to hydrogen embrittlement, and increasing materials strength reduces the resistance to HE. To measure the resistance curve and crack propagation resistance of a material, an API 5L X65QS was used. The main mechanical properties of this material are listed in Table 9.

Table 9. Main properties of the API 5L X65QS seamless pipe sample.

Pipe dimensions, mm OD x WT	YS, MPa	UTS, MPa	Charpy V-notch, J (-10ºC)
355 x 19	501	594	398

All tests were carried out in a 200 bar(g) H_2 environment, following a similar procedure to that described in 5.1.1**,** to ensure that no significant presence of O_2, CO, CO_2 and humidity was detected before and after testing using gaseous chromatography. The specimen geometry followed the guidelines presented, considering a value of *W* equal to 20 mm.

The test system assembly was developed to use cross-head displacements, measuring crack growth through line load displacement or direct current potential drop (DCPD), using load from inside or outside the autoclave, controlling hydrogen total pressure and temperature. A load cell and a clip gauge installed inside the autoclave, fittings connection with cooper-nickel wires insulated with PTFE, which conducted the signal and current for all sensors and DCPD measurements, allow to achieve reliable measurements for all measured values.

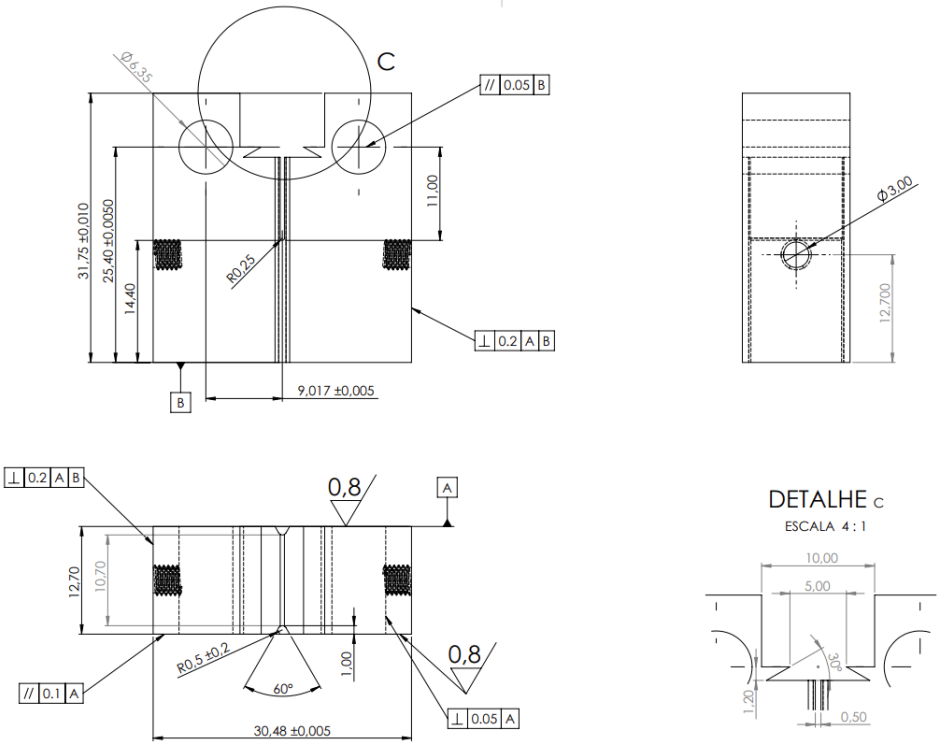

Notes: Tolerances on all dimensions ±0,013W

Pin shall be sized so that maximum clearance with hole is 0,01W.

Fig 41. Compact Tension (C(T)) test specimen geometry.

While a tailored clip-gage inserted into the autoclave measured the line load displacement, a DC power supply set to 8A and a nanovoltmeter with 0.5 μV resolution accessed the voltage drop during the tests, using DCPD terminals mounted in the test specimen, as indicated in Fig 42.

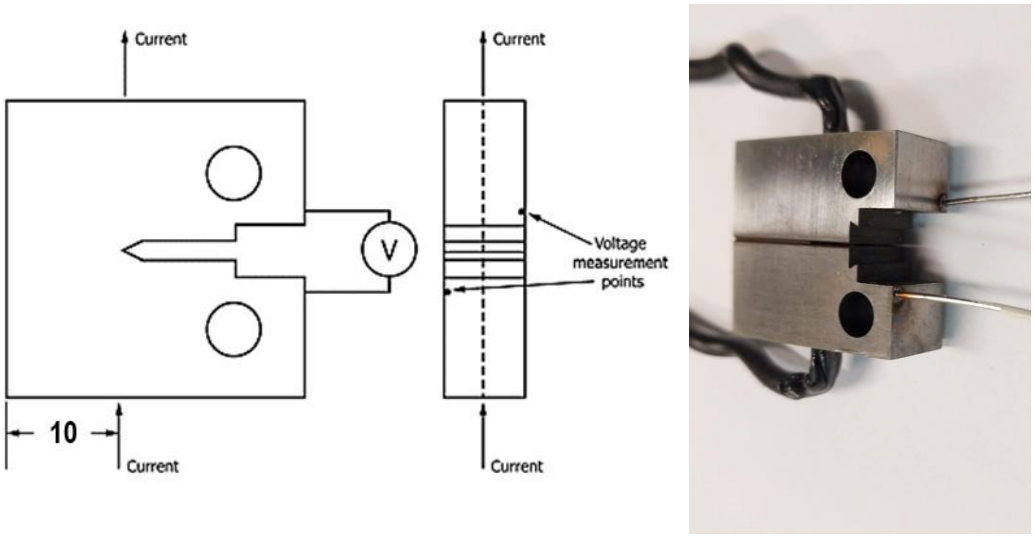

a) b)

Fig 42. a) DCPD schematic drawing adapted from ASTM E1820(2023) and b) test specimen with the wires attached.

As seen in Fig 41 and Fig 42(b), the C(T) specimens had lateral side grooves. Prior to machine these side grooves, each specimen must be pre-cracked by fatigue and both crack sides measured to estimate the initial J-values.

All fatigue pre-cracking were made in the same servo hydraulic machine following the procedure presented in Section 5.1.1. However, these tests used load control, and the *K*-values were calculated according to Equations (46) and (47), as specified by ASTM E1820 (2023)

$$K_I = \left[\frac{P_{(i)}}{(BB_N\mathrm{W})^{1/2}}\right] f\left(\frac{a_i}{W}\right) \tag{46}$$

$$f\left(\frac{a_{(i)}}{W}\right) = \frac{\left[2+\frac{a_{(i)}}{W}\right]\left[0.866+4.64\left(\frac{a_{(i)}}{W}\right)-13.32\left(\frac{a_{(i)}}{W}\right)^2+14.72\left(\frac{a_{(i)}}{W}\right)^3-5.6\left(\frac{a_{(i)}}{W}\right)^4\right]}{\left(1-\frac{a_{(i)}}{W}\right)^3} \tag{47}$$

where P is the load applied on the specimen through the pins [N]; $a_{(i)}$ is the actual crack size [m]; B is the specimen thickness [m]; B_N is the net specimen thickness [m]; and W is the specimen Width [m].

The cutting process to make all notches and side grooves were through Wire Electric Discharge (W-ED). Fig 43. shows the C(T) specimen assembling inside the autoclave with the pull rod, grips, clip-gauge, and load cell.

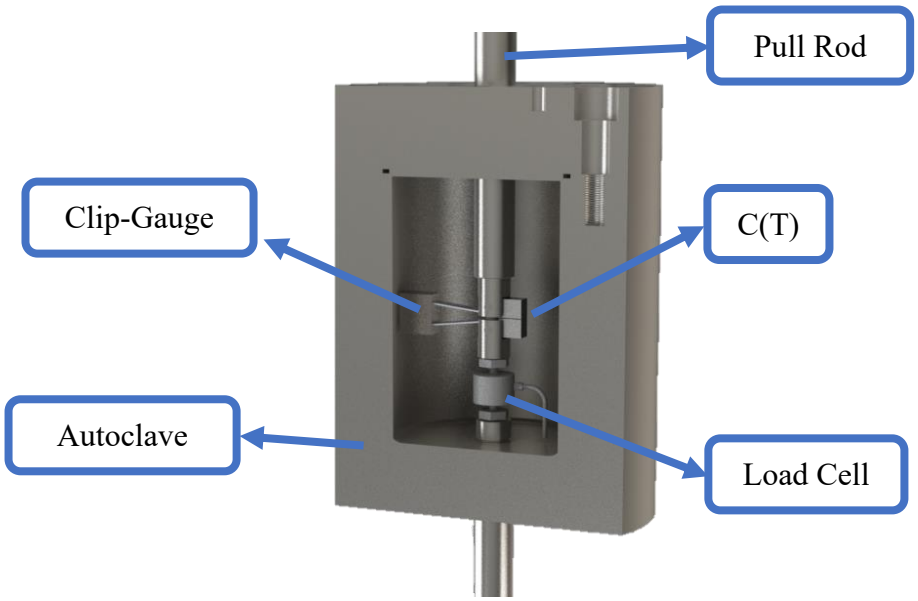

Fig 43. C(T) specimen assembly inside the autoclave. (Source: Created by the author)

To avoid the presence of even small content of contaminants and to guarantee that the environment is safe to reach the high amount of gaseous hydrogen, a leak test with pure Nitrogen (99,999%) per one hour at 220 bar and ten (10) cycles of 50 bar(g) to 1 bar(g) was used. After that, the gas composition was measured through gas chromatography with the total amount of O_2, CO, CO_2 and moisture values lower than 1 ppm. Five cycles of injecting pure gaseous hydrogen (99,9999%) for 50 bar(g) to 1 bar(g) guaranteed the nitrogen content lower than 0,01bar(g).

As the test pressure is higher than the hydrogen cylinder vessel supplied (150 bar(g)), a gas booster increased the total pressure until the test system reached the total pressure of 200bar(g) of gaseous hydrogen. Inline gas chromatographer installed at the outlet of the autoclave measured the gas contaminants.

With all system tested and safe, the DC power supply was turned on with a current of 9A, and the DCPD kept per at least 1h monitoring to guarantee good signal stability. Inside the autoclave, the pull rods are insulated from the specimen by carbon fiber reinforced PEEK washers. Fig 44 shows all test devices used to measure the resistance curve for a carbon steel in high pressure gaseous hydrogen.

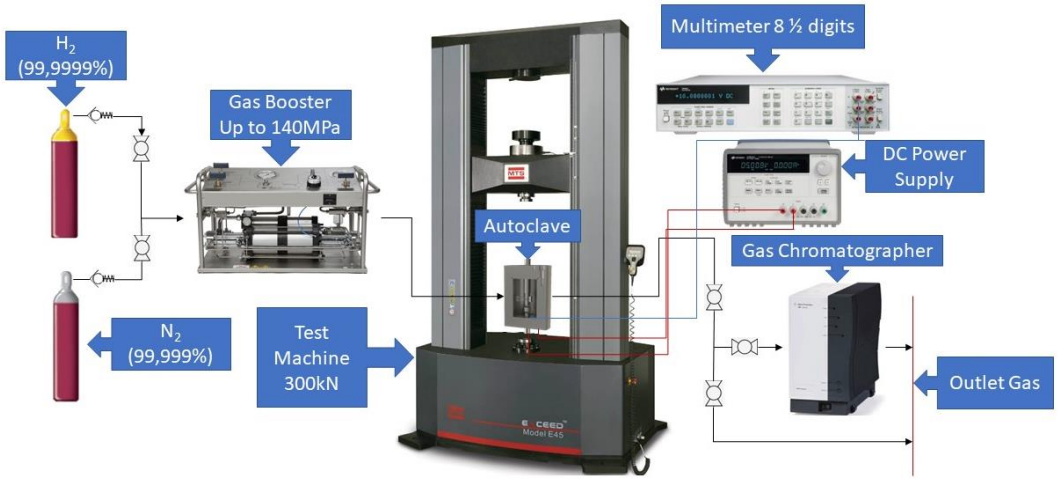

Fig 44 Schematic drawing for fracture toughness test in gaseous hydrogen at 3000Psig.

With all transducers and the DCPD system working properly, the loading procedure could start as follows:

- Constant load rate of 1.3 N/sec up to 12kN, to avoid a large interval around 10kN without loading the specimen. As the pull rod has a diameter $D_R = 25{,}4$ mm, the hydrostatic pressure (20 N/mm²) applied a compressive force $F = P_{H2} \cdot A_R = 10.13$ kN, where P_{H2} is the hydrogen hydrostatic pressure, and A_R is the cross-sectional area of the pull rod. When the specimen is tensioned above 10 kN the pull rod change from compression to tension, thus a displacement of about 0.5mm is applied without changing in force up to close all the gaps on the pins.
- Constant displacement rate of 0.01mm/sec from 12 kN up to identify more than 4mm of crack propagation, when the test is stopped.
- One test run with a higher displacement rate, 1mm/sec during the whole test.

Fig 45. Test system assembled and gas chromatographer used to guarantee the gas properties.

The post processing analysis followed ASTM E1820(2023) procedures. Resistance curve test method with crack growth measured by DCPD. J calculation for the C(T) specimen at each corresponding point a_i, v_i, P_i on the specimen force vs load line displacement record was calculate through:

$$J_{(i)} = \frac{{K_{(i)}}^2(1-v^2)}{E} + J_{pl(i)} \tag{48}$$

where $K_{(i)}$ is from equation (47), and:

$$J_{pl(i)} = \left[J_{pl(i-1)} + \left(\frac{\eta_{pl(i-1)}}{b_{(i-1)}}\right)\left(\frac{A_{pl(i)} - A_{pl(i-1)}}{B_N}\right)\right]\left[1 - \gamma_{i-1}\left(\frac{a_i - a_{(i-1)}}{b_{(i-1)}}\right)\right] \tag{49}$$

where $\eta_{pl(i-1)} = 2.0 + 0.522b_{(i-1)}/W$, $\gamma_{(i-1)} = 1.0 + 0.76b_{(i-1)}/W$, $A_{pl(i)} - A_{pl(i-1)}$ is the increment of plastic area under the force versus plastic load-line displacement between lines of constant displacement at points i−1 and i. $A_{pl(i)}$ can be calculated through equation (50).

$$A_{pl(i)} = A_{pl(i-1)} + \frac{\left(P_{(i)} + P_{(i-1)}\right)\left(v_{pl(i)} - v_{pl(i-1)}\right)}{2} \quad (50)$$

where $v_{pl(i)} = v_{(i)} - P_{(i)}CLL_{(i)}$ and $CLL_{(i)}$is defined by:

$$CLL_{(i)} = \frac{1}{EB_e}\left(\frac{W + a_i}{W - a_i}\right)^2 \left[2.1630 + 12.219\left(\frac{a_i}{W}\right) - 20.065\left(\frac{a_i}{W}\right)^2 - 0.9925\left(\frac{a_i}{W}\right)^3 + 20.609\left(\frac{a_i}{W}\right)^4 - 9.9314\left(\frac{a_i}{W}\right)^5\right] \quad (51)$$

$$\mathrm{B}_e = B - \frac{(B - B_N)^2}{B} \quad (52)$$

5.1.2.2. Results and discussion

The resistance curve of an API 5L X65 steel pipe sample in high pressure gaseous hydrogen was measured according to ASTM E1820(2023) procedures. This test involved two specimens and included the measurement and monitoring of various parameters. The recorded variables throughout the testing process were: cross head displacement, load line displacement, load inside the autoclave, load outside the autoclave, crack propagation through Direct Current Potential Drop (DCPD), temperature, hydrogen total pressure, and the levels of gases such as O_2, CO, CO_2, as well as moisture.

The results from the gas chromatography analyses revealed that the contaminant levels, including O_2, CO, CO_2, and moisture, were below 1 ppm for both tests conducted. Additionally, the concentration of nitrogen was found to be under 0.1 bar(g). During the tests, the total pressure of gaseous hydrogen applied was maintained at 200 bar(g).

Departing from the resistance curves obtained for specimens 1 and 2, the J_{IEAC} values were obtained through the intersection from 0.2mm offset line with the power law regression. The value of K_{JIC} was calculated through equation (53).

$$K_{JIEAC} = \sqrt{\frac{E}{1 - \nu^2} J_{IEAC}} \quad (53)$$

The obtained values are listed in Table 10.

Table 10. API 5L X65 Fracture toughness in 200bar(g) H_2 and in air.

Specimen	Medium	JIEAC, kJ/m²	KJIEAC, MPa√m
SpecJH2. #1	200 bar(g) H_2	50.5	107.6
SpecJH2. #2	200 bar(g) H_2	51.2	108.6
SpecJH2. #3	Air	295	257

See in Fig 46 the resistance curves obtained in accordance with ASTM E1820 (2023) for the two specimens tested in gaseous hydrogen at 200bar(g), and in Fig 47 the fracture surface of one of the specimens tested.

As noted in both figures, the fracture surface is composed of an almost plane region, consisting of the fatigue pre-crack, followed by the crack propagation region. The completely brittle region is obtained by immersing the test sample in liquid nitrogen to mark the end of the crack propagation path.

The major difference between the crack propagation region and the final fracture is the radial pattern formed during crack growth. However, as expected, the fracture surfaces for specimens tested in 20 MPa gaseous hydrogen are considered brittle with no signs of dimples and local plastic strain.

During the development of the test method to obtain the resistance curve in high-pressure gaseous hydrogen, an unexpected failure in the miniature load cell occurred. This unforeseen event becomes a study case where it was possible to obtain the load cell limits to continue using the same model in future tests, as discussed in Chapter 6.

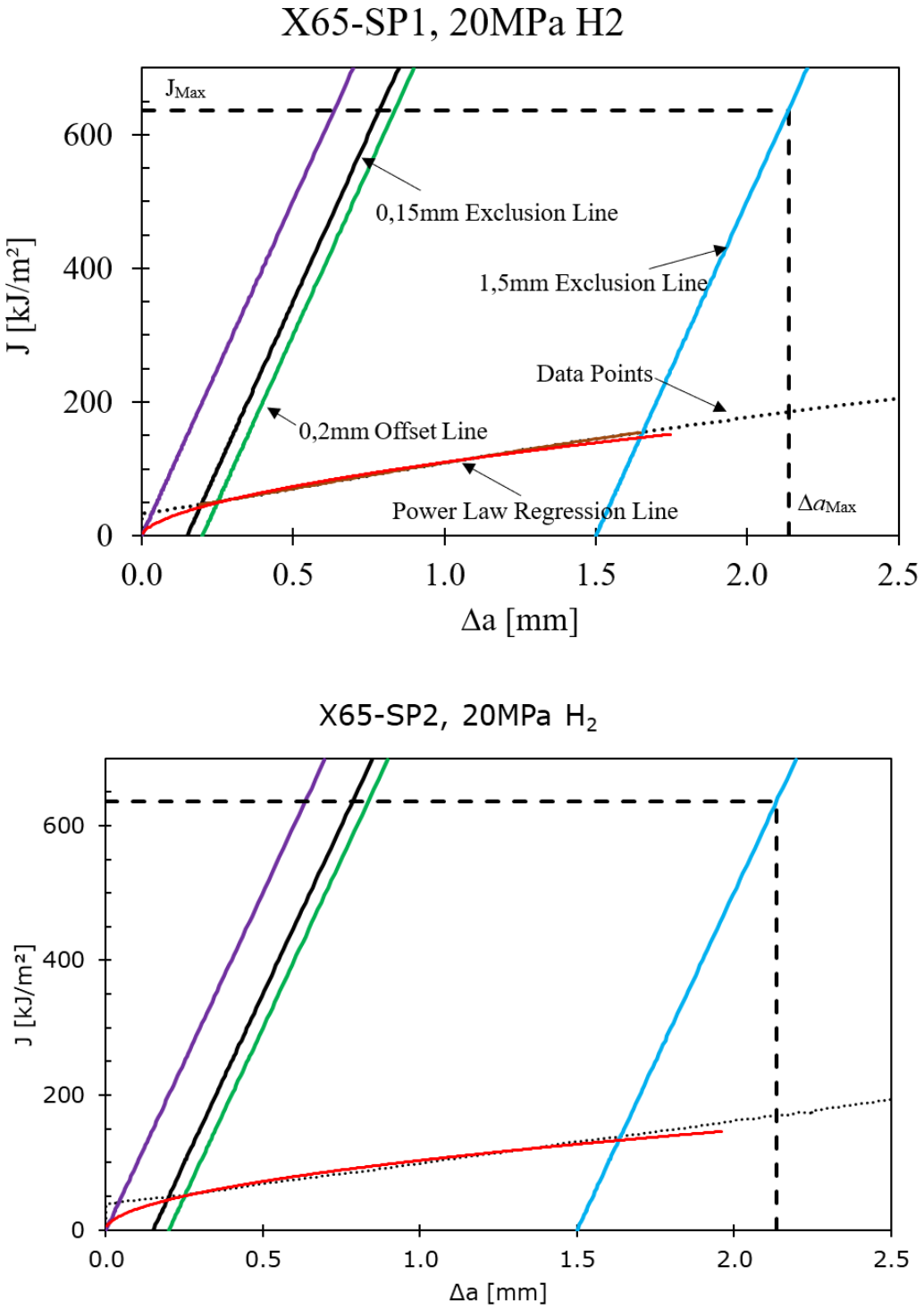

Fig 46. Resistance curves plotted as J [kJ/m²] versus crack propagation (Δa) [mm] obtained for specimens SpecJH2. #1 on top and SpecJH2. #2 on bottom, in gaseous hydrogen at 200bar(g) and 24±3ºC.

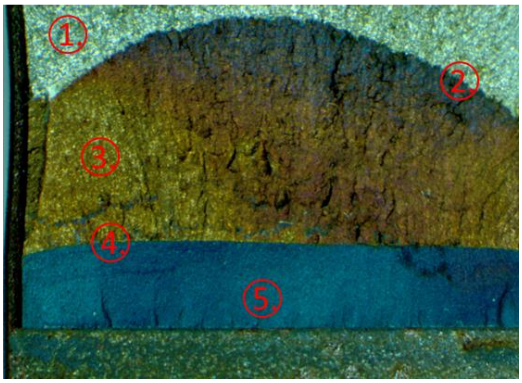

X65-SP2

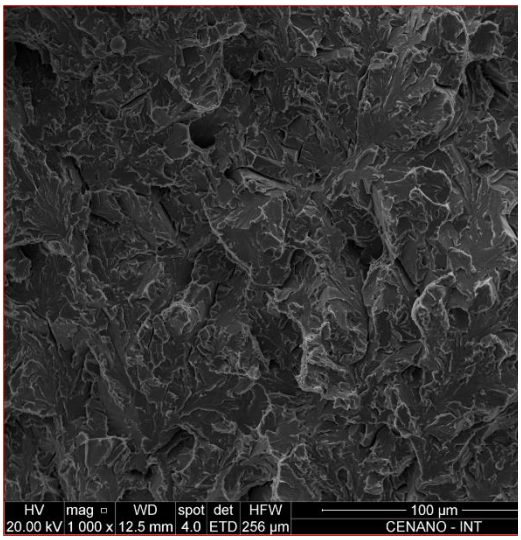

1.

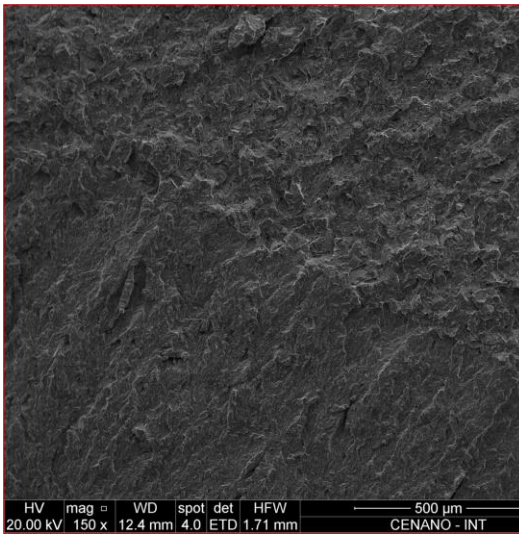

2.

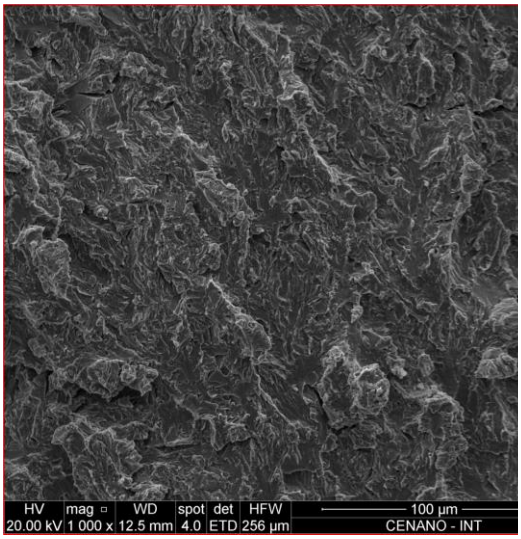

3.

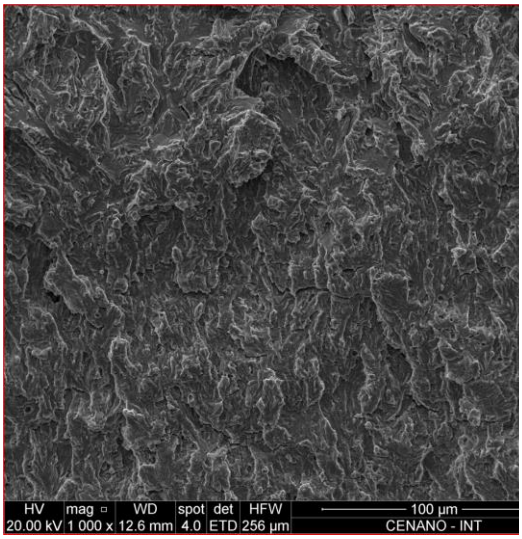

4.

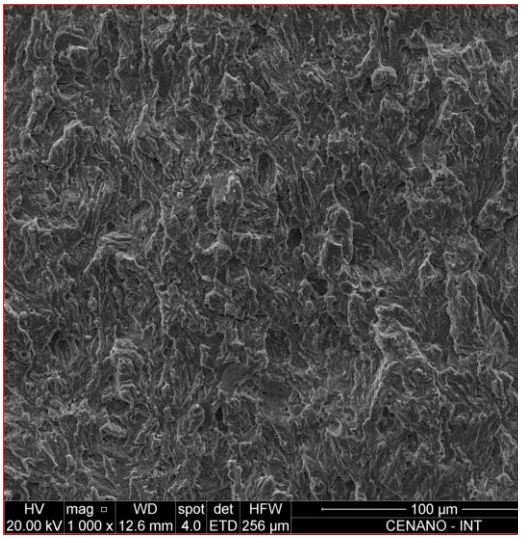

5.

Fig 47. X65-SP2 fracture surface regions

6. Failure analysis of a 17-4PH load Cell

To conduct J-R curves testing under high-pressure gaseous hydrogen conditions, it is essential that all materials and instruments used for measurement (clip-gauge, load cell, and DCPD wires), as well as those used to load the specimens, are resistant to hydrogen embrittlement and are of appropriate size to fit inside the autoclave. To meet this requirement, all components of the test system were specified in alloys, including Ni-based, Ti-based, and annealed austenitic stainless steel.

Specifically, the pull rod and autoclave are made of alloy UNS N10276, the clip-gauge is machined from an ASTM B861 grade 2 Ti alloy, and the tubing is composed of annealed 316L stainless steel.

During the material selection process for the test system, special attention was given to the internal load cell, which needed to be very small to fit within the test system. The chosen miniature load cell is a commercial one specified simply as 'Stainless Steel' (HBK U9C 20kN). Then, during the execution of ASTM E1820 (2023) test method applied to high pressure gaseous Hydrogen; the internal load cell had a brittle failure on the screw.

As, the load cell failure was not expected, a failure analysis was performed to investigate the root causes, which include tests to evaluate the chemical composition, microstructure, mechanical properties, and the fracture surface analysis in a SEM microscope.

Since the load cell indicates to not attend the material requirement to operate under high-pressure gaseous hydrogen, an alternative Fitness for Service (FFS) model (CASTRO et al., 2015; CASTRO; LANDIM; MEGGIOLARO, 2015; CASTRO; MEGGIOLARO, 2014; LANDIM et al., 2023; MEGGIOLARO; MIRANDA; CASTRO, 2007) was proposed to qualify and validate the use of similar load cells to a new maximum load. Hence, similar miniature load cells can be able to be used on the following tests to the qualification program of materials to high pressure gaseous hydrogen pipelines.

The failure case analyzed in this work occurred in a load cell used in tests to obtain the J-R curve of a low alloy steels candidates to pipelines for gaseous hydrogen transportation.

6.1. Failure analysis, Materials and Methods

The failed miniature load cell is the model U9C 20 kN from HBK with a M10 screw fixture as seen in Fig 48. The load cell failed after perform two tests according to ASTM E1820-23 (2023) at 200 bar(g) of pure gaseous hydrogen at 24 ºC, which reach the maximum load of 18 kN.

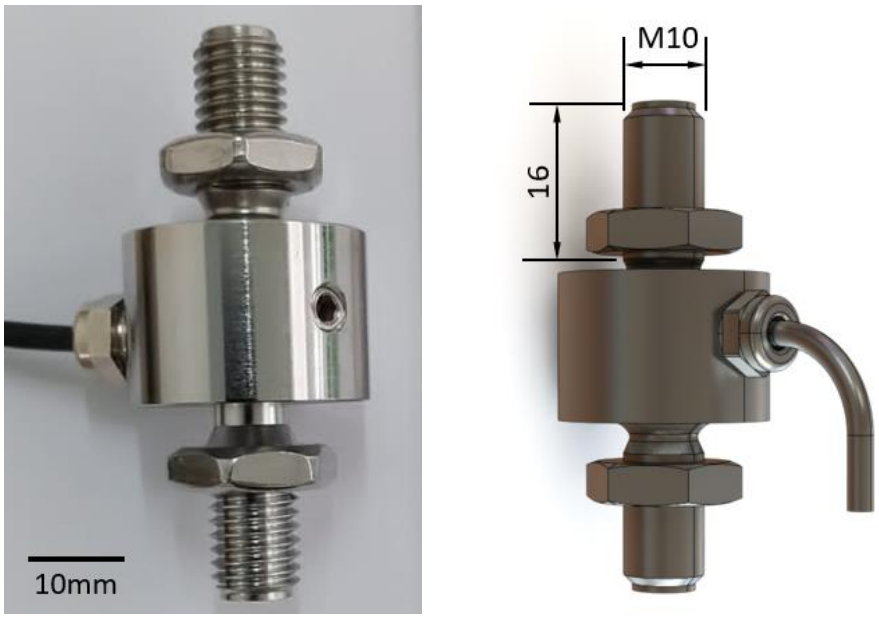

Fig 48. Miniature load cell U9C (HBK) with screw dimensions. All dimensions are in SI (mm).

The assembled test system was composed by an autoclave, pull rod, and grips in Hastelloy C-276 (UNS N10276), clip-gauge in Ti based alloy (ASTM B861 gr 2), and tubbing in annealed AISI 316L, see in Fig 49.

Crack size for all ASTM E1820-23(2023) test was measured by Direct Current Potential Drop (DCPD) with Coopper-Nickel wires, insulated to the autoclave by polytetrafluorethylene (PTFE) in AISI 316L fittings.

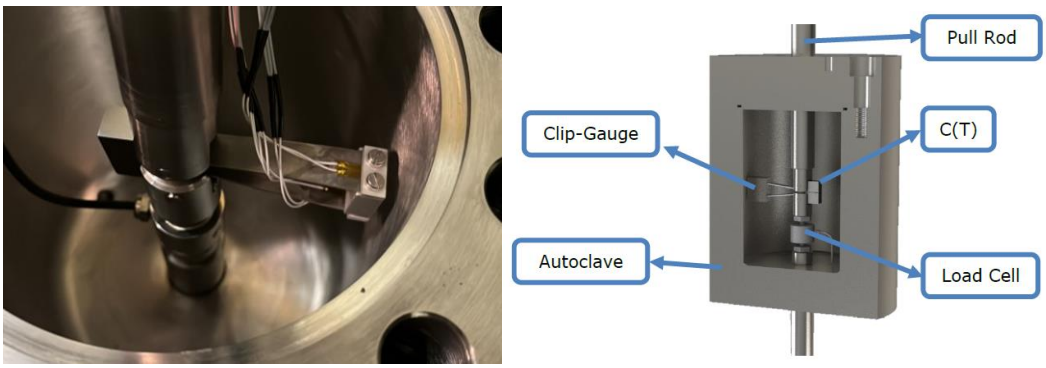

Fig 49. Assembly of a Resistance curve (J-R) test with the main components inside the autoclave and the position of the miniature load cell U9C (HBK).

As soon as the load cell came to fail, the chemical composition was obtained by X-ray fluorescence method with the PMI (Positive Material Identification) equipment model Genius 7000XRF.

To obtain the root causes that makes the miniature load cell came to fail, the fracture surface was investigated in a Scanning electron microscope QUANTA FEG 450, same equipment used to analyze the microstructure after metallographic preparation and etching with Villela's solution (95 ml ethanol, 5 ml HCl, 1 g acid picric).

On the screw side that has no cracks, it was conducted a Vickers hardness with 10 kgf load, which allows to identify the material's heat treatment condition. Based on the chemical analysis, hardness and microstructural analysis, a material with the same composition was acquired and heat treated to reach mechanical properties similar to those measured in the load cell. Specimens were machined to obtain the two main properties, S_{EAC} (Strength limit at 200bar of gaseous H_2) and K_{JIEAC} (Fracture toughness at 200bar of gaseous H_2), which are required to use the FFS model proposed for Environmentally Assisted Cracking (EAC) purposes.

The materials resistance against Hydrogen was measured through Step loading tests according to ASTM F1624-12(2018) (Strength limit, S_{EAC}) and through fracture mechanics tests according to ASTM E1820 (2023) aim to determine the Stress Intensity threshold K_{JIEAC}. All tests were performed in the same condition which the load cell failed: 24ºC, 200 bar(g) of pure gaseous Hydrogen (99,9999%).

The amounts of CO, CO_2, moisture, and O_2 were monitored and maintained to a total level lower than 1 ppm through gas chromatographer analysis before the start and immediately after the conclusion of each test. The gas chromatographer analyzer was a Micro GC Varian 490GC, see in Fig 50.

Fig 50: Gas Chromatographer analyzer model VARIAN 490 GC

Prior to inlet the gaseous hydrogen inside the vessel, all test system was purged with pure Nitrogen (99,999%) up to the total of contaminant be lower than the requirement of 1ppm. Then a leak test was performed at pressure 1.5 times the test pressure per 1hour with pure N_2. Afterwards, a few cycles of pure gaseous H_2 allows to ensure the amounts of N_2 to be lower than 1ppm.

Fig 51 (a, b) show the dimensions of the specimen and the assembly to perform the step loading test. The test procedure used to evaluate the 17-4PH strength limit under gaseous H_2 at 200 barg was according to ASTM F1624-12(2018), which consist in a step load test method commenced by a standard tensile test (ASTM E8) to determine the UTS of the material in air.

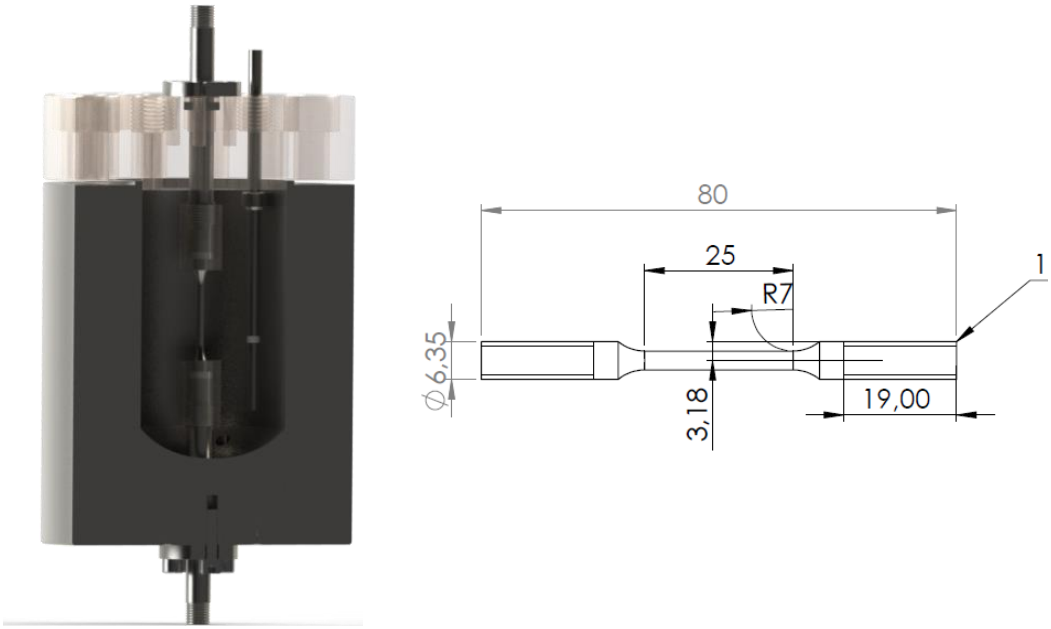

(a) (b)

Fig 51: Assembly of the ASTM F1624-12(ASTM F1624-12, 2018) test with a round specimen inside the autoclave and round specimen drawing. Dimensions are in mm.

The step loading profile to determine the threshold load was 10/5/2,4 (#/%P_{MAX}/hrs) which correspond to 10 steps with an incremental load of 5% of the Maximum load (P_{MAX}) reached at the previous test, during 2 hours each one followed by 10 steps with an incremental load of 5% P_{MAX} during 4 hours each one. P_{MAX} is set to 1.1 times the P_{th} (Load threshold) obtained in the previous test.

To obtain the stress intensity threshold of the 17-4 PH in 200 bar(g) of gaseous hydrogen the C(T) specimen was loaded at a K_{rate} = 0.2 MPa√m/minute, the load line displacement has been measured by a clip-gauge attached to the specimen inside the autoclave as previous seen in Fig 49. A similar method used to qualify the materials for pipeline wherein the load cell failure was used to obtain the KIJ_{H2} for the 17-4PH. A similar load cell was installed inside the autoclave, nonetheless the specimen has been designed to sustain a load lower than the load cell, since the specimen is already pre-cracked. The C(T) specimens (Fig 52) were pre-cracked at 30Hz with the control by ΔK using a clip gauge and the test system MTS Landmark.

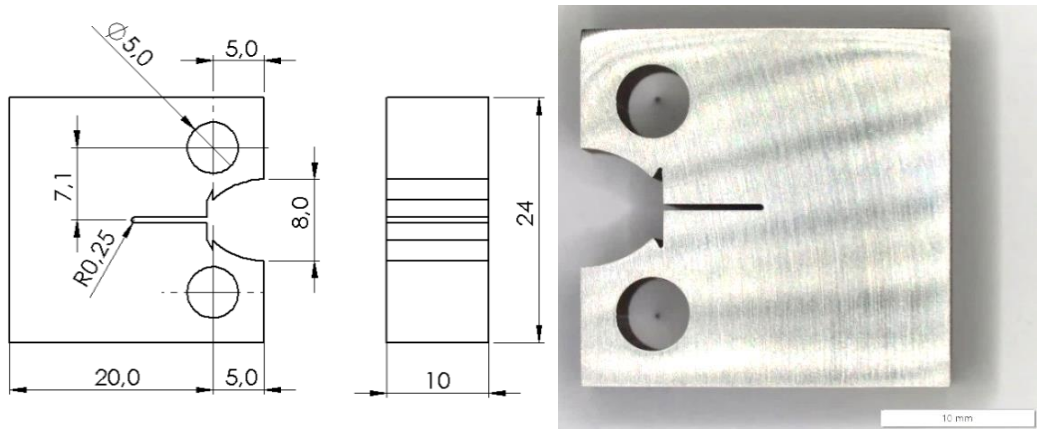

Fig 52: C(T) specimen drawing, specimen used for fracture mechanic tests according to ASTM E1820 (2023). Dimension are in mm.

Cooper-nickel wires insulated by PTFE fittings has been welded to the front of the C(T) specimen to measure the DCPD (Direct Current Potential Drop), which were connected to a multimeter outside the autoclave. A current of 8A where applied by a power supply from the bottom face to the top of the specimen as seen in Fig 53. DCPD system was applied to monitor the crack propagation along the tests.

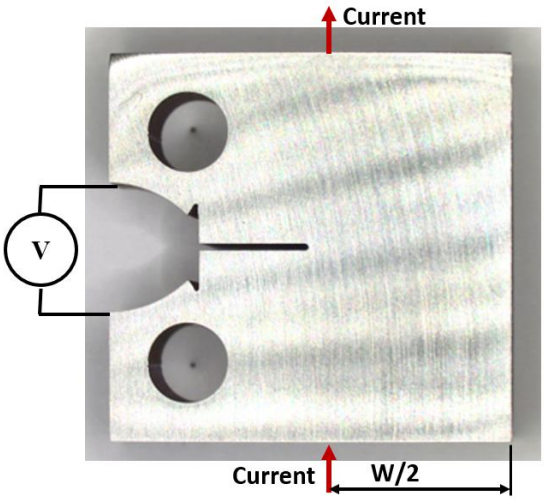

Fig 53: Schematic for the Voltage measurement points and current patch for the Direct Current Potential Drop system.

The schematic drawing indicates the assembly test method used to access both step loading tests and the Resistance Curve test.

Fig 54: Schematic drawing for step loading test and fracture toughness test in gaseous hydrogen at 3000psig.

For a comparison purpose, a SEN(B) specimen was tested in air according to ASTM E1820 (2023) to obtain the K_{IC} for the 17-4PH H900. The specimen dimension for the SEN(B) was: W=B=10.0 mm and a0 = 0.5W as seen in Fig 55.

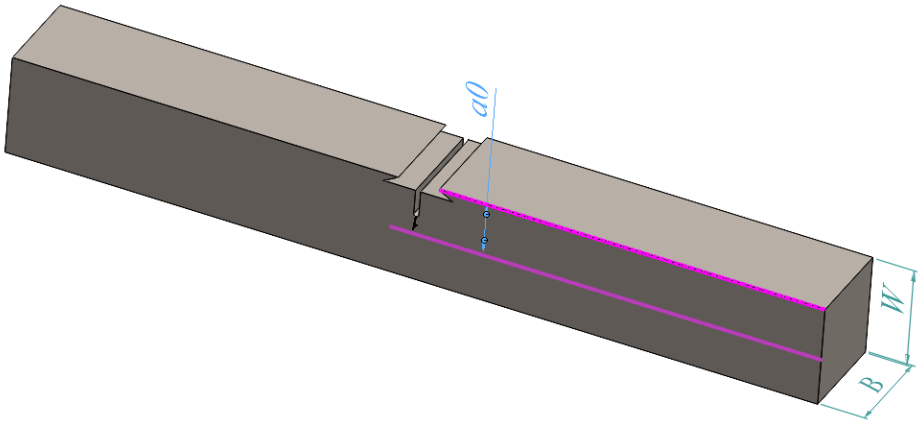

Fig 55. Schematic drawing for the SEN(B) specimen tested in air.

6.2. Notch Sensitivity approach to the Miniature Load Cell, Theory/calculation

A screw thread naturally presents a stress concentration at their roots, which can be a crack starter area if the stress becomes greater than the material resistance to the environmental assisted cracking S_{EAC}. Since the load cell has a M10 standard screw thread design, the stress concentration factor and the stress gradient ahead of the screw thread root shall be calculated to obtain the real design condition which in the material is loaded.

The stress concentration factor was obtained through the analytical model proposed by Creager and Paris (1967), equation 54, and through a numerical analysis in Abaqus software.

$$K_t = \frac{2K_I}{\sigma_N \sqrt{\pi\rho}} \tag{54}$$

where,

K_t is the stress concentration factor,

K_I is the Stress Intensity Factor,

σ_N is the Nominal Stress,

and ρ is the notch root radius

The K_I obtained from reference (CASTRO; MEGGIOLARO, 2016a), equation 55, it has been considered for the analytical model. It corresponds to the

stress intensity factor calculated for a circular shaft with a circumferential crack, under a normal load.

$$K_I = \frac{P\sqrt{\pi a s}}{2\pi(w-a)^2}\left[1 + \frac{s}{2} + \frac{3s^2}{8} - 0{,}363s^3 + 0{,}731s^4\right] \quad (55)$$

Where:

w is the shaft radius,

a is the crack depth,

P is the normal load,

and *s* = 1 - (*a*/*w*)

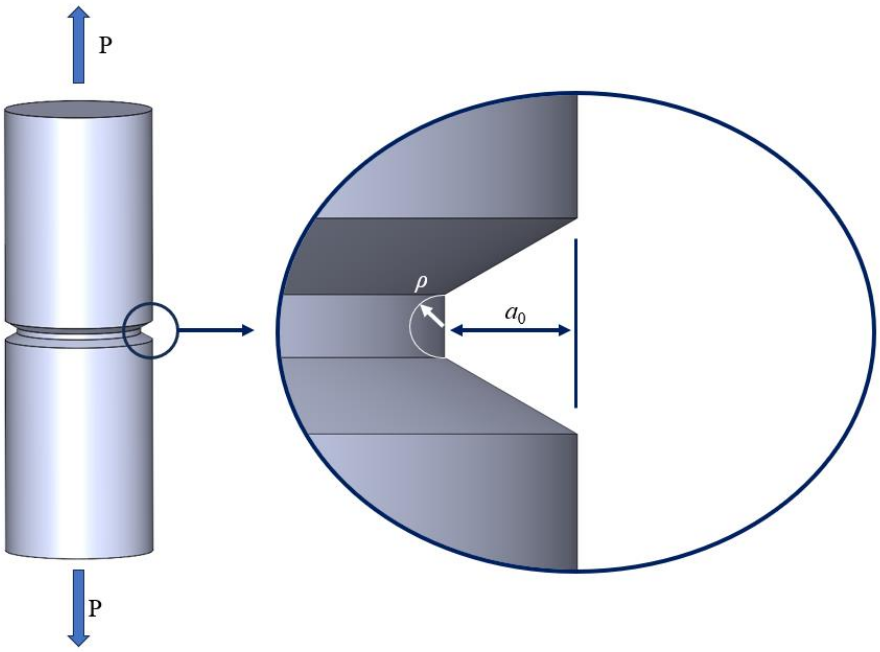

Fig 56. Circular shaft with a circumferential notch similar to the screw thread from the load cell.

Since for a screw $\sigma_n = P/A_t$, where A_t is the transversal tensile stress area from the screw and ρ can be rounded to pitch/4 (SHIGLEY; MISCHKE, 2003) as measured in the load cell in a profile projector. Then, for a M10 screw: $A_t = \pi.w^2 = 78.5$ mm², $\rho = 1.5/4 = 0.375$ mm, and $a_0 = 0.98$mm (the screw thread depth). The analytical K_t per Creager & Paris approach is:

$$K_t = \frac{2\dfrac{P\sqrt{\pi a_0 s}}{2\pi(w-a_0)^2}\left[1 + \dfrac{s}{2} + \dfrac{3s^2}{8} - 0{,}363s^3 + 0{,}731s^4\right]}{\dfrac{P}{A_t}\sqrt{\pi\rho}} = 3{,}95 \quad (56)$$

Following this tolerance defect approach to a mechanical design of structures susceptible to an Environmentally Assisted Cracking mechanism, calculate q_c requires two main properties of the material in the corrosive environment, S_{EAC} and K_{IEAC} (CASTRO; LANDIM; MEGGIOLARO, 2015), which can be measured through proper and standardized tests as cited in section 4.

6.3. Failure Analysis Results and Discussion

The chemical analysis of the failed load cell is shown in Table 11.

Table 11. Chemical composition of the miniature load cell HBK U9C 20kN compared to the specification form ASTM 564-19 (2019) material UNS S17400 type 630.

Material	%C	%Cr	%Ni	Cu	Mn	Nb	P	S	Si	Fe
HBK U9C	ND	15,3	4,64	3,01	0,34	0,23	ND	ND	ND	Bal.
ASTM 564 type 630 (UNS S17400)	0,07	15,0-17,5	3,00-5,00	3,00-5,00	1,00	0,15-0,45	0,04	0,03	1,00	Bal.

Note: ND = Not detected by PMI method.

The material composition corresponds to a 17-4PH stainless steel (UNS S17400), which is a precipitation hardenable (PH) steel that can be purchased with different properties according to the final heat treatment. Some commercial heat treatments of this material are specified in ASTM A-564 (2019).

In a macro scale, the fracture was brittle, i.e. without any sign of plastic deformation Fig 57. The fracture occurred in the screw, in a region of high stress concentration. Fig 58(a-b) show the fracture surface of the load cell, as observed in the SEM. The fracture was brittle with tear ridges, microcracks, small dimples and quasi-cleavage facets.

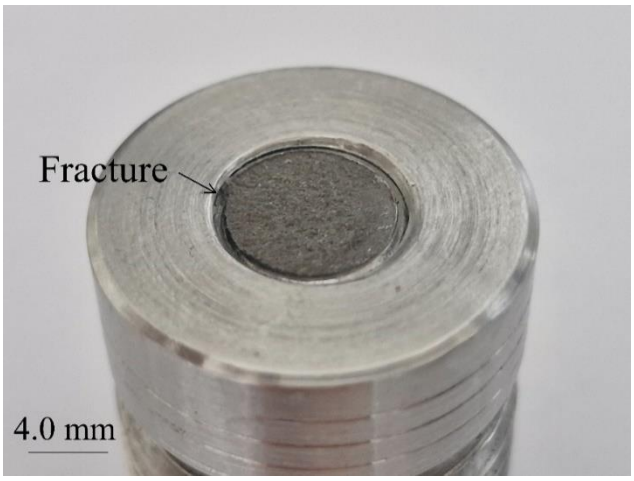

Fig 57. Macroscopic view of the fractured load cell.

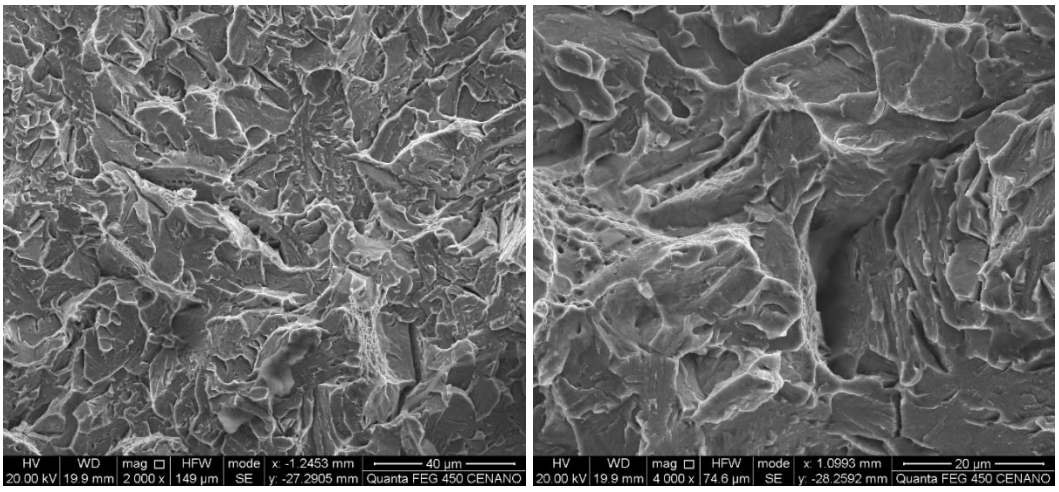

(a) (b)

Fig 58. SEM images of the fracture surface of the load cell.

The hardness of the failed material was 447±7 HV10, which corresponds to 45 HRC using the conversion table for ferritic/martensitic steels (ASTM E140-12BE1, 2012). This hardness value corresponds to condition H900, which means that the material has been solution treated (1040ºC) and aged at 480ºC (900ºF) for 1h.

The microstructure of the failed load cell is presented in Fig 59(a-b).

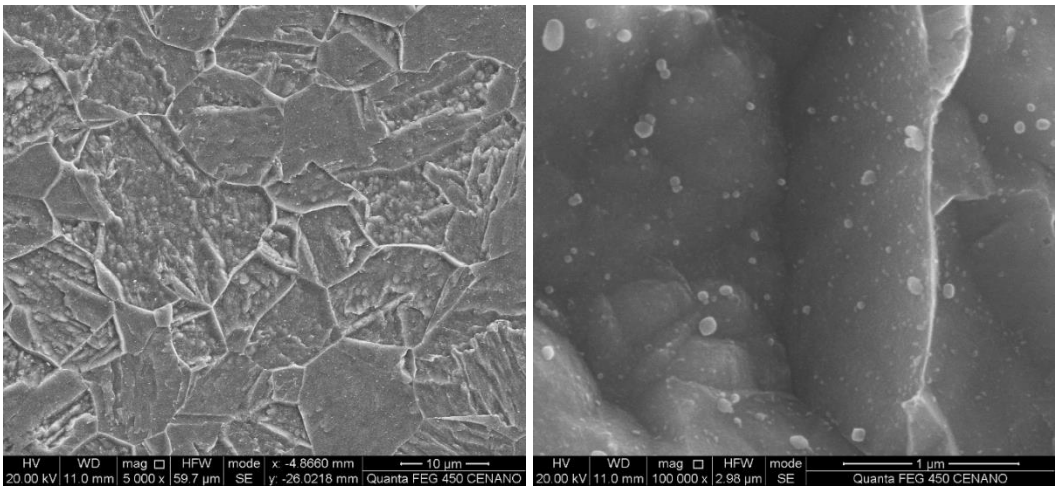

(a) (b)

Fig 59. Microstructure of the failed load cell.

Villela's reagent revealed the general martensitic microstructure and the previous austenite grain boundaries. With higher magnification, fine spherical precipitates are observed. The size of these spherical or quasi-spherical precipitates ranges from 20 to 170 nm. These precipitates are probably NbC carbides, but confirmation by energy dispersive spectroscopy (EDS) in the SEM was not possible due to the small size of the particles. Although some secondary hardening can be provoked by fine carbides, the precipitation hardening of 17-4PH is mainly provoked by fine Cu-rich precipitates (CRP), but these particles are only observed and identified by transmission electron microscopy (TEM). The precipitation in a forged and rolled bar of 17-4PH steel treated for condition H900 was investigated by Hsiao et al. (2002) with field emission gun-transmission electron microscopy (FEG-TEM). They found that the martensitic matrix still has a high dislocation density, indicating that the aging temperature was too low to provoke recrystallization. Also, the investigation revealed elliptical CRPs with nanometric sizes (15 – 25 nm) coherent with the matrix.

The UNS S17400 (ASTM A-564 type 630) is used in structural components (studs, fasteners, impellers, springs, plates …) in the chemical, petrochemical, nuclear, steel making and aerospace industries. Several cases of failure analysis of this material have been published in the last ten years (JIANG et al., 2020; LIU et al., 2019; TAVARES et al., 2009; YOUSEFI et al., 2021). Jiang et al. (2020) investigated the failure of a valve stem due to hydrogen embrittlement (HE) and found that the high hardness provoked by incorrect heat treatment lead to the high sensitivity of HE. Tavares et. al (2009) also concluded that the cause of the failure

of a pressure safety valve spring of 17-4PH was associated to its high hardness (46 HRC) compatible with H900 condition.

As specified in ASME B31.12 (2019), that material is not acceptable to handle with gaseous Hydrogen due to its high susceptibility to Hydrogen Embrittlement. It is a high strength steel that can reach a UTS higher than 1310MPa for the condition H900 (ASTM A564/564M, 2019). Prior to the age hardening heat treatment, the steel shall be solution treated at 1040 ± 15 ºC (cool as required to below 32ºC), which let the material with 38 HRC maximum. The mechanical properties after age hardening heat treatment for the ASTM A564 type 630 (UNS S17400) is as seen in Table 12.

Table 12. Mechanical Properties after age hardening heat treatment according to ASTM A564 type 630 (UNS S17400)(ASTM A564/564M, 2019) for materials up to 3in thickness.

Condition	Age hardening heat Treatment	UTS (min)	YS (min)	HRC (min)	Impact Charpy-V, min
H900	900ºF (480ºC) per 1h, Quenching in air	1,310	1,170	40	-
H925	925ºF (495ºC) per 4h, Quenching in air	1,170	1,070	38	6.8
H1025	1025ºF (550ºC) per 4h, Quenching in air	1,070	1,000	35	20
H1075	1075ºF(580ºC)	1,000	860	32	27
H1100	1100ºF(595ºC)	965	795	31	34
H1150	1150ºF(620ºC)	930	725	28	41
H1150M	1400ºF(760ºC) per 2h, air cool plus 1150ºF(620ºC) per 4h, air cool	795	520	24	75
H1150D	1150ºF(620ºC) per 4h, air cool plus 1150ºF(620ºC) per 4h, air cool	860	725	24 -33 max	41

UNS S17400 steel is a precipitation hardenable grade, a martensitic stainless steel widely used in aeronautics, minning, and oil and gas industries (TAVARES et al., 2009). The mechanical and corrosion properties depend on the final heat treatment applied. Commonly the resistance against hydrogen embrittlement decreases when the material strength increases, which might indicate that the H900 age hardening heat treatment will be the most susceptible condition to HE (TAVARES et al., 2009).

6.4. Tolerance to short crack approach to continue using the same load cell model in 200bar(g) gaseous Hydrogen.

As it was impossible to determine whether the screw would withstand minor yielding around the thread root or if a short crack would propagate even in linear elastic conditions, we used test methods that account for elastoplastic conditions to obtain the material's resistance to crack initiation and propagation. We measured fracture toughness using the ASTM E1820 (2023) protocol to obtained the resistance curve, according to section 5.1.2.

6.4.1. Step loading test results to obtain the S_{EAC} in 3000psig of gaseous Hydrogen.

As the first part of the step loading test according to ASTM F1624 is to perform a standard tensile test in air to obtain the UTS, the mechanical properties to the 17-4PH samples heat treated to condition H900 reach an UTS of 1,393MPa, YS of 1,278MPa and a ε_u of 0.094 mm/mm. Following the test procedure as previous presented in Materials and Methods section, a profile of (#10, 5, 2-4) was applied to the step loading tests. This profile entails a sequence of 10 increasing steps, each at 5% of P_{MAX} obtained from the previous test, with each step lasting 2 hours. This is followed by 10 steps at 5% of P_{MAX}, with each step lasting 4 hours.". The results are as show in Fig 60 and Table 13.

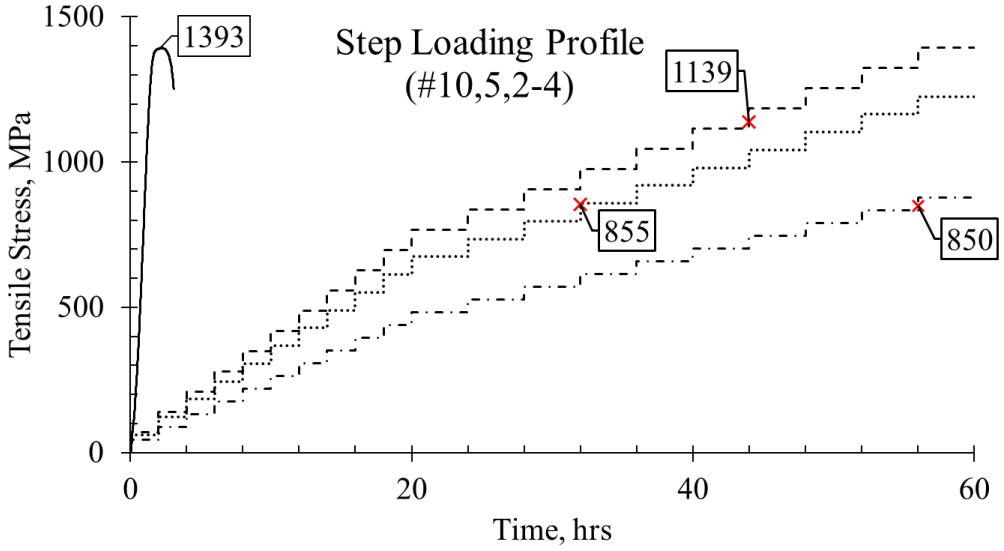

Fig 60. Step Loading Test results for a 17-4PH H900 in 3000psig of gaseous Hydrogen with Profile (#10,5,2-4).

The maximum tensile stress obtained in each test specimen is depicted in the chart of Fig. 60, where four specimens were tested.

Table 13. Mechanical properties of the 17-4PH H900 sample in air and the Step Loading Test results in 3000psig of gaseous Hydrogen with Profile (#10,5,2-4).

Specimen	UTS, MPa	YS, MPa	ε_u, mm/mm	S_f, MPa	S_{th}, MPa	S_{Max}, MPa
17-4H900_Air	1,393	1,278	0.094			
17-4H900_H2_S1	-	-	-	**1,139.3**	1,114.4	1,225.8
17-4H900_H2_S2	-	-	-	**854.7**	797.0	876.7
17-4H900_H2_S3	-	-	-	**850.1**	833.0	-

Note: $S_{MAX} = 1{,}1 \times S_{th}$

Where, S_f is the stress at the failure, S_{th} is the Stress threshold defined by the stress at the step immediately before the failure, and S_{Max} is the maximum stress to be used for the following test profile and it is defined in equation (57).

$$\begin{cases} S_{MAX} = UTS; S1\ specimen\ follow\ ASTM\ E8\ as\ baseline \\ \therefore \\ S_{MAX} = 1.1\ x\ S_{th(n-1)};\ S_{th}\ obtained\ in\ previous\ test \end{cases} \quad (57)$$

Even the specimen tested in air indicates at the surface a brittle fracture behavior, specimen border has small dimples and most of the center has a mix of small dimples and cleavage, as seen in Fig 61.

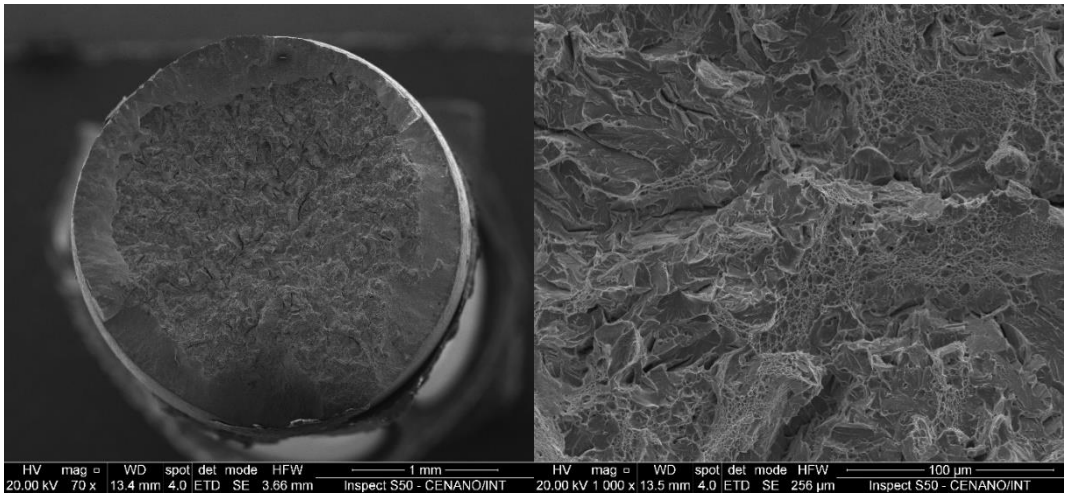

Fig 61. SEM analysis of the fracture surface of a specimen tested in air, Tensile test results.

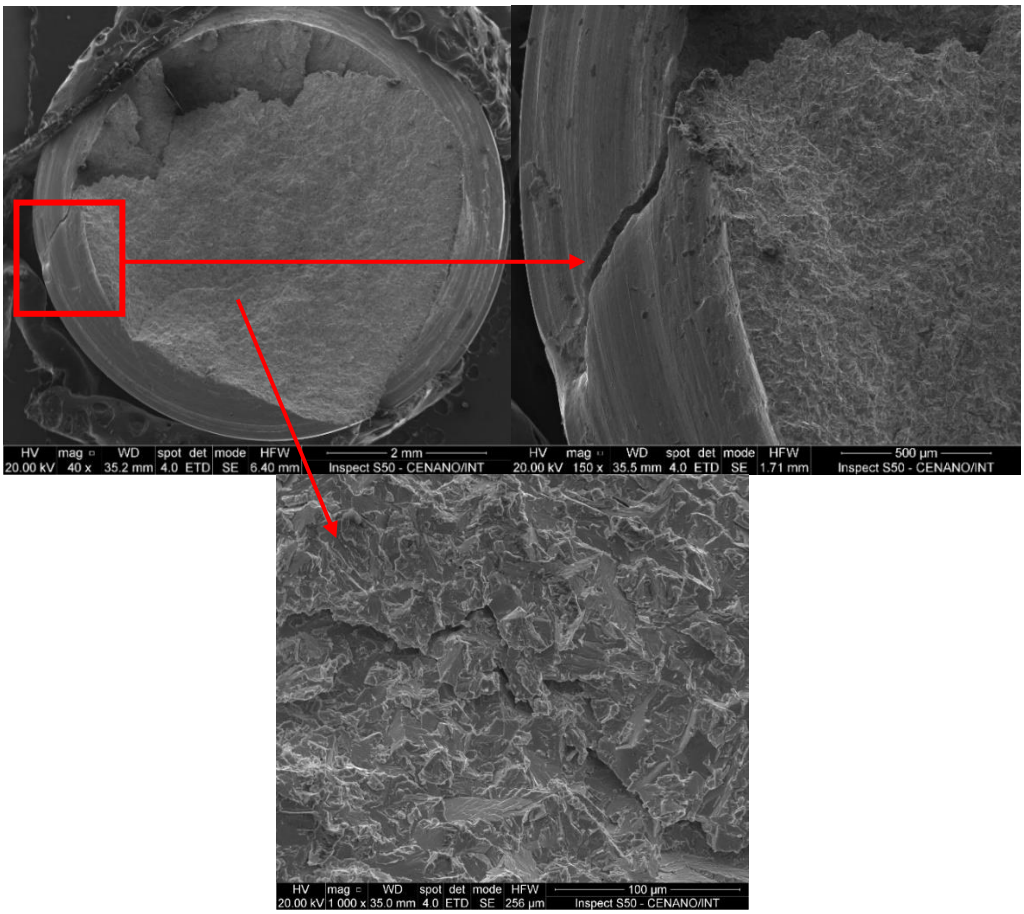

Fig 62. SEM analysis of a 17-4PH H900 specimen tested in 200barg H_2 per a Step Loading Test, specimen 17-4H900_H2_S3.

The resistance to crack start in a smooth specimen S_{EAC} is equal to S_{th} when ΔS_{th} is $\leq S_f$. Where, $\Delta S_{th} = S_{th\,(n)} - S_{th\,(n-1)}$ and is the test sequence number. According to the test results the S_{EAC} for the 17-4PH H900 sample tested in 200 bar(g) of pure gaseous Hydrogen is **833 MPa**.

While the tests in 200 bar(g) of gaseous hydrogen shown secondary cracks departing from the main fracture surface and also cleavage facets on all the fracture surface, as seen in Fig 62. Secondary cracks are a clear indicative of Environmentally Assisted Cracking.

6.4.2. Fracture Mechanic test results to obtain the K_{IEAC} in 200bar(g) of gaseous Hydrogen.

The C(T) specimen results from testing a 17-4PH H900 sample under 200 bar(g) gaseous H_2 did not exhibit any plastic behavior, and a very low K_{IEAC} was observed. A pop-in event was noted, as depicted in Fig 63.

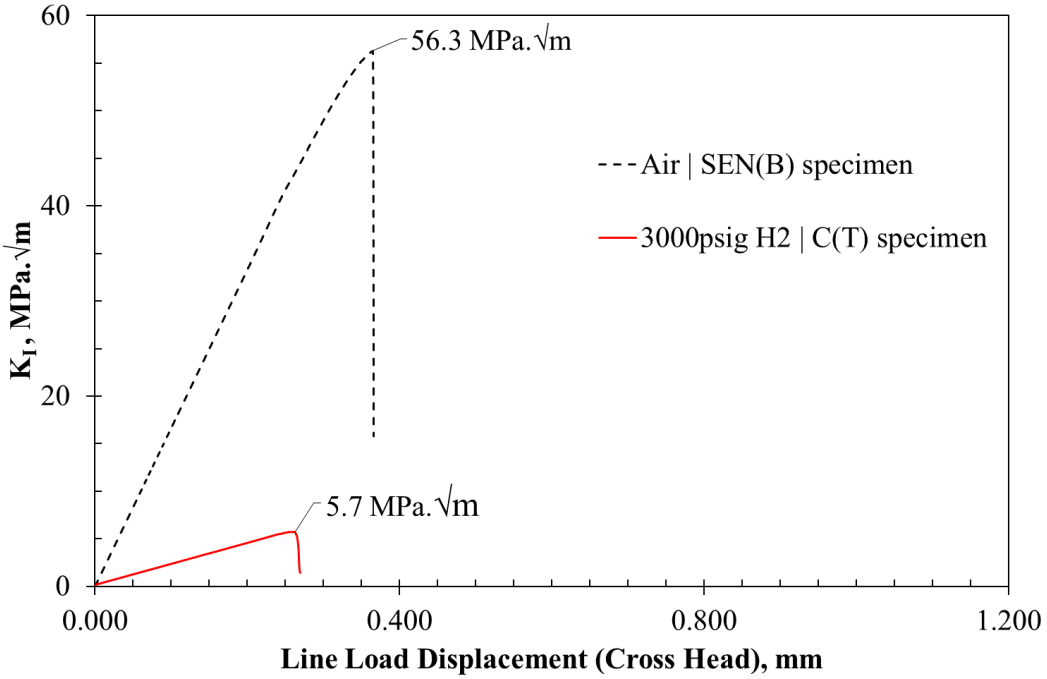

Fig 63. K_I vs LLD curve for a 17-4PH H900 C(T) specimen tested in 200bar(g) of gaseous Hydrogen compared with a specimen tested in air condition.

Given the significantly low K_{IEAC} induced by exposure to hydrogen in the 17-4PH H900, a subsequent test in air was conducted, revealing a similar pop-in occurrence. Low values for K_{IEAC} and high values for S_{EAC} will result in a small characteristic short crack size. Hence, this induces a notch sensitivity effect that approaches 1 (CASTRO; MEGGIOLARO, 2016a).

6.4.3. Notch sensitivity factor and the design of a similar load cell to operate in 200bar(g) of gaseous Hydrogen.

Solving the equations (33) and (34) for the values of S_{EAC} and K_{IEAC} at 200 bar(g) H_2 (S_{EAC} = 833 MPa, K_{IEAC} = 5.7 MPa.√m) will yield the values of K_{tc} and q_c. It is important to emphasize that K_I shall be greater than K_{Ith} for a crack propagate.

$$\begin{cases} K_{tc} = 3.88 \\ \therefore \\ q_c = \dfrac{K_{tc} - 1}{K_t - 1} = \dfrac{3.88 - 1}{3.95 - 1} = 0.96 \end{cases} \tag{58}$$

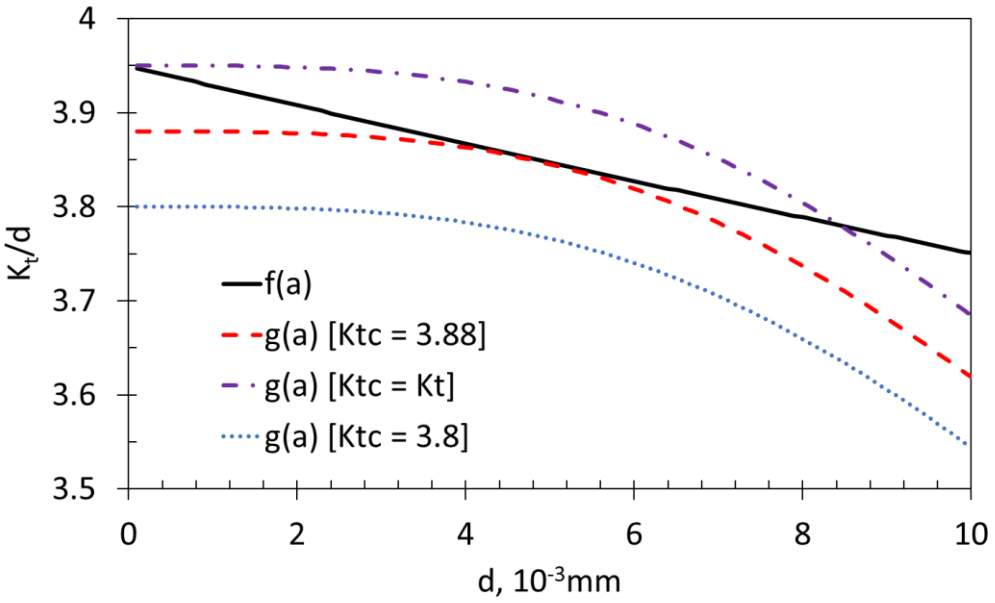

Fig 64. Comparison between the stress gradient ahead of the notch root f(a) with the threshold function g(a) for different K_{tc}, for a 17-4PH H900 in 200bar(g) of gaseous Hydrogen.

In Fig 64, the intersection between f(a) and g(a,Ktc) identify the characteristic short crack size. Where d is the distance ahead the notch root.

In environments wherein the sample has a brittle behavior, like the 17-4PH H900 in 200 bar(g) H_2, the notch sensitivity tends to 1 as K_{tc} tends to K_t. Materials that are very sensitive to the embrittle mechanism of the environment short crack sizes that are around the grain size of the material. So, the maximum load allowed to the 17-4PH miniature Load Cell in 200 bar(g) of gaseous Hydrogen is:

$$\frac{P_{MAX}}{A_t} K_{tc} = S_{EAC} \therefore P_{MAX} = 11.8\ kN \tag{59}$$

As part of the ongoing materials qualification program for operation at 200 bar(g) of gaseous hydrogen, a maximum allowable load of 10 kN was specified. This limitation imposes restrictions on the size of the specimens.

7. Conclusions

The fracture mechanics approach effectively models the behavior of non-propagating short cracks across various Environmentally Assisted Cracking conditions. This includes Liquid Metal Induced Embrittlement (LMIE) in Al 2024 T0 alloy with melted Gallium and Hydrogen Embrittlement (HE) when High Strength steels like AISI 4140 and UNS 41426 are exposed to Sulfide Hydrogen (H_2S).

Focusing on the development of the tolerance to short crack design methodology to the design of Hydrogen based energy facilities, the original proposed model was extended to account localized plasticity around the notch root and using a new proposed test procedure modified from ASTM E1820 to obtain the fracture toughness in 200bar(g) of pure gaseous Hydrogen.

Traditional recommended methodologies as the T-Wol ASTM E1681 (2023) proposed by ASME to evaluate Hydrogen Embrittlement do not work properly for tough materials and they cannot be used for the qualification of Hydrogen storage tanks materials or pipeline steels.

During a rising load instrumented tests at 200 bar(g) of gaseous hydrogen, the miniature load cell installed inside the autoclave failed. Its failure analysis indicates that the material as it was (17-4PH) is susceptible to Hydrogen Embrittlement with low K_{IEAC} levels. Using the short crack tolerance approach to modify the maximum specified load of the miniature load cell, it was possible to continue with the tests with a new miniature load cell at low load levels.

The observed crack behavior, particularly the arrest of short cracks at stress levels significantly higher than the material's resistance to crack initiation (S_{EAC}) in a hydrogen environment, underscores the potential of the proposed methodologies to enhance safety and reliability in hydrogen facilities. Modifying the ASTM E1820 test method to meet the needs for performing high-pressure hydrogen tests proves to be a promising alternative for determining the resistance to crack propagation in tough materials where the cracks propagate under elastoplastic conditions.

The mechanical design approach considering the occurrence of short cracks in hydrogen environments is significant for industries transitioning to hydrogen-based energy systems, offering a pathway for the safer utilization of existing infrastructure and new designs in line with sustainability goals.

8. Future work

Many challenges related to fracture mechanics are associated with Environmentally Assisted Cracking (EAC). This study sought to investigate the behavior of short cracks in tough materials exposed to hydrogen embrittlement.

In some instances, the materials exhibited brittle behavior, and the linear elastic fracture mechanics were sufficient to provide a good understanding and predict their behavior. However, in engineering application conditions of interest, it is desirable for materials to maintain elastoplastic behavior even in aggressive environments. For these cases, the proposed model including elastoplastic fracture mechanics should be used.

For this purpose, obtaining the elastoplastic properties of tough materials in different corrosive environments and verifying the validity of the model is the main proposal for future work.

Investigating the model's effectiveness on other EAC mechanisms is important since crack behavior tends to remain consistent; hence, it is crucial to ascertain the limits to which the model can be applied.

Conducting the same tests at higher pressures of gaseous H_2 is necessary to confirm the material's behavior under these conditions and to check if reliable results can be obtained at low pressure, providing sufficient information to avoid the need for more complex and dangerous high-pressure tests.

9. References

ALMOND, E. A. et al. **Integrity of gas containers**. Teddington, UK: [s.n.].

ANDERSON, T. L. **Fracture Mechanics - Fundamentals and Applications**. 3rd. ed. [s.l: s.n.].

API. **API Specification 5L, 46th Edition**. [s.l: s.n.].

ASME B31.12. **Hydrogen Piping and Pipelines ASME Code for Pressure Piping.** New York, NYASME, , 2019.

ASME BOILER AND PRESSURE VESSEL CODE. **SECTION VIII Rules for Construction of Pressure Vessels. Division 3 Alternative Rules for Construction of High Pressure Vessels**. [s.l: s.n.]. Disponível em: <www.asme.org/cer>.

ASTM A564/564M. Standard Specification for Hot-Rolled and Cold-Finished Age-Hardening Stainless Steel Bars and Shapes. 2019.

ASTM E8/E8M − 22. Standard Test Methods for Tension Testing of Metallic Materials. **ASTM International**, 2022.

ASTM E140-12BE1. Standard Hardness Conversion Tables For Metals Relationship Among Brinell Hardness, Vickers Hardness, Rockwell Hardness, Superficial Hardness, Knoop Hardness, Scleroscope Hardness, And Leeb Hardness. **ASTM International**, 2012.

ASTM E340. Standard Practice for Macroetching Metals and Alloys. **ASTM International**, 2015.

ASTM E399. Standard Test Method for Linear-Elastic Plane-Strain Fracture Toughness of Metallic Materials. 2022.

ASTM E1681. Standard Test Method for Determining Threshold Stress Intensity Factor for Environment-Assisted Cracking of Metallic Materials. **ASTM**, 2023.

ASTM E1820-23B. **Standard Test Method for Measurement of Fracture Toughness**. [s.l: s.n.]. Disponível em: <www.astm.org.>.

ASTM F1624-12. Standard Test Method for Measurement of Hydrogen Embrittlement Threshold in Steel by the Incremental Step Loading Technique. **ASTM**, 2018.

ASTM G1-03. Standard Practice for Preparing, Cleaning, and Evaluating Corrosion Test Specimens. **ASTM International**, 2017.

ASTM G129 - 21. Standard Practice for Slow Strain Rate Testing to Evaluate the Susceptibility of Metallic Materials to Environmentally Assisted Cracking 1. **ASTM International**, 2021.

BAI, P. et al. Investigations of the diverse corrosion products on steel in a hydrogen sulfide environment. **Corrosion Science**, v. 87, p. 397–406, out. 2014.

BLOOMBERG NEF. **Hydrogen Economy Outlook**. [s.l: s.n.].

BOWKER, P.; HARDIE, D. The Tensile Ductility of a High-Strength Steel in an Atmosphere of Hydrogen. **Metal Science**, v. 9, n. 1, p. 432–436, 1 jan. 1975.

BROWN, B. F. A Preface to the Problem of Stress Corrosion Cracking. Em: **ASTM STP 518 Stress Corrosion Cracking of Metals - A State of the Art**. [s.l: s.n.]. p. 3–15.

CASTRO, J. T. P. DE et al. Prediction of fatigue crack initiation lives at elongated notch roots using short crack concepts. **International Journal of Fatigue**, v. 42, p. 172–182, 1 set. 2012.

CASTRO, J. T. P. DE; MEGGIOLARO, M. A. On the Tolerance to Short Cracks under Fatigue and SCC Conditions. **Procedia Engineering**, v. 74, p. 242–245, 2014.

CASTRO, J. T. P.; MEGGIOLARO, M. A. **Fatigue Design Techniques, Volume 3: Crack Propagation**. 1. ed. Scotts Valley, CA 95066: USA: CreateSpace, 2016a. v. 3

CASTRO, J. T. P.; MEGGIOLARO, M. A. **Fatigue Design Techniques, Volume 1: High-Cycle Fatigue**. 1. ed. Scotts Valley, CA 95066: USA: CreateSpace, 2016b. v. 1

CHEREPANOV, G. P. Crack propagation in continuous media. **Journal of Applied Mathematics and Mechanics**, v. 31, n. 3, p. 503–512, jan. 1967.

CREAGER, M. AND P. C. PARIS. Elastic Field Equations for Blunt Cracks with Reference to Stress Corrosion Cracking. **International Journal of Fracture Mechanics**, v. 3, n. 4, p. 247–252, 1967.

CASTRO, J. T. P. DE et al. Prediction of notch sensitivity effects in fatigue and in environmentally assisted cracking. **Fatigue & Fracture of Engineering Materials & Structures**, v. 38, n. 2, p. 161–179, 7 fev. 2015.

CASTRO, J. T. P. DE; LANDIM, R. V.; MEGGIOLARO, M. A. Defect tolerance under environmentally assisted cracking conditions. **Corrosion Reviews**, v. 33, n. 6, p. 417–431, 1 nov. 2015.

MIRANDA, A. C. DE O. et al. Stress intensity factor predictions: Comparison and round-off error. **Computational Materials Science**, v. 53, n. 1, p. 354–358, fev. 2012.

MIRANDA, A. C. DE O. et al. Use of the stress gradient factor to estimate fatigue stress concentration factors K. **Engineering Fracture Mechanics**, v. 206, p. 250–266, fev. 2019.

DJUKIC, M. B. et al. The synergistic action and interplay of hydrogen embrittlement mechanisms in steels and iron: Localized plasticity and decohesion. **Engineering Fracture Mechanics**, v. 216, p. 106528, jul. 2019.

EL HADDAD, M. H. et al. J integral applications for short fatigue cracks at notches. **International Journal of Fracture**, v. 16, n. 1, p. 15–30, fev. 1980.

EL HADDAD, M. H.; TOPPER, T. H.; SMITH, K. N. Prediction of non propagating cracks. **Engineering Fracture Mechanics**, v. 11, n. 3, p. 573–584, jan. 1979.

EL HADDAD, M.; SMITH, K.; TOPPER, T. A Strain Based Intensity Factor Solution for Short Fatigue Cracks Initiating from Notches. Em: **Fracture Mechanics**. 100 Barr Harbor Drive, PO Box C700, West Conshohocken, PA 19428-2959: ASTM International, 1979. p. 274-274–16.

ESCOBAR, J. D. et al. Compositional analysis on the reverted austenite and tempered martensite in a Ti-stabilized supermartensitic stainless steel: Segregation, partitioning and carbide precipitation. **Materials & Design**, v. 140, p. 95–105, fev. 2018.

EUROPEAN HYDROGEN BACKBONE. **Implementation Roadmap - Cross Border Projects and Costs Update**. [s.l: s.n.].

GERBERICH, W. W. et al. The necessity of both plasticity and brittleness in the fracture thresholds of iron. **Philosophical Magazine A**, v. 63, n. 2, p. 363–376, fev. 1991.

GLICKMAN, E. E. Dissolution Condensation Mechanism of Stress Corrosion Cracking in Liquid Metals: Driving Force and Crack Kinetics. **Metallurgical and Materials Transactions A**, v. 42, n. 2, p. 250–266, 1 fev. 2011.

GRIFFITH, A. A. The Phenomena of Rupture and Flow in Solids. **Philosophical Transactions of the Royal Society of London. Series A, Containing Papers of a Mathematical or Physical Character**, v. 221, p. 163–98, 1921.

HYDEPLOY. **HyDeploy2 Project: Gas Network Innovation Competition // 5th Project Progress Report (PPR)**. [s.l: s.n.].

INA, K.; KOIZUMI, H. Penetration of liquid metals into solid metals and liquid metal embrittlement. **Materials Science and Engineering: A**, v. 387–389, p. 390–394, dez. 2004.

INCE, A.; GLINKA, G. Approximation modeling framework for elastic-plastic stress-strain fields near cracks with a small finite crack tip radius. **Theoretical and Applied Fracture Mechanics**, v. 121, p. 103452, out. 2022.

INGLIS, C. E. Stress in a plate due to the presence of cracks and sharp corners. **Transactions of the Institute of Naval Architects**, v. 55, p. 219–241, 1913.

INTERNATIONAL ENERGY AGENCY. **Net Zero by 2050 - A Roadmap for the Global Energy Sector**. [s.l: s.n.]. Disponível em: <www.iea.org/t&c/>.

ISO 7539-4. Corrosion of metals and alloys Stress corrosion testing Part 4: Preparation and use of uniaxially loaded tension specimens. 1989.

ISO 7539-9. Corrosion of metals and alloys Stress corrosion testing Part 9: Preparation and use of pre-cracked specimens for tests under rising load or rising displacement. 2021.

JIANG, T. et al. Hydrogen embrittlement induced fracture of 17-4 PH stainless steel valve stem. **Engineering Failure Analysis**, v. 113, p. 104576, jul. 2020.

JONES, R. H. (ED.). **Stress-Corrosion Cracking**. 2nd. ed. [s.l.] ASM International, 2017.

KANE, R. D.; CAYARD, M. S. **Roles of H2S in the Behavior of Engineering Alloys: A Review of Literature and Experience**. CORROSION 98. **Anais**...NACE International, 22 mar. 1998.

LANDIM, R. V. et al. Notch sensitivity and short cracks tolerance in a super 13Cr stainless steel under sulfide stress corrosion cracking conditions. **Corrosion Reviews**, v. 41, n. 1, p. 57–71, 23 fev. 2023.

LI, X. et al. **Review of Hydrogen Embrittlement in Metals: Hydrogen Diffusion, Hydrogen Characterization, Hydrogen Embrittlement Mechanism and Prevention**. **Acta Metallurgica Sinica (English Letters)**Chinese Society for Metals, , 1 jun. 2020.

LIAN, Y. et al. Effect of 0.2 and 0.5% Ti on the microstructure and mechanical properties of 13Cr supermartensitic stainless steel. **Journal of Materials Engineering and Performance**, v. 24, n. 11, p. 4253–4259, 22 nov. 2015.

LIU, M. et al. Experimental investigation of failure behavior of the cracked 17-4PH steel blades in a top gas energy recovery turbine. **Engineering Failure Analysis**, v. 105, p. 545–554, nov. 2019.

LIU, M. et al. Plastic stress concentration effects in fatigue strength. **International Journal of Fatigue**, v. 168, p. 107394, mar. 2023.

LYNCH, S. Hydrogen embrittlement phenomena and mechanisms. **Corrosion Reviews**, v. 30, n. 3–4, 1 jan. 2012.

LYNCH, S. P. Hydrogen embrittlement (HE) phenomena and mechanisms. Em: **Stress corrosion cracking: Theory and practice**. [s.l.] Elsevier Ltd, 2011. p. 90–130.

MARCHEBOIS, H.; LEYER, J.; BERTINE ORLANS-JOLIET. **Ssc Performance Of A Super 13% Cr Martensitic Stainless Steel For Octg: Three-Dimensional Fitness-For-Purpose Mapping According To PH2S, Ph And Chloride Content.** CORROSION 2007. **Anais**...NACE International, 11 mar. 2007.

MARTIN, M. L. et al. Enumeration of the hydrogen-enhanced localized plasticity mechanism for hydrogen embrittlement in structural materials. **Acta Materialia**, v. 165, p. 734–750, fev. 2019.

MCLNTYRE, P. Hydrogen Effects in High Strength Steel. Em: ORIANI, R. A.; HIRTH, J. P.; SMIALOWSKI, M. (Eds.). **Hydrogen Degradation of Ferrous Alloys**. Park Ridge, New Jersey, U.S.A: Noyes Publications, 1985. p. 763–798.

MEGGIOLARO, M. A.; MIRANDA, A. C. DE O.; CASTRO, J. T. P. DE. Short crack threshold estimates to predict notch sensitivity factors in fatigue. **International Journal of Fatigue**, v. 29, n. 9–11, p. 2022–2031, 1 set. 2007.

MØLLER, K. T. et al. Hydrogen-A sustainable energy carrier. **Progress in Natural Science: Materials International**, v. 27, p. 34–40, 2017.

NACE MR0175 / ISO 15156. Petroleum And Natural Gas Industries-Materials For Use In H2S-Containing Environments In Oil And Gas Production. **NACE International**, 2020.

NACE TM0177. Laboratory Testing of Metals for Resistance to Sulfide Stress Cracking and Stress Corrosion Cracking in H2S Environments. **NACE International**, 2016.

NACE TM0198. Slow Strain Rate Test Method for Screening Corrosion-Resistant Alloys for Stress Corrosion Cracking in Sour Oilfield Service. **NACE International**, 2020.

NACE TM0316. Four-Point Bend Testing Of Materials For Oil And Gas Applications. **NACE International**, 2016.

NAGUMO, M. Hydrogen related failure of steels – a new aspect. **Materials Science and Technology**, v. 20, n. 8, p. 940–950, 19 ago. 2004.

NARITA, N.; BIRNBAUM, H. K. On the role of phase transitions in the hydrogen embrittlement of stainless steels. **Scripta Metallurgica**, v. 14, n. 12, p. 1355–1358, dez. 1980.

NEUBER, H. Theory of Stress Concentration for Shear-Strained Prismatical Bodies With Arbitrary Nonlinear Stress-Strain Law. **Journal of Applied Mechanics**, v. 28, n. 4, p. 544–550, 1 dez. 1961.

ORIANI, R. A.; JOSEPHIC, P. H. Equilibrium aspects of hydrogen-induced cracking of steels. **Acta Metallurgica**, v. 22, n. 9, p. 1065–1074, set. 1974.

PATONIA, A.; POUDINEH, R. **Hydrogen storage for a net-zero carbon future**. [s.l.] OIES, 2023.

RICE, J. R. A Path Independent Integral and the Approximate Analysis of Strain Concentration by Notches and Cracks. **Journal of Applied Mechanics**, v. 35, n. 2, p. 379–386, 1 jun. 1968.

ROBERTSON, I. M. et al. Hydrogen Embrittlement Understood. **Metallurgical and Materials Transactions B**, v. 46, n. 3, p. 1085–1103, 28 jun. 2015.

SHIGLEY, J.; MISCHKE, C. **Mechanical Engineering Design**. 7th. ed. [s.l.] McGraw-Hill Science/Engineering/Math, 2003.

SHVACHKO, V. Cold cracking of structural steel weldments as reversible hydrogen embrittlement effect. **International Journal of Hydrogen Energy**, v. 25, n. 5, p. 473–480, 1 maio 2000.

SOUSA, R. A. et al. On improved crack tip plastic zone estimates based on T-stress and on complete stress fields. **Fatigue & Fracture of Engineering Materials & Structures**, v. 36, n. 1, p. 25–38, jan. 2013.

STĘPIEŃ, Z. A Comprehensive Overview of Hydrogen-Fueled Internal Combustion Engines: Achievements and Future Challenges. **Energies**, v. 14, n. 20, p. 6504, 11 out. 2021.

TAVARES, S. S. M. et al. Failure analysis of PSV springs of 17-4PH stainless steel. **Engineering Failure Analysis**, v. 16, n. 5, p. 1757–1764, jul. 2009.

TAVARES, S. S. M. et al. Characterization of fracture behavior of a Ti alloyed supermartensitic 12%Cr stainless steel using Charpy instrumented impact tests. **Engineering Failure Analysis**, v. 82, p. 695–702, dez. 2017.

TROIANO, A. R. The Role of Hydrogen and Other Interstitials in the Mechanical Behavior of Metals. **Metallography, Microstructure, and Analysis**, v. 5, n. 6, p. 557–569, 21 dez. 2016.

UDOD, K. A. et al. Factors Determining the Level of Mechanical Properties of Chromium Corrosion-Resistant Steels Alloyed with Nitrogen. **Metallurgist**, v. 60, n. 5–6, p. 503–510, 20 set. 2016.

VASUDEVAN, A. K. **Applied stress affecting the environmentally assisted cracking**. Metallurgical and Materials Transactions A: Physical Metallurgy and Materials Science. **Anais**...mar. 2013.

WASIM, M.; DJUKIC, M. B.; NGO, T. D. Influence of hydrogen-enhanced plasticity and decohesion mechanisms of hydrogen embrittlement on the fracture resistance of steel. **Engineering Failure Analysis**, v. 123, 1 maio 2021.

WU, H. et al. On the prediction of the residual fatigue life of cracked structures repaired by the stop-hole method. **International Journal of Fatigue**, v. 32, n. 4, p. 670–677, 1 abr. 2010.

YOUSEFI, M. et al. Failure Analysis of a 17-4PH Stainless Steel Part in an Exhaust Fastener. **Journal of Failure Analysis and Prevention**, v. 21, n. 6, p. 2278–2289, 17 dez. 2021.

YURIOKA, N.; SUZUKI, H. Hydrogen assisted cracking in C-Mn and low alloy steel weldments. **International Materials Reviews**, v. 35, n. 1, p. 217–249, 20 jan. 1990.

ZHAO, Y. et al. The role of hydrogen in hardening/softening steel: Influence of the charging process. **Scripta Materialia**, v. 107, p. 46–49, out. 2015.